

2018

Fabrication and Characterizations of LAGP/PEO Composite Electrolytes for All Solid-State Lithium-Ion Batteries

Jeremy J. Lee
Wright State University

Follow this and additional works at: https://corescholar.libraries.wright.edu/etd_all



Part of the [Mechanical Engineering Commons](#)

Repository Citation

Lee, Jeremy J., "Fabrication and Characterizations of LAGP/PEO Composite Electrolytes for All Solid-State Lithium-Ion Batteries" (2018). *Browse all Theses and Dissertations*. 1959.
https://corescholar.libraries.wright.edu/etd_all/1959

This Thesis is brought to you for free and open access by the Theses and Dissertations at CORE Scholar. It has been accepted for inclusion in Browse all Theses and Dissertations by an authorized administrator of CORE Scholar. For more information, please contact library-corescholar@wright.edu.

Fabrication and Characterizations of LAGP/PEO Composite
Electrolytes for All Solid-State Lithium-Ion Batteries

A thesis submitted in partial fulfillment
of the requirements for the degree of
Master of Science in Renewable
and Clean Energy Engineering

By

JEREMY J. LEE

B.S. in Mechanical Engineering, Wright State University, 2015

2018

Wright State University

WRIGHT STATE UNIVERSITY

GRADUATE SCHOOL

April 12, 2018

I HEREBY RECOMMEND THAT THE THESIS PREPARED UNDER MY SUPERVISION Jeremy J. Lee
ENTITLED Fabrication and Characterizations of LAGP/PEO Composite Electrolytes for All Solid-
State Lithium-Ion Batteries BE ACCEPTED IN PARTIAL FULLFILLMENT OF THE REQUIREMENT
FOR DEGREE OF Master of Science of Renewable and Clean Energy Engineering.

Hong Huang, Ph.D.
Thesis Director

Joseph C. Slater, Ph.D., P.E.
Chair, Department of Mechanical and
Materials Engineering

Committee on final examination:

Hong Huang, Ph.D.

James Menart, Ph.D.

Thomas Howell, Ph.D.

Michael Rottmayer , Ph.D.

Barry Milligan, Ph.D.
Interim Dean of the Graduate School

Abstract

Lee, Jeremy J. M.S.R.C.E. , Department of Mechanical and Materials Engineering, Wright State University, 2018. "Fabrication and Characterizations of LAGP/PEO Composite Electrolytes for All Solid-State Lithium-Ion Batteries"

With the rise of electric vehicles and increasing dependence on mobile electronics, the demands for lithium-ion batteries have followed in tandem for their high energy and power densities. However, traditional lithium-ion batteries consisting of liquid electrolytes have limited operating temperatures and are susceptible to ignition and subsequent fires. Recently, battery research has diverged into solid state chemistry to address the aforementioned issues. In this research, we systematically investigate a series of ceramic/polymer lithium-ion conducting composite electrolytes, i.e. $\text{Li}_{1.4}\text{Al}_{0.4}\text{Ge}_{1.6}(\text{PO}_4)_3$ /lithiated polyethylene oxide (LAGP/PEO). Lithiated PEO was prepared with two different lithium salts, LiBF_4 and LiTFSI. The impacts of the LAGP on the electrical, thermal, and mechanical properties of the two lithiated PEO systems are assessed. When LAGP is homogeneously distributed in PEO-LiTFSI films, ionic conductivities and thermal properties remain relatively uninhibited; the elastic modulus and ultimate strength increased up to 450% and 200%, respectively. When LAGP was added to PEO- LiBF_4 films, it increased the elastic strength nearly 200% without compromising the ultimate strength and thermal properties, but at the sacrifice of ionic

conductivity. The ceramic/polymeric electrolytes have potential applications to flexible all solid state lithium-ion batteries.

Table of Contents

1	Introduction	1
1.1	Operating Principle of Lithium Ion Battery	2
1.2	Cathode Materials	4
1.3	Anode Materials	7
1.4	Limitations of Electrode Materials.....	9
1.5	Electrolytes in Lithium Ion Batteries.....	9
1.5.1	Liquid Electrolytes	10
1.5.2	Challenges That Liquid Electrolyte Faces in Li-ion Batteries	13
1.5.3	Polymer Electrolytes	14
1.5.4	Ceramic Electrolytes.....	18
1.5.5	Ceramic Composite Electrolytes	20
1.6	Summary	23
1.7	Outline of this Thesis Research	23
2	Synthesis and Characterization of LAGP Powders	25
2.1	Synthesis Process.....	25
2.2	Structural Characteristics of LAGP	26

2.3	Ionic Conduction Characteristics of the LAGP	28
2.4	Summary	35
3	Fabrication and Characterizations of LAGP/PEO/Li-salt Composite Electrolyte Membranes.....	36
3.1	LAGP/PEO/LiBF ₄ Composite Film Compositions	36
3.2	LAGP/PEO/LiTFSI Composite Film Compositions	37
3.3	Fabrication of LAGP/PEO/Li-salt Composite Electrolyte Membranes.....	38
3.4	Structural Characterization of the Composite Films	40
3.5	Thermal Characterizations of the Composite Films	42
3.6	Surface Morphological Imaging of the Composite Films	48
3.7	Summary	50
4	Ionic Conduction of the Composite Films.....	51
4.1	EIS Results Using Stainless Steel Electrodes	51
4.2	EIS Results Using Lithium Electrodes	55
4.3	Ionic Conductivity Characteristics of the Composite Films.....	62
4.3.1	Lithiated Polymer Ionic Conductivity	62
4.3.2	With Addition of LAGP	66

4.4	Summary	70
5	Mechanical Characterization of the Composite Films.....	72
5.1	Experimental Aspects for Mechanical Testing	73
5.2	Stress-Strain Behavior of Pure PEO films.....	76
5.3	Mechanical Characteristics of LAGP/PEO/LiBF ₄ Composite Films	77
5.4	Mechanical Characteristics of LAGP/PEO/LiTFSI Composite Films.....	82
5.5	Morphological Evolution of the Composite Films Upon Stretching	83
5.6	Accuracy of Equipment Used in Mechanical Testing	88
5.7	Processing Factors Affecting the Mechanical Properties.....	90
5.7.1	Surface Morphology.....	90
5.7.2	Differences Between Front and Back of Films	91
5.7.3	Uncommon large ceramic particles	94
5.7.4	Internal Ceramic Particle Size and Distribution	94
5.8	General Discussion	99
5.9	Summary	99
6	Conclusion.....	101

List of Figures

<i>Figure 1: A schematic of a lithium-ion battery made up of carbon anode and LiCoO₂ cathode [4]</i>	3
<i>Figure 2: Illustration of crystal structure (a) Layer-structured LiCoO₂, (b) Spinel-structured LiMn₂O₄, (c) Olivine-structured LiFePO₄, (d) Tavorite Structure LiFeSO₄F [1]. ..</i>	7
<i>Figure 3: XRD spectra of LAGP synthesized in different laboratories (a) Li_{1.4}Al_{0.4}Ge_{1.6}(PO₄)₃ synthesized in our lab; (b) sintered at 1450°C and annealed at 650°C Li_{1.4}Al_{0.4}Ge_{1.6}(PO₄)₃ [90]; (c) Li_{1.5}Al_{0.5}Ge_{1.6}(PO₄)₃ calcined at 700°C and sintered at 900°C [92].....</i>	27
<i>Figure 4: Cross-Sectional SEM Images of LAGP Pellets Calcined (a) at different temperatures for 6 hours; (b) at 850° Celsius for different times [93]</i>	29
<i>Figure 5: A silver coated pellet with two copper electrodes for electrochemical impedance measurement.</i>	30
<i>Figure 6: Electrochemical impedance spectra (Nyquist plots) of (a) sintered LAGP pellet at 105° C. The inset shows the Randles equivalent circuit used to derive the resistance of LAGP electrolyte for conductivity calculation.</i>	32
<i>Figure 7: Arrhenius plot, logarithm conductivity vs. reciprocal of temperature, of sintered LAGP pellet</i>	33
<i>Figure 8: Impedance spectra of (a) LATGP, (b) LAGP, and (c) LATTP obtained using two lithium electrodes at 20° Celsius[101]</i>	35

<i>Figure 9: Kapton Bruker Film Holder used for XRD measurement of the composite membrane</i>	41
Figure 10: XRD patterns of the LAGP/PEO/LiTFSI series in comparison with LAGP powders and PEO.....	42
Figure 11: DSC profiles obtained from (a) LAGP/PEO/LiBF ₄ ; (b) LAGP/PEO LiTFSI Composite Films.....	43
Figure 12: Selection of the onsite melting temperature for analysis (a) in LAGP/PEO/LiBF ₄ composite system; (b) in LAGP/PEO/LiTFSI composite system.....	45
Figure 13: Melting temperature and onsite melting temperature as a function of LAGP content in (a) LAGP/PEO/LiBF ₄ series; (b) in LAGP/PEO/LiTFSI series.	47
Figure 14: Top-view SEM images showing the surface morphologies and LAGP distribution in the LiBF ₄ film series (a) PEO; (b) LAGP20; (c) LAGP30; (d) LAGP40; (e) LAGP50; (f) LAGP60.....	49
Figure 15: Nyquist impedance plot of LAGP20/LiBF ₄ Composite obtained at (a) 25° Celsius (b) 80° Celsius using two stainless steel electrodes.....	53
Figure 16: Nyquist Plot of LAGP30/LiBF ₄ Composite Electrolytes of two different thickness, 127 microns and 415 microns, using stainless steel electrodes.....	54
Figure 17: Arrhenius conductivity plot of LAGP/PEO/LiBF ₄ samples obtained using stainless steel.....	55
Figure 18: A Schematic of Coin Cell Assembly For Electrochemical Characterization	56

Figure 19: EIS of the LAGP20/LiBF ₄ film obtained at 35°C using an AC voltage of 100 mV and DC voltages ranging from 0 to 750 mV.....	57
Figure 20: EIS of the LAGP20/LiBF ₄ film obtained from 55° to 80° Celsius with no DC polarization	58
Figure 21: EIS spectra of LAGP20/LiBF ₄ film at 80°C at the 2 nd , 3 rd , and 4 th thermal cycles.	59
Figure 22: EIS spectra of LAGP20/LiBF ₄ film at 80 °C as a function of time	60
Figure 23: EIS spectra of LAGP20/LiBF ₄ film at 45 °C at the 2 nd , 3 rd , and 4 th thermal cycles.	61
Figure 24: Arrhenius Conductivity Plots of (a) PEO/LiBF ₄ (8:1) film; (b) PEO/LiTFSI (20:1) film; (c) PEO/LiBF ₄ (4.5:1) [109]; and (d) PEO/LiTFSI (20:1) film [108]	62
Figure 25: Arrhenius Conductivity Plot Summary of (a) LAGP/LiBF ₄ ; (b) LAGP/LiTFSI PEO-based Composite Films	67
<i>Figure 26: An Engineering Drawing and Specs of ASTM Standard Used</i>	<i>74</i>
Figure 27: LAGP50/LiTFSI Composite Tensile Sample Punched From a D638V Die	74
Figure 28: Mitutoyo 293-185 micrometer	75
Figure 29: (a) the extensometer used to stretching LAGP/PEO/Li-salt Composite Film; (b) The LabVIEW GUI Used to Control The Tensiometer and Record Data	75
Figure 30: Stress vs Strain Plot of 400,000 Molecular Weight PEO	76

Figure 31: The stress-strain plots obtained from PEO/LiBF₄ series with LAGP weight percent from 0% to 60%. (a) LAGP0, (b) LAGP20, (c) LAGP30, (d) LAGP40, (e) LAGP50, and (f) LAGP60. 78

Figure 32: Mechanical properties of the composite films as a function of LAGP weight percent in the LiBF₄ series. (a) average Elastic modulus; (b) average ultimate strength; (c) statistic failure strain (the straight line is the instrumental limit)..... 81

Figure 33: The stress-strain plots obtained from PEO/LiTFSI series with LAGP weight percent from 0% to 60%. (a) LAGP0, (b) LAGP20, (c) LAGP50, and (d) LAGP60. 83

Figure 34: SEM images of PEO (left) and LAGP30/PEO/LiBF₄. (a) PEO unstretched; (b) LAGP30 unstretched; (c) PEO stretched, top view; (d) LAGP30 stretched, top view; (e) PEO stretched, side view after FIB cutting; (f) LAGO 30 stretched, top view with micropore..... 84

Figure 35: Top-view SEM images of stretched LAGP0/PEO/LiBF₄. (a) silver streak at the necking area; (b) micropore at the necking area; (c) increased micropore in the center area. 85

Figure 36: Cross-section SEM images of LiBF₄ series before (left) and after (right) tensile test (a, b) LAGP20; (c, d) LAGP 30; (e, f) LAGP 60 tensile test 87

Figure 37: SEM image of the back side of a LAGP20/PEOLiBF₄ Film 90

Figure 38: To-view SEM images of there exist spherulite structure in some specimens (a) LiBF₄/PEO film; (b) LAGP40/PEO/LiBF₄ film; (c) LAGP60/PEO/LiBF₄ Film..... 92

Figure 39: Top-view SEM images showing the morphological difference between the top side (left) and bottom side (right) of the LiBF₄ series composite films ; (a, b) PEO; (c,d) LAGP20; (e,f) LAGP40..... 93

Figure 40: A side-view SEM image showing an uncommon LAGP agglomerate in an area in the LAGP60/PEO/LiBF₄ Film 94

Figure 41: Stress-strain plots of LAGP50/PEO/LiTFSI films obtained from three different batch (followed same fabrication processing) 96

Figure 42: Side—view SEM images of LAGP50/PEO/LiTFSI films before (left) and after (right) tensile stretching cut with the help of FIB. (a, b) batch1; (c, d) batch 3 97

List of Tables

Table 1: Ionic conductivities of 1 Molar Solution Salt in PC:DME	13
Table 2: Ionic conductivities of inert fillers in composite electrolytes	21
Table 3: Ionic conductivities of active fillers in composite electrolytes	22
Table 4: Ionic conductivities and activation energy values of LAGP reported in literatures.....	34
Table 5: The amount of each component used to fabricate the LAGP/PEO/LiBF ₄ series	37
Table 6: The amount of each component used to fabricate the LAGP/PEO/LiTFSI series	38

Acknowledgements

I would like to thank all the people who helped me throughout my time spent towards completing my thesis at Wright State University. I'd like to thank my advisor, Dr. Hong Huang for her subject matter expertise, her help doing the FIB/SEM work, and lastly, for helping me throughout the manuscript writing. I would like to thank Dr. Michael Rottmayer for the opportunity to work on this project and providing guidance in this project. I would like to thank Dr. Thomas Howell for the hours he spent coaching me through the thesis project and providing mentorship. I would like to also thank all the other staff at Wright Patterson Air Force Base who spent the resources and time to aid me in my research: Dr. Padmakar Kichambare and Mr. Tom Jenkins for their lab assistance, and Dr. Bang Tsao for assisting me in equipment acquisitions. Lastly, I would like to thank my parents for their love and patience throughout this endeavor and their continued support for which I would have never been able to succeed.

1 Introduction

As fossil fuels begin to deplete and the cost of extraction becomes less economically feasible, it is of increasing interest to migrate towards renewable energy sources. Renewable energy sources like wind, solar, and hydrogen are promising technologies to replace hydrocarbon fuels because their perpetual life cycles and their operating costs are independent of global market forces. However, a current limitation for widespread use of renewable energies is the ability to store it efficiently. Common commercial methods to store energy are electrochemical devices like batteries.

There are two classes of batteries, primary and secondary. Primary batteries are often used in one-off applications such as medical devices. Secondary batteries are a class of batteries we often refer to as rechargeable batteries. The most commonly utilized secondary battery are lithium-ion batteries.

What makes lithium ion attractive as a charge carrier and hence lithium-ion batteries is due to a number of reasons, giving it wide market potential ranging from consumer electronics to electric vehicles [1]. Lithium possesses a high theoretical energy density, large reduction potential, and is one of the lightest elements. In addition to the exceptional material properties of lithium, it is believed that there are largely untapped reservoirs of lithium sitting in the earth's crust. In fact, if world economies had

an optimistic annual GDP growth rate of 3%, it is believed that total accumulated demand for lithium in 2100 will top out at around 20-30 megatons[2]. When exploiting lithium resources it is generally agreed upon that we would be within our carrying capacity with proper recycling and mining. The projected world supply of lithium is as much as 40 megatons, sufficient to put an estimated 12 billion electric vehicles on the road [3].

1.1 Operating Principle of Lithium Ion Battery

A traditional lithium ion battery is composed of four components: a cathode, anode, separator, and an electrolyte. The cathode material is typically a lithium transition metal oxide and the anode is a carbon-based material. The electrolyte is a lithium-ion conductor but electron insulator, which can be liquid, polymer or solid. Under some laboratory circumstance, a liquid electrolyte alone would be enough to prevent electrical shorting. In practical battery setting made up of liquid electrolyte, it is often necessary to utilize a separator. A separator functions as a permeable membrane of electrolyte, but as a physical barrier between the electrodes.

In principle, the cathode and anode in lithium-ion batteries undergo redox reactions when a load is applied (discharging) or electricity is supplied externally to the battery (charging). A schematic can be seen in **Figure 1**. When a battery is being charged, the cathode is oxidized, i.e. valence electrons from the transition metal leave to the external circuit while lithium ions pass through the electrolyte into the anode. Specifically, as charge carriers exit the system, the lithium ions de-intercalate from the

cathode structure, diffuse inside the electrolyte, recombine with the free electrons at the anode interface, and intercalate into the anode structure. During discharge, the system operates in reverse, where when a load is applied, electrons leave the anode, lithium de-intercalates accordingly, and both components recombine inside the cathode.

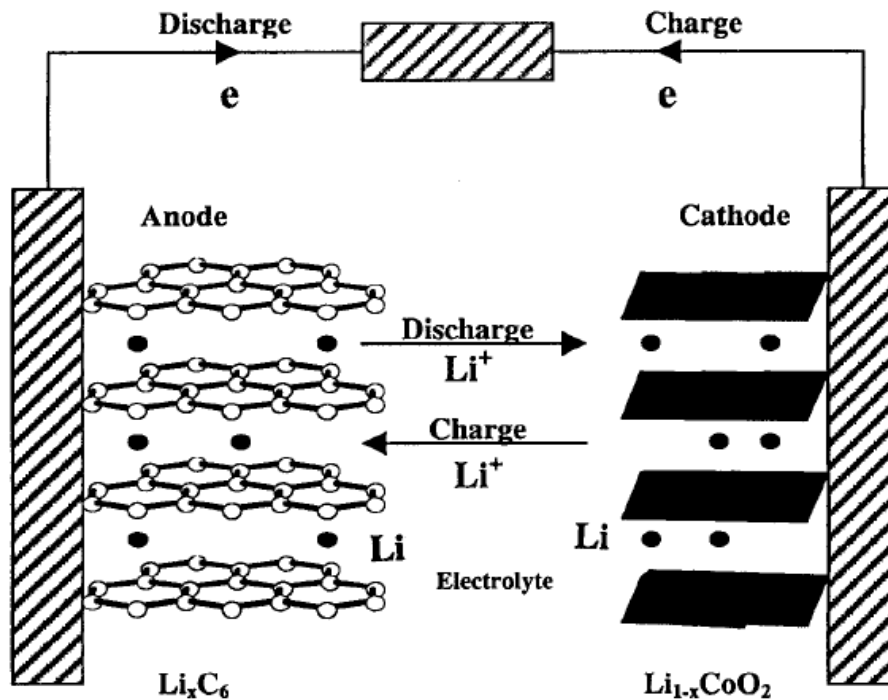
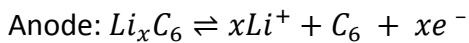
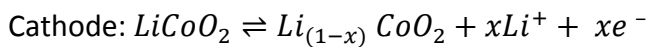
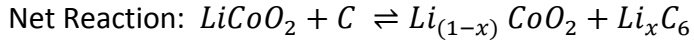


Figure 1: A schematic of a lithium-ion battery made up of carbon anode and LiCoO_2 cathode [4]

The reactions of the exemplar lithium-ion cell presented in **Figure 1** redox reactions proceed in the following manner :





1.2 Cathode Materials

There are a variety of requirements for cathodes in lithium-ion batteries. The structure should offer a high specific capacity, high volumetric capacity, good capacity retention or coulombic efficiency, a high potential, and small volumetric changes upon lithium insertion/removal. Typically, cathodes are lithium transition metal oxides with a general chemical formula of $Li_xM_yX_z$ where the M is a transition metal species and X is an anionic species.

The theoretical specific energy capacity of an electrode can be calculated using a modified form of Faraday's Law presented in the following equation[5, p. 429]:

$$Q_{theoretical} = \frac{nF}{3.6 * M_{weight}} \left[\frac{mAh}{gram} \right]$$

The variables Q, n, F, and M_{weight} correspond to the theoretical specific energy capacity, the number of electrons carried per ion, Faraday's constant in Joules, and the molecular weight of electrode material, respectively.

There have been many advances in lithium-ion battery cathode chemistry. The most notable contributions have been made by John Goodenough who developed the first commercially viable chemistry, lithium cobalt oxide ($LiCoO_2$) in the 1980s[6]. While $LiCoO_2$ has a high operating voltage and large theoretical specific energy capacity of 274 mAh/g assuming all lithium could be extracted from the structure. Practically, only half of lithium can be extracted. With its large and non-linear volumetric expansion, if more

than half of the lithium was extracted, LiCoO_2 irreversibly changes from a hexagonal structure to a monoclinic structure, which can affect its cycling performance[7]. In addition to mechanical breakdown of the cathode, LiCoO_2 begins to release oxygen exothermically when operating above 250° Celsius, which can result in thermal runaway, cell expansion, and eventual fires. Also problematic, while LiCoO_2 has a starting discharge potential of 4 Volts, it's discharge plateau changes drastically with its state of charge (SOC), which means it requires additional circuitry like a buck-converter to deliver constant power. Technical issues aside, the cost of cobalt processing and limited supply could make it economically infeasible to manufacture LiCoO_2 in the future[8].

As a result of the performance, safety issues, and the supply bottleneck of LiCoO_2 , other cathode materials have been subsequently conceived, such as LiNiO_2 , LiMn_2O_4 , and LiFePO_4 to name a few. The aforementioned chemistries all have different dopants and crystal structures which can affect their discharge characteristics[1]. A few example cathode unit cells can be seen in **Figure 2**.

The layer-structured LiNiO_2 has a high energy density, large theoretical specific energy capacity, is cheaper than LiCoO_2 . But LiNiO_2 is more thermally unstable than LiCoO_2 [9]. In addition, LiNiO_2 cathodes have an issue with Ni^{2+} substituting with lithium sites during the de-intercalation process, effectively blocking lithium diffusion and inhibit performance [10].

Non-layered cathode structures such as olivine, spinel, and tavorite have very stable 3D lattice structures and as a result, have very low volumetric expansion during the intercalation/de-intercalation process. As a result of their small volume changes, cathodes such as LiFePO_4 and LiMn_2O_4 with their olivine and spinel structures, have flat discharge plateaus [11], [12]. LiFePO_4 is very environmentally friendly, has high cycle life, and has very little exothermic release during decomposition. LiMn_2O_4 has a high operating voltage, very little exothermic release during decomposition, and is less expensive to manufacture than LiCoO_2 . While many advanced cathode materials have been proposed, there are many caveats with each cathode material. For instance, LiFePO_4 has a relatively low energy density [13], [14], while LiMn_2O_4 can undergo several phase changes during cycling, it has low temperature stability, and has a low energy density like LiFePO_4 [13], [15]. As with any material, the cathode used will depend on the applications' requirements.

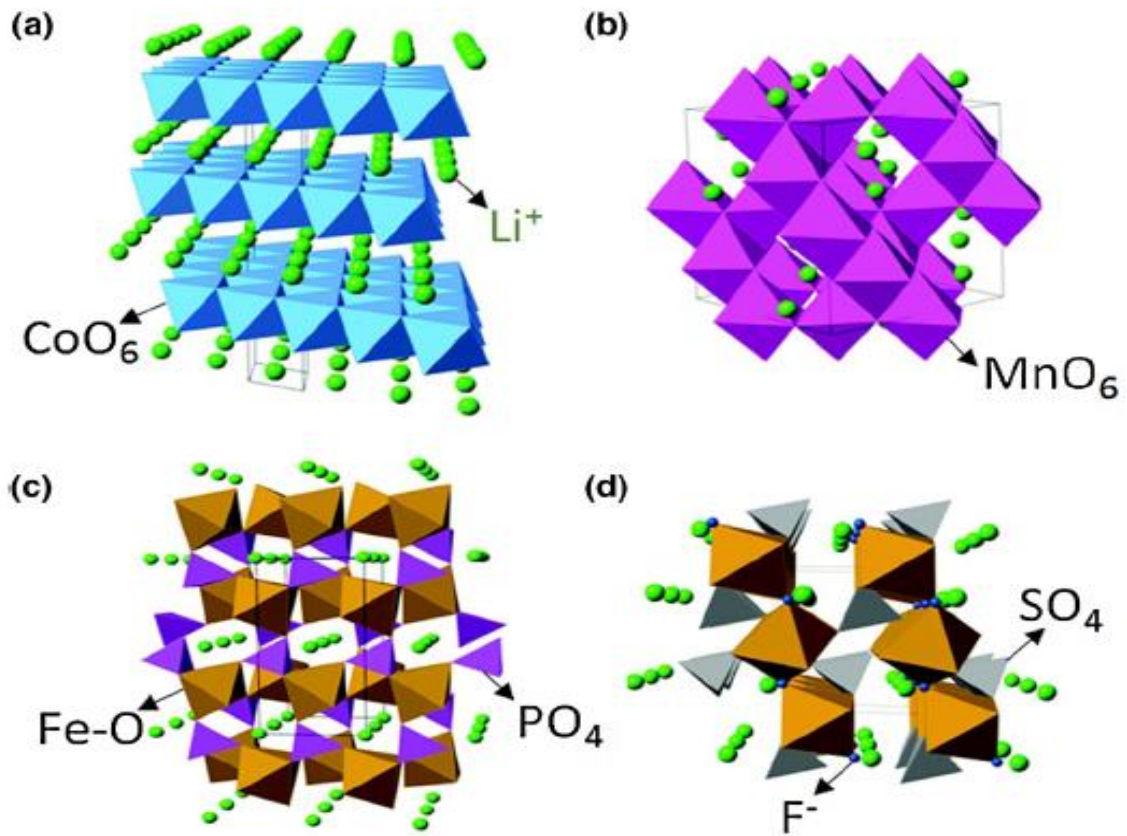


Figure 2: Illustration of crystal structure (a) Layer-structured LiCoO_2 , (b) Spinel-structured LiMn_2O_4 , (c) Olivine-structured LiFePO_4 , (d) Tavorite Structure LiFeSO_4F [1].

1.3 Anode Materials

The most typical intercalation anode utilized in industry and research is graphite based materials. Graphitic carbon has high electrical conductivity, is abundant, has low volumetric expansion during intercalation/de-intercalation, and has a low redox potential[16]–[18]. Additionally, graphite has a high theoretical energy density of 372 mAh/g, which exceeds most typical cathodes' gravimetric energy density.

Since the utilization of carbon, other anode materials have been studied such as $\text{Li}_4\text{Ti}_5\text{O}_{12}$, silicon, germanium, and tin. $\text{Li}_4\text{Ti}_5\text{O}_{12}$ is often referred to as a zero strain electrode because of its low volumetric change of 0.02% during lithium insertion and removal. This allows the material to be charged several thousand times without any mechanical degradation[19]–[22]. In addition to excellent cycle life, $\text{Li}_4\text{Ti}_5\text{O}_{12}$ has a potential above 1 Volt which enables it to avoid the drastic capacity fade most lithium-ion batteries experience from solid electrolyte interphase(SEI) formation[23, pp. 93–166]. The disadvantages of using $\text{Li}_4\text{Ti}_5\text{O}_{12}$ as an anode, is that it has a low energy density and because it possesses a large potential, it reduces the max operating voltage of a lithium-ion battery.

Elements like silicon, germanium, and tin are often referred to as alloying electrodes because they tend to form compound phases with lithium rather than rely on Van Der Waals to store the material. The main benefit of using these different alloying materials as an anode is that they have much higher theoretical energy capacities than carbon[24]–[28]. Silicon, for example, has a theoretical gravimetric energy density of 4200 mAh/g, even greater than lithium whose theoretical energy density of 3800 mAh/g. Unfortunately, alloying materials have volumetric expansions of several hundred percent when complexed with lithium. Such anodes can start to pulverize and fracture during cycling.

1.4 Limitations of Electrode Materials

With the exception of graphite based electrodes, most if not all electrode materials are not electronically conductive. Because of the low electronic conductivity of electrode materials, they must be blended with conductive media such as acetylene black or carbon nanotubes to facilitate electron exchange of the electrode materials[29]. By adding carbon to the lithium battery, it is effectively reducing the overall gravimetric energy density of the entire battery package because carbon additive does not contribute to the energy capacity but increases the weight of battery. Lastly, the electrode materials for most commercial batteries have gravimetric energy densities less than 300 mAh/g. Energy density of electrodes needs to be increased to seamlessly replace hydrocarbon fuels and commercialize electric vehicles successfully.

1.5 Electrolytes in Lithium Ion Batteries

In addition to high lithium ion conductivity, a critical requirement of the electrolyte is that it should have a high break down voltage or di-electric constant to accommodate the operating voltage of the electrode materials. To ensure there is no oxidation or reduction of the electrolyte, the redox energies of both the anode and cathode should not exceed the bandgap of electrolyte. By acknowledging the aforementioned limitation, the open circuit voltage of a secondary lithium battery is limited by the following relationship[4, p. 5]:

$$eV_{oc} = \mu_{cathode} - \mu_{anode} < E_g$$

1.5.1 Liquid Electrolytes

Liquid electrolytes typically are composed of non-aqueous, aprotic, organic solvents, and lithium salts. The most commonly used aprotic solvents are dioxolane, ethylmethyl carbonate (EMC), ethylene carbonate (EC), diethyl carbonate (DEC), and propylene carbonate (PC). These solvents have a wide electrochemical window (0 to 6 volts) against lithium[30, pp. 93–102], [31]. To completely dissociate lithium ions, the chosen solvent is preferable to have a dielectric constant >37 [32]. When lithium salts are not completely dissociated, it results in a lower number of charge carriers which can lead to an overall decrease in the ionic conductivity of the liquid electrolyte. Other solvents such as γ -butyrolactone have been proposed that meet the dielectric constant requirement, but have limited performance and stability[33]. While propylene carbonate is sometimes used as a solvent in liquid electrolytes, it is not a suitable choice for conventional lithium-ion battery packs. During the intercalation/de-intercalation process, propylene carbonate transports with lithium in-between the graphite layers, inadvertently exfoliating layers of carbon from the graphite, and subsequently results in large capacity loss[34], [35]. It is determined that ethylene carbonate is a preferable solvent in terms of electrochemical stability for lithium-ion battery packs that use carbon based anodes, as it is the only solvent that can facilitate reversible intercalation due to its formation of a passivating layer. Despite ethylene carbonate's ability to solvate lithium ions and its reversibility, it is not practical to use the solvent by itself because its melting point is approximately 40° Celsius. At present, most liquid electrolytes are a blend of several solvents. Albeit the high melting point of ethylene

carbonate, it's still used as the primary solvent or majority charge carrier in solvent blends. Because of their low temperature melting points and miscibility with ethylene carbonate, dimethyl-carbonate(DMC), diethyl-carbonate(DEC), and dioxolane are used for blending, but in a limited quantities. The low boiling points and flash temperatures of the organic solvents effectively limit the operating temperature of the batteries.

Various lithium salts, to be dissolved in the aprotic above solvents as the electrolyte, include LiPF_6 , LiClO_4 , LiAsF_6 , LiSO_3CF_3 (LiTF), LiBF_4 , and $\text{LiN}(\text{SO}_2\text{CF}_3)_2$ (*LiTFSI*). Lithium salts are typically kept in inert or non-aqueous environments because they are susceptible to hydrolysis in the presence of water. When the anions undergo hydrolysis, the reaction can proceed with the formation of HF gas and can inhibit the batteries' performance[36]–[38].

The mixture of solvents and salts typically yield ionic conductivities greater than 10^{-3} S/cm. LiPF_6 , being one of the most conductive salts, having the ability to form a stable passivation layer with aluminum current collectors and graphite has made it a favorite for commercial battery packs[30, p. 8]. For most of the literature presented, LiPF_6 is often used as the reference to determine if the novel or studied liquid electrolytes have desirable properties. LiClO_4 yields electrolyte solutions with high ionic conductivities, but its suitability for commercial applications is thrown into question when acknowledging its potential hazards. LiClO_4 /dioxolane batteries can explode or catch on fire if overcharged, and there's a high probability of explosion/puncture if the battery packs are impacted with a large force[39]. LiClO_4 electrolytes can also explode at temperatures above 220° Celsius, a condition that can be easily achieved in

circumstances of thermal runaway or continuous exothermic decomposition[40]. In addition to its limited safety, while LiClO_4 electrolyte solutions are stable against aluminum current collectors up to 4.5 volts, it readily oxidizes with stainless steel at around 3V and without passivation, which disqualifies it for use in coin cell batteries[41]. LiAsF_6 is a lithium salt that has a higher moisture and thermal stability than LiPF_6 and has one of the highest cycling efficiencies, but it is an incredibly toxic salt due to its ability to form arsenic byproducts[42]. LiSO_3CF_3 has a strong resistance to hydrolysis due to its C-F bond, but it has one of the lowest ionic conductivities of the aforementioned salts, and oxidizes with aluminum current collectors near 3 volts [30, p. 8], [43], [44]. LiBF_4 is a salt that has a lower ionic conductivity than LiPF_6 , but as documented by thermogravimetric analysis results(TGA), it is much more resistant to hydrolysis and thermal decomposition[45]–[47]. An additional benefit of using LiBF_4 is that it can create a passivation layer on aluminum foil which is stable at high voltages, whereas LiPF_6 's passivation layer can break down at 5.6 volts[48]. As a result of its thermal and electrochemical properties, LiBF_4 operates more efficiently than LiPF_6 at high temperatures[49]. LiTFSI has a lower ionic conductivity than LiPF_6 , but it is much higher than LiBF_4 and LiSO_3CF_3 [47]. In addition, LiTFSI has a remarkably high tolerance to hydrolysis because of the strong C-F bond; in open air it can be left out for days without degrading and its stable until at least 300° Celsius [46], [50]. However despite its high stability with air, when mixed in low concentrations with aprotic solvents, it has been observed to corrode aluminum foil at voltages as low as 3-3.5V, but the aforementioned corrosion observed with LiTFSI chemistries is not well understood [51], [52]. Despite

there being large amounts of literature that suggest LiTFSI is unstable against aluminum, there have been studies that propose stability can be achieved with a high molar concentrations of LiTFSI [53].

A table summarizing all the ionic conductivities of the previously mentioned salts as a 1 molar solution in PC:DME are in **Table 1**[47]:

Table 1: Ionic conductivities of 1 Molar Solution Salt in PC:DME

Salt	Ionic Conductivity (10^{-3} S/cm)
LiTF	6.12
LiBF ₄	9.46
LiTFSI	12.6
LiClO ₄	13.5
LiAsF ₆	14.8
LiPF ₆	15.3

Other liquid electrolytes have been proposed such as ionic liquids, which are salts that have melting points well below STP conditions, but this subject matter is beyond the scope of this work.

1.5.2 Challenges That Liquid Electrolyte Faces in Li-ion Batteries

While lithium-ion batteries have higher energy density than most conventional energy storage devices, they still have many hurdles to overcome. Lithium batteries use volatile hydrocarbon solvents, which pose a real-world risk to consumers. An example of the risks that lithium-ion batteries can pose is when on January 16, 2013 all Boeing 787 Dreamliner airplanes were grounded when two of them caught on fire due to lithium-ion battery pack failures [54].

The cycling life of commercially available lithium-ion batteries is another big issue. Most lithium ion batteries can only be cycled a few hundred times. The reason for the drastic capacity fade of these lithium ion batteries is due to the passivation layer or solid electrolyte interface (SEI) that forms on the electrodes. While SEI is instrumental in maintaining the shelf life of lithium-ion batteries, its continuous formation can be the cause of battery failure. Metal halides can form from the redox reactions and cause a drop in the Coulombic efficiency. Alkali halides consume lithium ions which results in a decrease in the number of charge carriers available to intercalate the electrodes. Most worry-some about these alkali halides is that they have typically have a breakdown voltage higher than the electrolyte, therefore, the formation of these halides increase the internal resistance of the battery and create irreversible capacity loss [55].

The utilization of aprotic-containing electrolyte is a potential safety hazard. The formation of these continuous passivation layers is another problem with liquid electrolytes. The research and development of electrolyte materials alternative to the traditional liquid electrolyte will be essential for the future of lithium-ion batteries.

1.5.3 Polymer Electrolytes

There are three polymer systems typically encountered in electrochemistry: gel, dry-polymer, and polymer-in-salt systems. Lithium salts that are typically blended with polymer electrolytes are LiTFSI, LiTF, LiClO₄, and LiPF₆. Gel polymer electrolytes are usually polymer electrolytes that have been enhanced with a solvent (like PEG, carbonate solvents, ionic liquids) or solid plasticizers like succinonitrile. Dry-polymer

electrolytes are typically polymer systems that have lithium salts dissolved in concentrations lower than 50 weight percent. Polymer-in-salt systems are polymer electrolytes with a composition of lithium salt in excess of 50 weight percent.

Gel polymer electrolytes typically use poly-methyl-methacrylate (PMMA), polyvinyl-chloride (PVC), polyacrylonitrile (PAN), polyvinylidene-fluoride (PVDF), or polyvinylidene-fluoride-hexafluoropropylene (PVDF-HFP) as the host polymer. While a gel electrolyte utilizes a polymer host, its ion conduction is dominated by the swollen gelled phase or liquid phase of the electrolyte[56]. Despite gel electrolytes mirroring liquid electrolytes' conduction mechanism, their conductivity is usually limited between 10^{-3} - 10^{-4} S/cm [57], [58]. While gel electrolytes may impart some additional flexibility to lithium ion batteries, it still employs a liquid solvent or liquid polymer which is still problematic. Due to the presence of hydrocarbon fluids, the risk of fire and drastic capacity fade seen in traditional batteries is left largely unaddressed.

A low glass transition temperature is essential for dry polymer electrolytes to have good flexibility and adhesion. It is not only important for having good mechanical properties, but essential for having reasonable ionic conductivities at ambient temperatures. Based on the past numerous studies it is widely understood that ion conduction occur predominantly in the amorphous region through large-chain segmental motion [59]–[61]. According to free-volume theory, when the polymer is below the glass transition temperature, the free-volume shrinks and the ions become localized in highly-ordered polymer chains, a state which results in a crystalline-like phase and low ionic conductivity [62, pp. 381–384]. As lithium salt addition increases,

the crystallinity of the host polymer decreases until it reaches a level of percolation. In the percolation region, the excess salts begin complexing with the host polymer in large concentrations, causing the polymer to stiffen and segmental motion of the polymer to be inhibited.

Most commercially available polymers do not have a glass transition temperature lower than 25° Celsius. Studies of commercial polymers have been typically limited to polyethylene oxide(PEO) and PVDF copolymers. PVDF copolymers have a higher solvation capability than PEO, but are often seldom used due to their large interfacial resistances and tendency to de-fluorinate when being cycled in the presence of lithium[63]. PEO has a long history in the polymer, electrochemistry, medical, and pharmaceutical fields, which is why it's often used as a reference when studying new solid state electrolytes or developing solid state batteries. PEO conducts ions through segmental motion. PEO moves lithium ions through intra-chain ion hopping (nearest solvation site) and inter-grain (chain to chain helix) hopping of its ether oxygens. As many as 4 - 6 oxygens can be bonded to the cation at a given time[64], [65]. However, a consequence of having these lithium ions solvate through the ether oxygens is that they tend to act as transient cross-linking sites, a mechanism which can stiffen the polymer and lower the ionic conductivity of the polymer. Accordingly, most salt-in-polymer systems are not composed of more than 30 weight percent in lithium salts.

Methods typically used to evaluate whether a polymer has been blended with too much lithium salt is to measure the glass transition temperature, the crystallinity, or if its vibrational state has changed. Techniques like Differential Scanning Calorimetry

(DSC) can be used to determine not only the glass transition temperature, but also to determine if the polymer's crystallinity has changed; a property which can be quantified by a shift in its enthalpy of fusion[66]. An alternative and more analytical technique that can be used to determine the change in crystallinity is Wide-Angle X-Ray Diffraction (WAXD) [66]. Another commonly used method for determining proper polymer/salt blending ratios is the measurement of the system's vibrational state using Fourier Transform Infrared Spectroscopy (FTIR).

The draw-back of using these salt-in polymer dry electrolytes is that they are often limited to ionic conductivities of $10^{-5} - 10^{-6}$ S/cm at room temperature and therefore have limited performance at ambient temperatures[67]. Because of the low ionic conductivity of polymer electrolytes, ways to increase the ionic conductivity have been continuously explored. One direction that has been extensively studied is to increase the lithium transport number [68]. The creation of a polymer electrolyte with a lithium transport number of 1 yields a system called a single-ion conducting polymer, a system where the anion is largely immobilized [69]. With the anions' steric effects hindered, it is believed that the cation would have increased mobility and therefore, higher ionic conductivity. Most research has been dedicated to crosslinking the anion to the polymer backbone in an effort to achieve single-ion conductors. Research in the single-ion polymer conductors is beyond the scope of this work.

The polymer-in-salt systems were first proposed by Angell's group and have shown to yield systems with ionic conductivities greater than 10^{-4} S/cm using PAN at room temperature[70]. In contrast with salt-in polymer electrolytes, the conduction

mechanism is believed to be different because of the systems' high cationic transport number and high ionic conductivity despite detection of large ion aggregates [67], [71]. Further evidence of the systems' different conduction mechanism is that the electrolytes have no abrupt change in ionic conductivity when operating below the glass transition temperature[72]. It has been proposed that its conduction is intrinsically liquid-like, where it is believed that the salt aggregates coordinate with all of the polymer's solvation sites, allowing for excess ions to migrate largely uninhibited.

1.5.4 Ceramic Electrolytes

Ceramic electrolytes are a promising class of solid state electrolytes because of their high ionic conductivities, absence of organic material, and are single-ion conductors [73]. Chemistries typically used for ceramic electrolytes are sulfides, oxides, phosphates, and have been reported to have ionic conductivities between $10^{-2} - 10^{-3}$ S/cm. With the absence of solvents, the risk of thermal runaway and subsequent fires is completely eliminated, this allows for high temperature operation.

For ceramic electrolytes, ion conduction is facilitated by the movement of point defects in the material. The continuous movement of point defects can be created through thermal excitation or an application of an electric field. The benefit of how ceramic electrolytes conduct, is that as single-ion conductors, concentration polarization at the electrodes' surface is largely mitigated. When there is concentration polarization, a battery's performance can be degraded under sustained operation. In traditional binary-electrolytes, the lithium anions can aggregate in the electrolyte or at the

electrodes' surface and create a blocking effect. As a result of the blocking from concentration polarization, the impedance can drastically increase, operating potential can decrease, and the discharge currents of a battery can alternate [74]. There are many different compositions of ceramics proposed, but they will not be discussed here; the merits and properties of LAGP are discussed later in the proceeding sections.

Despite the high ionic conductivity of ceramic electrolytes, there are drawbacks to using them in batteries. Ceramic electrolytes must be sintered into sheets which limit their configuration for commercial applications and prevent flexibility. In addition to the limited configuration, ceramics are brittle materials that can begin to fracture from thermal or mechanical shock. Many of the ceramic electrolytes tested have a fracture toughness of less than 1 MPa-m^{0.5} [75]. Examples of oxide, sulfide and phosphate electrolyte materials fracture toughness being tested are LLZO, LPS, and Li_{1.2}Zr_{1.9}Sr_{0.1}(PO₄)₃ respectively. LLZO has a fracture toughness of 0.86 MPa-m^{0.5}, LPS has a fracture toughness of 0.23 MPa-m^{0.5}, and Li_{1.2}Zr_{1.9}Sr_{0.1}(PO₄)₃ has a fracture toughness of 0.37 MPa-m^{0.5} [76]–[78]. A consequence of these porous and brittle materials is that they are unable to suppress the formation of lithium dendrites, a problem which can result in electrical shorts and self-discharge. Another challenge for ceramic electrolytes is being able to maintain good interfacial contact. Many electrodes have a reasonable amount of expansion and contraction during cycling, typical graphite electrodes can have a volumetric expansion as much as 12% [18]. This cyclic volume change of the electrodes can result in surface delamination of the electrolyte, which has limited

adhesive properties. Unfortunately, as a result of the physical limitations ceramic electrolytes have, they have very limited commercial applications.

1.5.5 Ceramic Composite Electrolytes

Ceramic electrolytes have high ionic conductivity at ambient temperatures, but they can fracture easily and have poor interfacial properties. Polymer electrolytes have low ionic conductivities, but under the right circumstances, can maintain a good interface with electrodes and can suppress lithium dendrites better than ceramic electrolytes. Individually, neither the polymer or ceramic electrolytes have the necessary properties to be commercially viable; both class of materials have their benefits and drawbacks. By combining both materials, researchers have looked for solutions that can transcend their individual constituents. As of recent memory, composite electrolytes have been explored to achieve electrolytes that are safer, flexible, and have high cycling efficiency.

There are currently two class of ceramic composite electrolytes researched, electrolytes that are blended active and inert ceramic fillers. Ceramic electrolytes, such as LLZO, LPS, LATP, and LAGP, are used as active fillers in polymer electrolytes. Some of the most commonly studied inert ceramic fillers are TiO_2 , Al_2O_3 , SiO_2 , and BaTiO_3 . Inert ceramic fillers, as the name suggests, are unable to conduct lithium ions.

Before there were super conducting ceramic electrolytes, most studies of ceramic composite electrolytes were dedicated to studying the effect these inert oxides had on polymers. For polymer electrolytes that were blended with inert filler at low

concentrations, the conductivity was reported to almost always increase. The increase in polymers' ionic conductivity has been attributed to the oxides inhibiting the crystallization of the polymers to create more amorphous conduction sites. The ability of the ceramic to inhibit crystallization is not only dependent on the material used, but the size of the particle. Nanometer sized particles are required to affect the crystallization[79]. In addition to requiring nanometer size particles, if too much of the inert filler is added to the polymer electrolytes, it begins decreasing the ionic conductivity because of its insulator-like properties. A table summarizing a few different published literatures on inert fillers at 25°C can be seen in **Table 2**.

Table 2: Ionic conductivities of inert fillers in composite electrolytes

Filler	Wt% Filler	Polymer	Salt	Polymer σ (S/cm)	Composite σ (S/cm)	Author
BaTiO ₃	15	PEO/PVDF	LiClO ₄	$.68 \times 10^{-4}$	1.2×10^{-4}	Kim[80]
TiO ₂	1.5	P(EO-EC)	LiCF ₃ SO ₃	3.2×10^{-5}	5.1×10^{-5}	Kwak[81]
SiO ₂	8	PEO	LiClO ₄	9.7×10^{-7}	9.5×10^{-5}	Mustarelli [82]
	8	PEO	LiTFSI	1.5×10^{-5}	8.2×10^{-5}	
Al ₂ O ₃	20	PEO	LiTF	1.0×10^{-6}	8.64×10^{-5}	Pumchusak [83]

While the contribution of conductivity from inert ceramic fillers is generally understood, the increase in conductivity for active fillers lacks a concrete narrative. As with inert fillers, an increase in conductivity is believed to be partly attributed to the increase in amorphous polymer content. The second contribution of conductivity of the active fillers is believed to be a contribution from the lithium that occupies the lattice structure of the fillers. The active filler is believed to not only act as an increase in charge carriers, but as sites that increase the mobility of lithium ions by acting as

additional solvation sites. There have been numerous studies that report adding high proportions of active filler content can increase the conductivity, but there have also been a few studies that report an increase in conductivity can only be achieved with small additions of ceramic filler. Up to date, there is not an agreement of how much the conductivity can increase with active fillers. For instance, LAGP/PEO composite electrolytes are reported to have an increase in conductivity by as many as two magnitudes at 25 °C by Kim’s group, but less than a quarter magnitude increase in ionic conductivity at 60 °C by Xu’s group [84], [85]. Xu’s group also tried using LGPS as the active filler, the group could only increase the conductivity using up to 10 wt% of material. Xu’s group found that at 1, 5, and 10 wt% the conductivity of the lithated polymer went up, but the highest was achieved using 1 wt%. Increasing the ceramics more than 1% began to reduce the ionic conductivity [86]. Another challenge with these active fillers is that researchers often have difficulty achieving the nanoparticle size required to lower the polymers’ crystallinity. A table summarizing a few different composite electrolytes utilizing active material can be found in **Table 3**.

Table 3: Ionic conductivities of active fillers in composite electrolytes

Filler	Wt% Filler	Polymer	Salt	Polymer σ (S/cm)	Composite σ (S/cm)	Author
LAGP	70	PEO	LiClO ₄	6.3×10^{-7} (25 °C)	1.0×10^{-5} (25 °C)	Kim[84]
LAGP	20	PEO	LiTFSI	4.29×10^{-4} (60 °C)	6.76×10^{-4} (60 °C)	Xu[85]
LATP (nano)	10	PEO	LiClO ₄	$\sim 8 \times 10^{-6}$ (20 °C)	5.97×10^{-5} (20 °C)	Kieffer[87]
LGPS	1	PEO	LiTFSI	6.16×10^{-6} (25 °C)	1.18×10^{-5} (25 °C)	Xu[86]
LLZO	52.5	PEO	LiClO ₄	$\sim 4 \times 10^{-6}$ (55 °C)	4.42×10^{-4} (55 °C)	Lee[88]
LLZTO	10	PEO	LiTFSI	$\sim 5 \times 10^{-6}$ (25 °C)	1.15×10^{-4} (25 °C)	Fan[89]

1.6 Summary

Traditional lithium-ion batteries are limited by their gravimetric energy density, safety, and long term performance. The most commercially used electrolyte in lithium-ion batteries are liquid electrolytes that are typically composed of carbonate solvents. The use of carbonate solvents and a number of the electrodes is that they are risk as imminent fire hazards. The fact remains, however, liquid electrolytes have high susceptibility to fires and can form a continuous passivation layer, which can result in the formation of alkali halides. The formation of a continuous passivation layer can lead to degraded performance and promote capacity fade.

1.7 Outline of this Thesis Research

Looking towards the future, solid state electrolytes have been proposed to rectify the issues that liquid electrolytes present. After reviewing the merits of polymer and ceramic electrolytes and the missing properties to meet modern requirements, this research is to systematically investigate a series of ceramic/polymer lithium-ion conducting composite electrolytes for potential application to all solid state lithium-ion batteries. The materials selected for study is the $\text{Li}_{1.4}\text{Al}_{0.4}\text{Ge}_{1.6}(\text{PO}_4)_3$ /lithiated polyethylene oxide (LAGP/PEO) with two different lithium salts, LiBF_4 and LITFSI.

In chapter 2, the synthesis and characterizations of LAGP was described. Utilizing x-ray diffraction (XRD), the purity of the LAGP is verified by comparing its spectra to reference literature. In addition, the conductivity of the synthesized LAGP as constituent powder and as a sintered ceramic pellet are determined using electrochemical

impedance spectroscopy (EIS). The conductivity and activation energy of the sintered and unsintered LAGP are compared against literature and the difference was discussed.

In chapter 3, the fabrication details, structural, morphological and thermal properties of LAGP/lithiated composite films are elaborated in details. Upon successful synthesis of the LAGP composite films, a select number of films are selected for XRD characterizations to determine the influence LAGP on the crystal structure of the lithiated polymer. Using differential scanning calorimetry (DSC), the thermal properties, i.e. melting temperature range of each film and composite film is determined. The morphological characteristics of the LiBF_4 composite films are discussed.

In chapter 4, the ionic conductivities in the temperature range of 25°C to 80°C of the LAGP composite films are systematically determined and analyzed. The impacts of adding LAGP and the difference between LiBF_4 series and LiTFSI series in terms of conductivities and conduction activation energies are discussed.

In chapter 5, the mechanical properties of the LAGP composite films are determined. The impacts of lithium-salt and LAGP on the film mechanical properties in terms of elastic modulus, ultimate strength, and failure strain are systematically investigated. The correlation between the ceramic particle size as well as distribution and the mechanical properties are also discussed.

In chapter 6, the merits of LAGP as a filler material are discussed. The effect of LAGP has on lithiated polymers' thermal, electrical, and mechanical properties are weighed. Areas that require further investigation are also discussed.

2 Synthesis and Characterization of LAGP Powders

2.1 Synthesis Process

ACS grade lithium carbonate (Li_2CO_3), aluminum hydroxide ($\text{Al}(\text{OH})_3$), and ammonium dihydrogen phosphate ($\text{NH}_4\text{H}_2\text{PO}_4$) were purchased from Sigma Aldrich; ACS grade germanium oxide (GeO_2) was purchased from Alfa Aesar. All chemicals were used without further purification or treatment. Solid reaction method was used to synthesize $\text{Li}_{1.4}\text{Al}_{0.4}\text{Ge}_{1.6}(\text{PO}_4)_3$ (LAGP) in 5 gram batches using the following stoichiometric ratios:



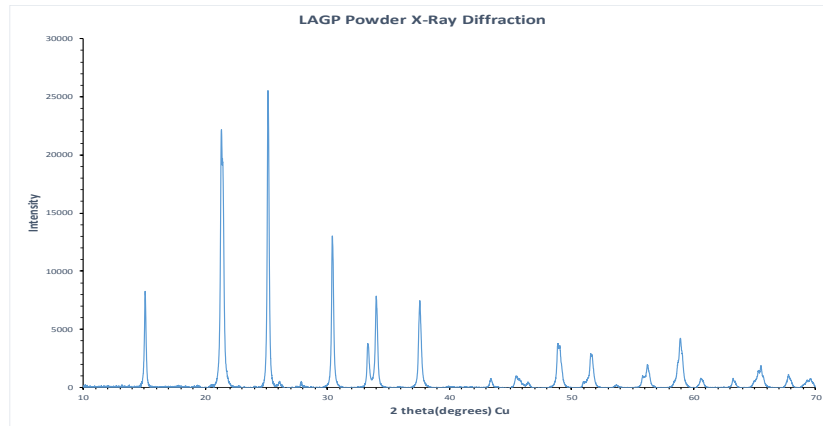
In a dry room, the reactants were mixed in an Agate mortar for 15 minutes. The mixture was then transferred to a borosilicate glass bottle and mixed on a ball mill without grinding media for at least 2 hours. The mixture was heated at two different conditions towards yielding the desired LAGP. The first heating treatment is to decompose any water, ammonia gas, and to ensure no side reactions happen during the formation of the oxide material. The mixture was transferred to a zirconia crucible and heated in a furnace at 600°C for 6 hours in air at a rate of 1°C per minute. The cooling rate was set at 3°C per minute. Upon completion of the first heating cycle, the mixture was milled in a high energy shaker mill for 3 hours. The milled material was subsequently transferred back to the zirconia crucible and fired at 900°C for 24 hours in

air. The temperature was raised slowly at a rate of 2°C/min and cooled at a rate of 3°C/min.

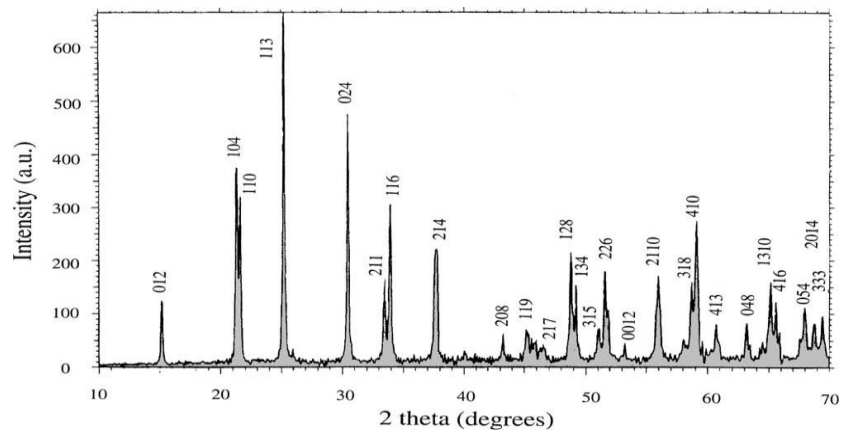
2.2 Structural Characteristics of LAGP

The as-prepared LAGP powders product was milled in an Agate mortar for 15 minutes before structural characterizations. X-ray diffraction spectroscopy (XRD) was used to determine the phase and purity of the material. The x-ray diffractometer used is Bruker XRD D8 with a Cu K α radiation tube and 1 mm slit. The scan range was set from 10° to 90° with a step size of 0.01° and a step scan of 1 second. During the measurement, the specimen was continuously rotated at 1.5 times per minute until the measurement was completed. The operating voltage is 40 kV and current is 40 mA.

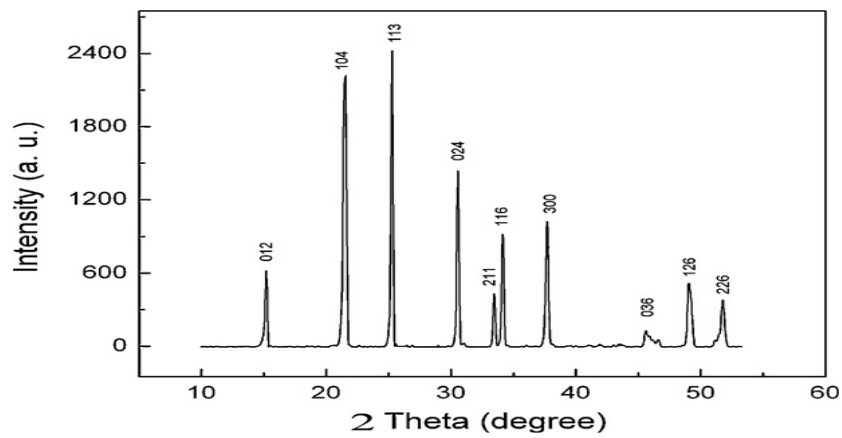
The representative x-ray diffraction spectrum of the LAGPs is shown in **Figure 3(a)**. Compared **Figures 3 (b) and (c)**, the positions of all the major peaks of the synthesized LAGP correspond well with the reference spectra of which our composition is derived [90]. The small peak at 26° corresponds to the trace of GeO₂ impurity [91].



(a)



(b)



(c)

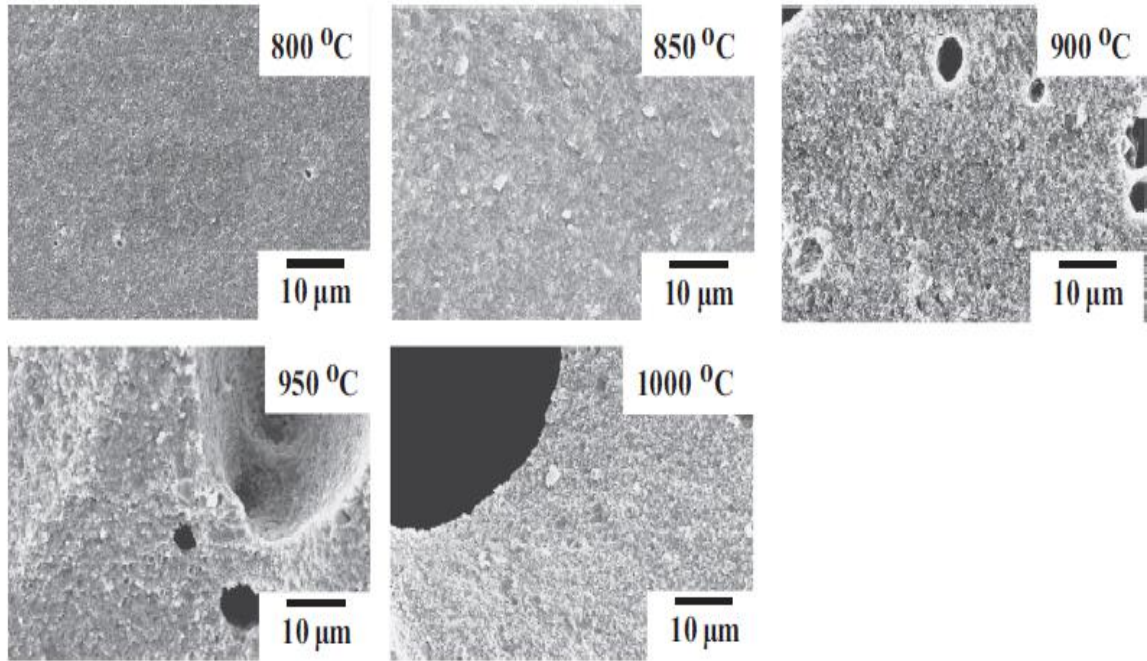
Figure 3: XRD spectra of LAGP synthesized in different laboratories (a) $\text{Li}_{1.4}\text{Al}_{0.4}\text{Ge}_{1.6}(\text{PO}_4)_3$ synthesized in our lab; (b) sintered at 1450°C and annealed at 650°C $\text{Li}_{1.4}\text{Al}_{0.4}\text{Ge}_{1.6}(\text{PO}_4)_3$ [90]; (c) $\text{Li}_{1.5}\text{Al}_{0.5}\text{Ge}_{1.6}(\text{PO}_4)_3$ calcined at 700°C and sintered at 900°C [92]

2.3 Ionic Conduction Characteristics of the LAGP

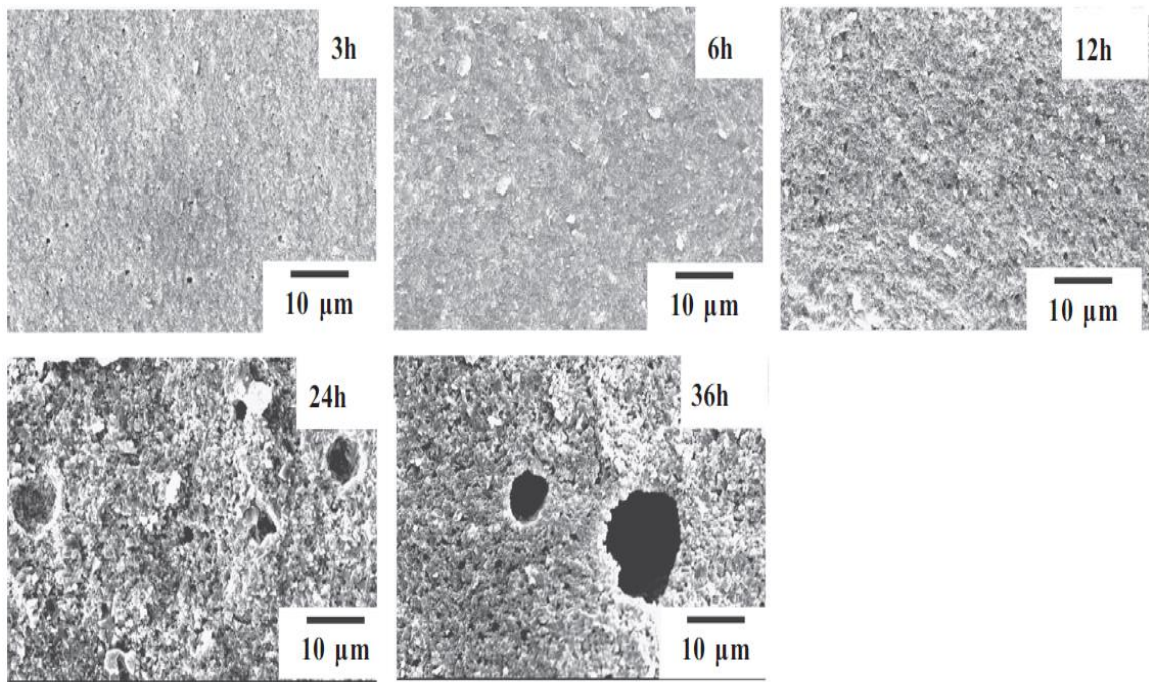
To determine the ionic conductivities of the LAGP products, the powders were pressed into pellets. Using a 13 mm pellet die set and without binder, the LAGP powders were pressed into pellets at a pressure of approximately 12,000 psi and kept under the constant pressure for 2 minutes.

Pellets were placed in the furnace at a temperature of 850° Celsius and ramped slowly at a rate of 0.5° C per minute and held isothermally for 12 hours. The sintered pellets were then carefully cooled down to room temperature at a rate of 1° Celsius per minute to prevent any cracks that may form due to thermal shock. The sintering parameters followed the previous work done by Kichambare and Kumar at the Air Force Research Laboratory.

Kotobuki et al [93] reported that sintering temperatures above 850°C not only yielded lower bulk ionic conductivities, but also resulted in large voids due to the reduction in volume that is accompanied by its crystallization. In addition to sintering temperature, sintering time was also found to be critical to void formation and ionic conductivity. **Figure 4 (a) and (b)** present a series SEM images showing the morphological changes with the sintering temperature and time. In agreement with Kichambare's results, Kotobuki found that sintering LAGP at 850° Celsius for 12 hours yielded the most optimal results on grain structure and ionic conductivity.



(a)



(b)

Figure 4: Cross-Sectional SEM Images of LAGP Pellets Calcined (a) at different temperatures for 6 hours; (b) at 850° Celsius for different times [93]

Electrochemical impedance spectroscopy (EIS) was used to derive resistances of LAGP pellets, from which ionic conductivities of LAGP pellets are determined. Sintered pellets were coated with silver paint (from Ted Pella) to function as working and blocking electrodes. Copper tapes were then attached to each Ag electrodes to wire the electricity out to the Gamry Potentiostat system. The samples were allowed to dry in the dry room for a day and then annealed at 105° Celsius for 2 hours to remove any residual solvent in silver paint. An image of a coated pellet ready for EIS is show in **Figure 5**.



Figure 5: A silver coated pellet with two copper electrodes for electrochemical impedance measurement.

The electrochemical impedance spectra of the LAGP pellets were obtained on Gamry Potentiostat Reference 600 with an AC amplitude of 100 mV in the frequency range of 1MHz to 1Hz and a sampling frequency of 50 points per decade. The

impedance spectra were recorded in the temperature range of 25 °C to 105 °C at an interval of 10 °C. The temperature was controlled in an automatic oven with presetting temperatures. The EIS measurement was started from high temperature to low temperature. The sample was held at the setting temperature for 1 hour prior to testing to ensure thermal equilibrium.

Representative EIS plots of a sintered pellets at the preset temperature are shown in **Figure 6**. Bulk resistance values were determined using a Randles equivalent circuit (see the inset) modified with a constant phase element.

From the LAGP electrolyte resistance values, conductivities were computed based on the pellet dimensions (thickness and base area of the pellet). At 25° Celsius the conductivity of our sintered LAGP was determined to be 1.72×10^{-4} S/cm. Unlike other researchers, it was difficult to develop an equivalent circuit model that could separate bulk and grain conductivity from the acquired EIS plots. The value obtained at room temperature is close to many published total conductivity values. The conductivities in the experimental temperature range closely match the total conductivities reported in literatures.

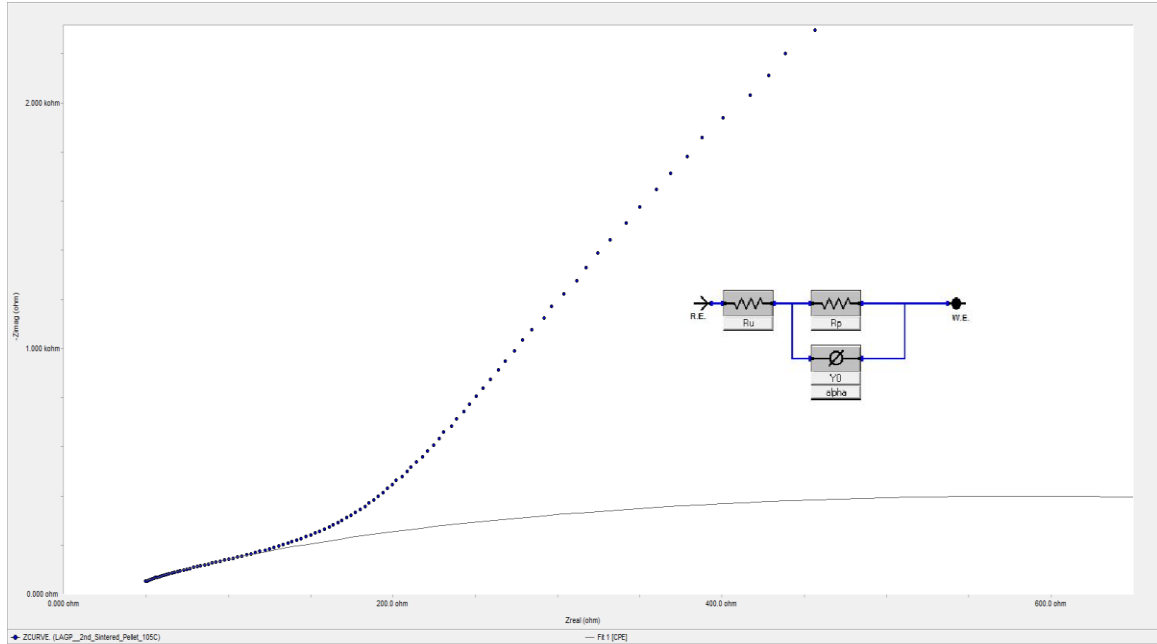


Figure 6: Electrochemical impedance spectra (Nyquist plots) of (a) sintered LAGP pellet at 105° C. The inset shows the Randles equivalent circuit used to derive the resistance of LAGP electrolyte for conductivity calculation.

The activation energy of the sintered LAGP pellet was calculated from the conductivity vs temperature plot shown in **Figure 7**, using a modified form of the Arrhenius equation [94, p. 192],

$$\sigma = Ae^{-\frac{E_a}{RT}}; \quad \text{Log}_{10}(\sigma) = -\frac{E_a}{2.3RT}$$

where the slope of the $\log \sigma$ vs. $1/T$ plot is equal to $-\frac{E_a}{2.3R}$ and R is equal to the gas constant 8.314 kJ/mol. The activation energy was calculated to be 27.5 kJ/mol, which is in close agreement with the activation energies reported as 28-30 kJ/mol.

Table 4 lists reported values of LAGP in terms of bulk conductivity, grain boundary conductivity, total conductivity and activation energies. The total ionic conductivity values are mostly in the order of magnitude of 10^{-4} S/cm at room temperatures [91], [93], [95]–[97]. The activation energy values varied from 28 to 45

kJ/mol, where the conductivity is found to be irrelevant to its variation. In addition to variations of LAGP in terms of composition, purity and crystallinity, measurement conditions resulting from facilities conducted at different laboratories will also introduce a certain range of errors.

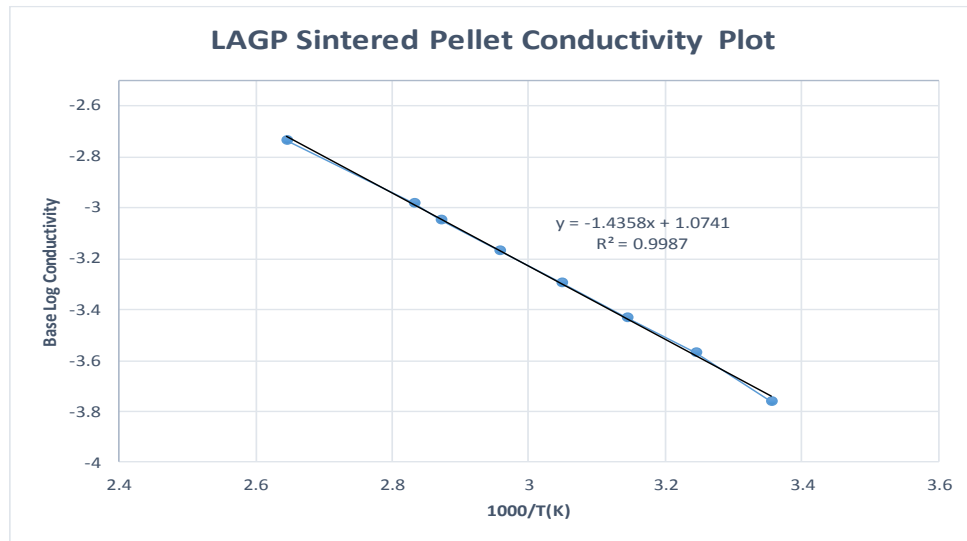


Figure 7: Arrhenius plot, logarithm conductivity vs. reciprocal of temperature, of sintered LAGP pellet

Leo was the first to report the performance of the LAGP composition we use, but the conductivities reported by Leo were determined using lithium electrodes[98]. It is now known however, that LAGP has a low electrochemical window against lithium, therefore it is inappropriate to determine lithium ion conductivity in LAGP using lithium foil as electrodes. It has been reported that LAGP has a redox window of -0.4 Volts to 0.6 Volts by Feng [99] and a window of -0.5 Volts to 0.7 Volts by Chen[100]. Experimental evidence of LAGP's instability against lithium is that its impedance increases substantially with time (a few hours) upon being in contact with lithium. The reported Nyquist plot can be seen in **Figure 8** [101]. As a consequence, lower

conductivity values were reported, e.g. 1.3×10^{-4} S/cm at 60 °C[98] and 3.8×10^{-5} S/cm at 40 °C[90].

Table 4: Ionic conductivities and activation energy values of LAGP reported in literatures.

Bulk Conductivity (S/cm) @25°C	Grain Boundary Conductivity (S/cm) @25°C	Total Conductivity (S/cm) @25°C	Activation Energy (kJ/mol)	Author
N/A	N/A	1.03×10^{-4}	44.38	Kichambare [95]
7.94×10^{-5}	N/A	10^{-4}	31.84	Arbi[96]
9.5×10^{-4}	N/A	1.8×10^{-4}	N/A	Kotobuki[93]
N/A	N/A	1.9×10^{-4}	39.56	Kang[91]
3.64×10^{-4}	4.68×10^{-3}	3.38×10^{-4}	30.57	Chi[97]
1.18×10^{-3}	N/A	7.25×10^{-4}	29.91	Wen[102]
N/A	N/A	4.23×10^{-3}	28.95	Kumar [103]
1.75×10^{-3}	4.3×10^{-3}	1.22×10^{-3}	31.1	Zhang[104]

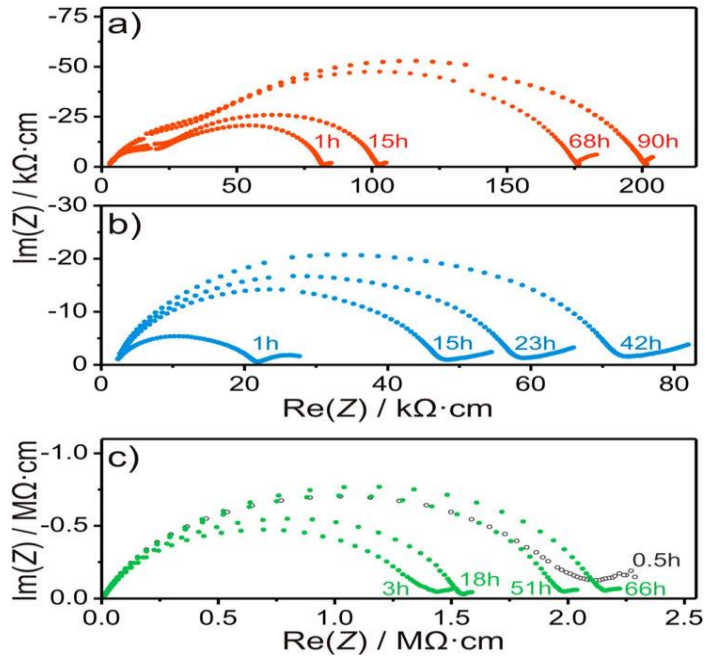


Figure 8: Impedance spectra of (a) LATGP, (b) LAGP, and (c) LATTP obtained using two lithium electrodes at 20° Celsius[101]

2.4 Summary

Using solid state reaction, $\text{Li}_{1.4}\text{Al}_{0.4}\text{Ge}_{1.6}(\text{PO}_4)_3$ (LAGP) powders were synthesized at 600° C for 6 hours following by 900° C for 24 hours in air at controlled at a slow ramping rate. With the help of XRD, the crystal structure and purity of the as-prepared LAGP was verified. Using EIS, the lithium ion conductivities was determined in the temperature range of 25 °C to 105 °C. Some LAGP powders were pressed into pellets and sintered at 850° Celsius for 12 hours. The sintered LAGP pellets' conductivity was determined to be 1.72×10^{-4} S/cm at 25 °C. The activation energies for the sintered pellet is 27.5 kJ/mol. The activation energy and conductivity of the sintered LAGP pellet falls within the range of reported values seen in literature.

3 Fabrication and Characterizations of LAGP/PEO/Li-salt

Composite Electrolyte Membranes

3.1 LAGP/PEO/LiBF₄ Composite Film Compositions

Most dry polymer electrolytes often use LiTFSI, LiTF, LiClO₄, or LiPF₆ as their lithium salt. After a preliminary literature review, it was determined that LiBF₄ is not a well characterized salt in polymer electrolytes, let alone PEO. In particular, there has been little to none in terms of the number of studies that has utilized LiBF₄ salt in LAGP composite films. Lastly, LiBF₄ has been known to have excellent high capacity retention, low charge transfer resistance, and low voltage hysteresis gain in carbonate solvents at temperatures as low as -30° Celsius when compared against LiPF₆ salt [105]. LiBF₄ has one of the highest ionic conductivities in liquid electrolytes. The aforementioned material properties and lack of studies led us to believe that this salt was fertile territory to be explored for use in our composite electrolytes.

Based on FTIR studies, it was found that for PEO with an EO:Li molar ratio of 8: 1 yields the most conducting polymer films[106]. Keeping the molar proportions of the salt and polymer constant, a series of composite films were fabricated in sequentially increasing weight proportions of LAGP relative to PEO. The amount of each component used in the composite membrane is listed in **Table 5**.

Table 5: The amount of each component used to fabricate the LAGP/PEO/LiBF₄ series

Composition	LAGP(g)	PEO(g)	LiBF ₄ (g)	Moles PEO	Moles Li	EO:Li Ratio
PEO	0	0.75	0.200	0.01704	0.00213	7.9876
LAGP-20	0.15	0.6	0.160	0.01363	0.00171	7.9876
LAGP-30	0.225	0.525	0.140	0.01193	0.00149	7.9876
LAGP-40	0.3	0.45	0.120	0.01022	0.00128	7.9876
LAGP-50	0.375	0.375	0.100	0.00852	0.00107	7.9876
LAGP-60	0.5625	0.375	0.100	0.00852	0.00107	7.9876

3.2 LAGP/PEO/LiTFSI Composite Film Compositions

For comparison, LiTFSI-based composite films were also fabricated and characterized. LiTFSI/PEO polymer electrolyte system has been studied previously. Hence, it can serve as a reference to gain insight in the impacts of Li-salt in polymer electrolyte system. Moreover, there is no extensive research on LAGP/PEO/LiTFSI composite electrolytes, and there is no any report in such system with LAGP in the weigh percentage of 20 - 60%. In this study, we will systematically investigate LAGP/PEO/LiTFSI system and compare with LAGP/PEO/LiBF₄ system .

Literature and researchers suggest that the optimal molar ratio for PEO and LiTFSI is a 10:1 ratio for highest conductivity [107]. However, our experimental results showed that a free-standing polymer film could not be fabricated at this composition at room temperature. Accordingly, a molar ratio of polymer to lithium was adjusted 20:1. As with the LiBF₄ composite films, the molar proportions of the salt and polymer were held constant. A series of composite films were fabricated in sequentially increasing

weight proportions of LAGP relative to PEO. The amount of each component used in the composite membrane is listed in **Table 6**.

Table 6: The amount of each component used to fabricate the LAGP/PEO/LiTFSI series

Composition	LAGP(g)	PEO(g)	LiTFSI(g)	Moles PEO	Moles Li	EO:Li Ratio
PEO	0.0000	0.7500	0.2440	0.0170	0.0008	20.0465
LAGP-20	0.1500	0.6000	0.1952	0.0136	0.0007	20.0465
LAGP-30	0.2250	0.5250	0.1708	0.0119	0.0006	20.0465
LAGP-50	0.3750	0.3750	0.1220	0.0085	0.0004	20.0465
LAGP-60	0.5625	0.3750	0.1220	0.0085	0.0004	20.0465

3.3 Fabrication of LAGP/PEO/Li-salt Composite Electrolyte Membranes

Anhydrous acetonitrile, polyethylene oxide (molecular weight of 400,000), lithium tetrafluoroborate (LiBF_4), and lithium bis(trifluoromethanesulf)imide (LiTFSI) were purchased from Sigma Aldrich. All chemicals are ACS grade and used without further purification. All chemicals were opened and used in conditions where the relative humidity was less than 1%. The acetonitrile was opened in a dry room and stored in a sealed polyethylene bag inside a dry room. LiBF_4 , LiTFSI, and PEO were opened and stored in an argon filled glove-box.

For the use in composite polymer electrolyte membranes, the as-synthesized LAGP powders, as described in the previous section, were further milled in a high energy shaker mill until the average particle size was submicron. Particle size was determined by SEM. Some agglomerates in the micron range were observed.

In the dry room, 15 mL of acetonitrile is measured using a graduated cylinder and poured into a borosilicate glass bottle. An appropriate amount of LAGP is added to acetonitrile. The suspension solution is subsequently sonicated for an hour using an average power of 4-5 J/s to break up LAGP agglomerates and to facilitate the dispersion of the LAGP. With the solution cooled and the bottle sealed, it is transferred to the argon filled glove-box. At room temperature, pre-weighed lithium salt was added while the solution was continuously stirred. After the salt was dissolved, the solution temperature was raised to 50°C and pre-weighed PEO was added to the solution and sealed. The solution was allowed to stir at medium speed 500-600 RPM for 4 days and the solution was cast on the 5th day in a Teflon dish.

When casting the solution to the Teflon dish, care needs to be taken to ensure the solution overcomes any surface tension and to eliminate the formation of air bubbles. Afterwards, there are three drying stages throughout the membrane fabrication procedure.

In the first stage of drying, the solution was placed in a close to zero flow (quiescent) environment with a pressure of 1 kPa (in the antechamber of the glove-box) until the viscosity reached approximately 1000 cp. Several preliminary viscosity tests were performed to determine the time required to reach the necessary viscosity. The solution was re-agitated in regularly timed intervals to make sure the film stayed a uniform thickness. After the solution reached the desired viscosity, the solution was no longer re-agitated.

The second stage of drying was to allow slow crystallization of the polymer and evaporation of the solvent to yield a homogenous film. During this stage, the Teflon dish containing the viscous solution was stored inside the antechamber at a sealing pressure of 1 KPa for 4 hours.

The third and final stage was to dry the membrane in the glove-box under circulating argon. At this stage, the drying time for LiBF₄ films is 24 hours before film removal and storing. The drying time for LiTFSI films is 72- 84 hrs in total. After 24-36 hours, the film was removed from the Teflon dish, laid on their front side and allowed to dry an additional 48 hours before taken out of glove box for bagging.

The as-fabricated LAGP/PEO/Li-salt composite membranes were stored in vacuum bags and sealed with a hot press. All films were stored in the glove-box and in darkness prior to use. Separate films for mechanical testing were made and stored at least two weeks prior to testing.

3.4 Structural Characterization of the Composite Films

A selected number of composite films were studied using XRD to see the potential influence of LAGP on the crystallographic structure of PEO films. To reduce the possibility of the lithiated polymers being complexed or broken down by the moisture from ambient air, samples were encapsulated in a special Bruker made holder. The analyzed samples were placed on a zero-diffraction plate and sealed with a Kapton film and thermoplastic gasket. A image of the specimen holder can be seen in **Figure 9**.



Figure 9: Kapton Bruker Film Holder used for XRD measurement of the composite membrane

Using a Cu K α radiation tube, 0.6 mm slit, and solar diffraction grating, samples were analyzed from 10 $^\circ$ to 80 $^\circ$ with a step size of 0.01 $^\circ$ and a step scan of 1 second. The specimen on a platform was continuously rotated 1.5 times per minute until the measurement was completed. The constant rotation of the films during measurement helps eliminate any bias that may arise from surface defects in a process that is similar to a raster. The operating voltage is 40 kV and current is 40 mA.

The X-ray diffraction data was processed using MATLAB and piecewise *Robust Local Regression* was performed in order to establish a baseline for which the data could be normalized. After data was normalized, application factors were calculated by taking the ratio of the largest detected peak and smallest detected peak so that they could be plotted on the same intensity scale.

Figure 10 presents the XRD spectra of LAGP/PEO/LiTFSI series with LAGP content of 20wt%, 30wt%, 50 wt%, and 60 wt% in comparison with LAGP powders and PEO.

From results, it appears that the addition of LAGP had no significant effect on the crystallinity of PEO because no peak broadening was observed.

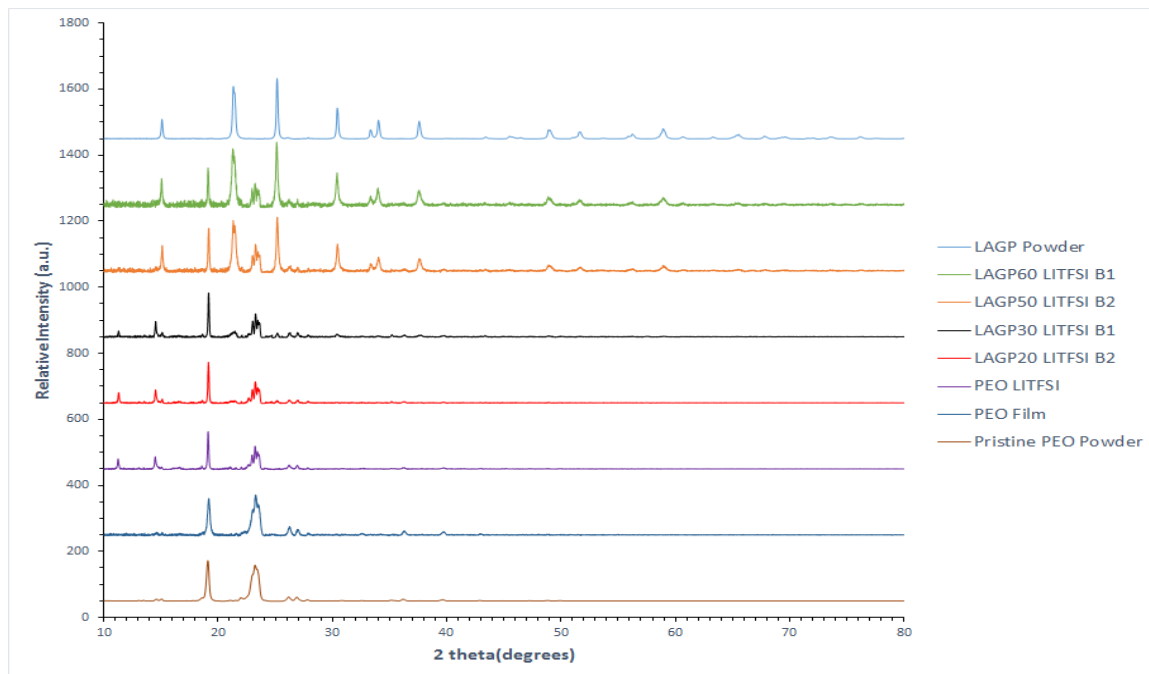


Figure 10: XRD patterns of the LAGP/PEO/LiTFSI series in comparison with LAGP powders and PEO.

3.5 Thermal Characterizations of the Composite Films

To understand the thermal properties and stabilities, the composite films were subjected to Differential Scanning Calorimetry (DSC) analysis. The composite films were punched and loaded in special hermetically sealed Al pans in a dry room. Punched samples were an average weight of 5 to 15 mg. The DSC spectra were recorded using TA Instruments DSC 2010 from room temperature to 200° Celsius at a rate of 5°/min.

DSC results for LiBF₄ and LiTFSI composite films can be seen in **Figure 11 (a)** and **(b)** respectively. For the LiBF₄ composite films it appears that there is no change in the

melting temperature as LAGP content increases; a similar assessment can be made of the LiTFSI composite films.

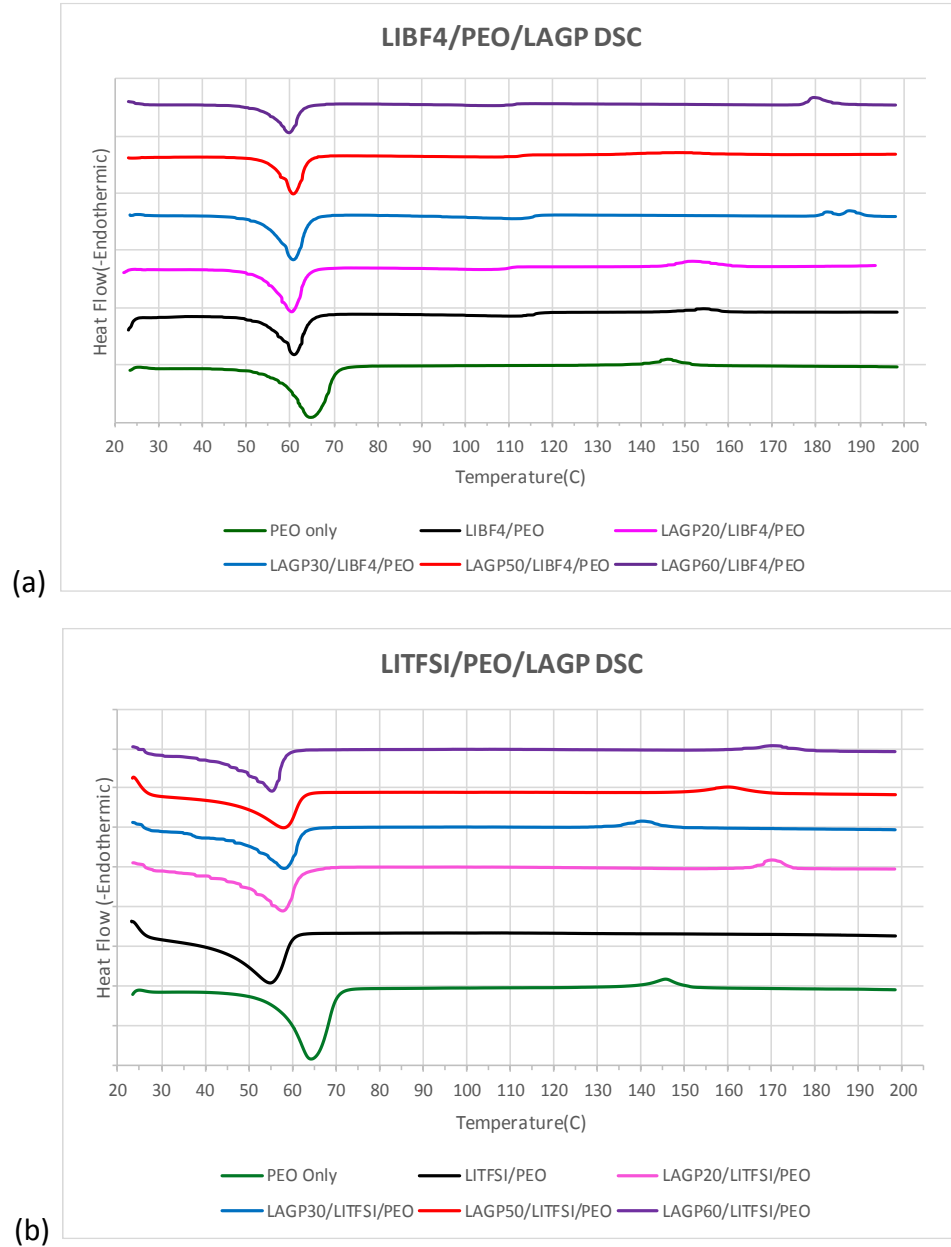
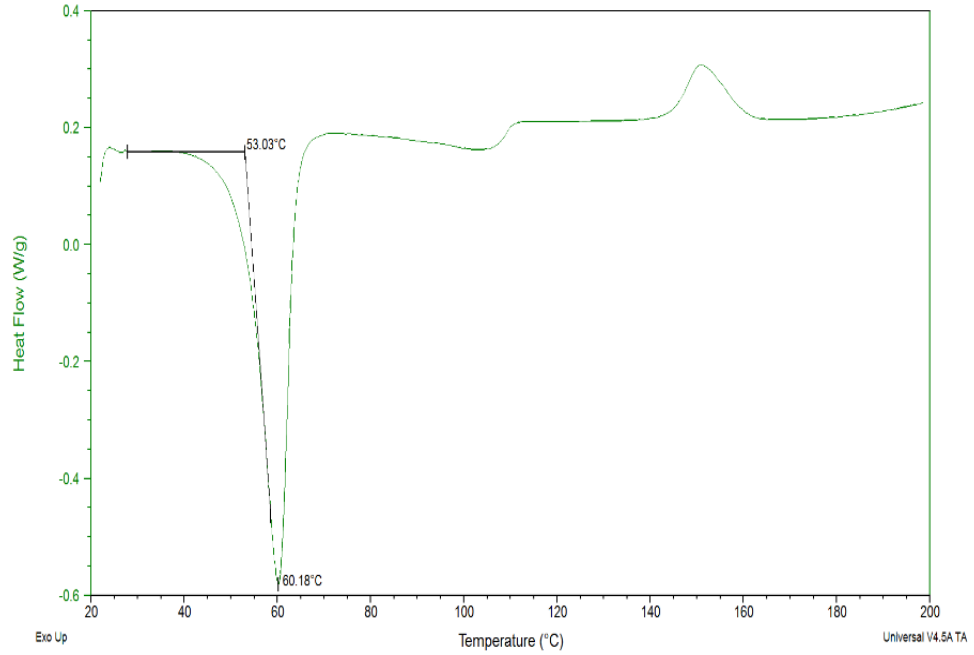


Figure 11: DSC profiles obtained from (a) LAGP/PEO/LiBF₄; (b) LAGP/PEO LiTFSI Composite Films

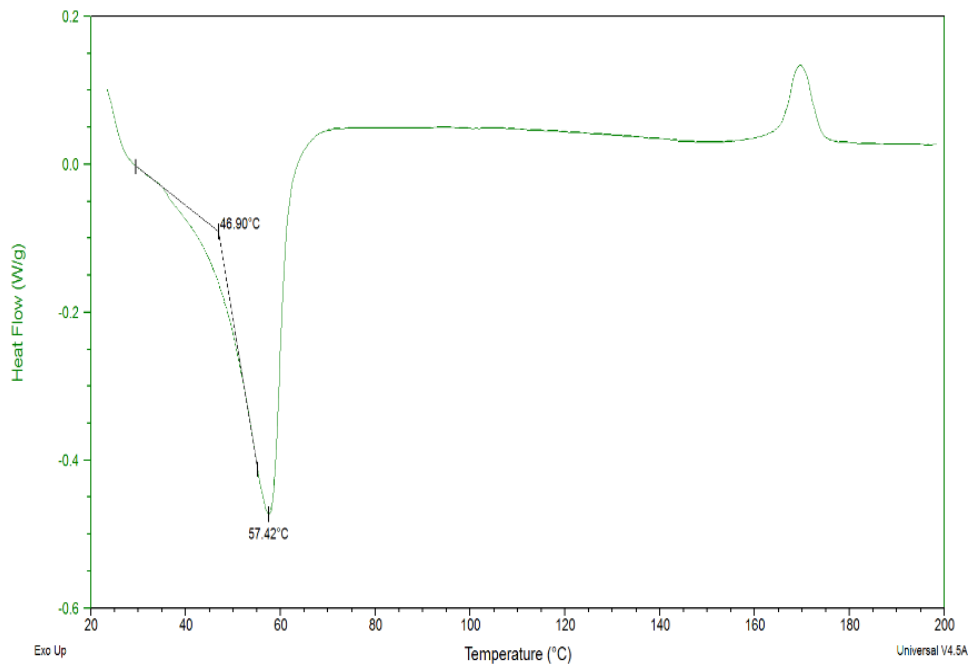
Using TA Instruments Universal Analysis software, the melting temperature range of each composition was determined. The method used to determine the starting

melting temperature was onset point method. Onset point temperature analysis determines the value by using the baseline reference and the tangential line of when enthalpy changes are detected, choosing the coordinate at which both lines would intercept if they approached infinity. To determine what the final melting temperature was in the different compositions, simple max peak analysis was used. When a material is undergoing a phase change, its temperature will not change until the phase transformation is complete. When the phase change is completed, the temperature will begin to increase again; this is where the final monomer should have changed from a solid to a fluid. Most polymers have a Weibull distribution of molecular weights and accordingly, the polymers will have a bin range for their melting temperature.

Two representative DSC thermographs of an LAGP20/PEO/LiBF₄ and LAGP20/PEO/LiTFSI composite electrolyte being processed to determine their melting temperatures can be seen in **Figure 12 (a)** and **(b)**, respectively. For the LiBF₄ series, the baseline used is a horizontal line. For the LiTFSI series there was no flat baseline to reference; this may be due to the fact that the true onset melting temperature is very close to STP conditions. Hence, the data points before an abrupt change in the slope of the plot was used as the baseline.



(a)

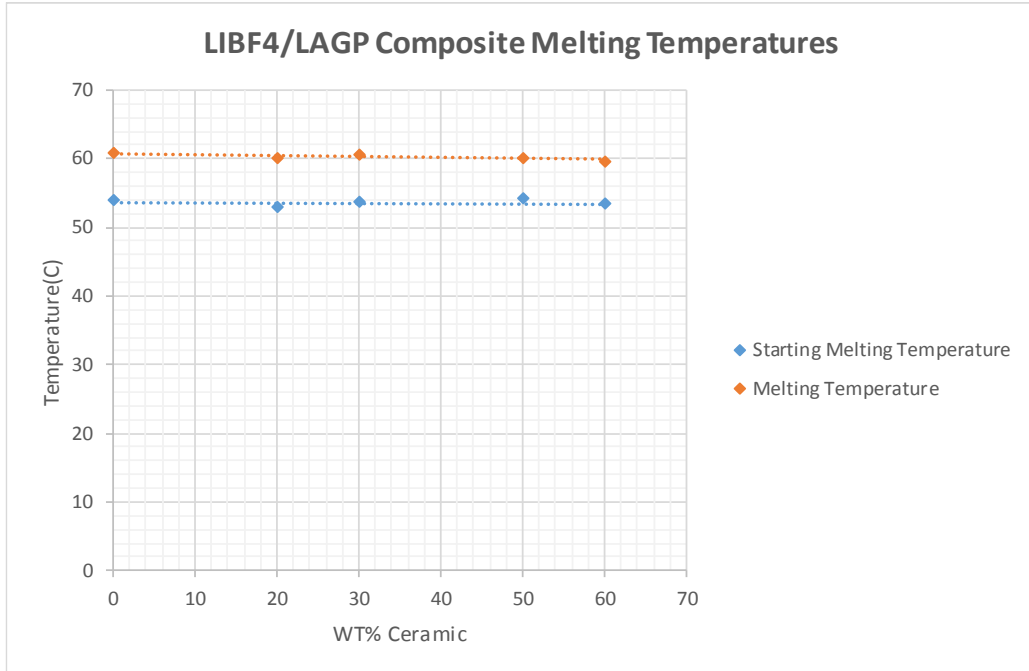


(b)

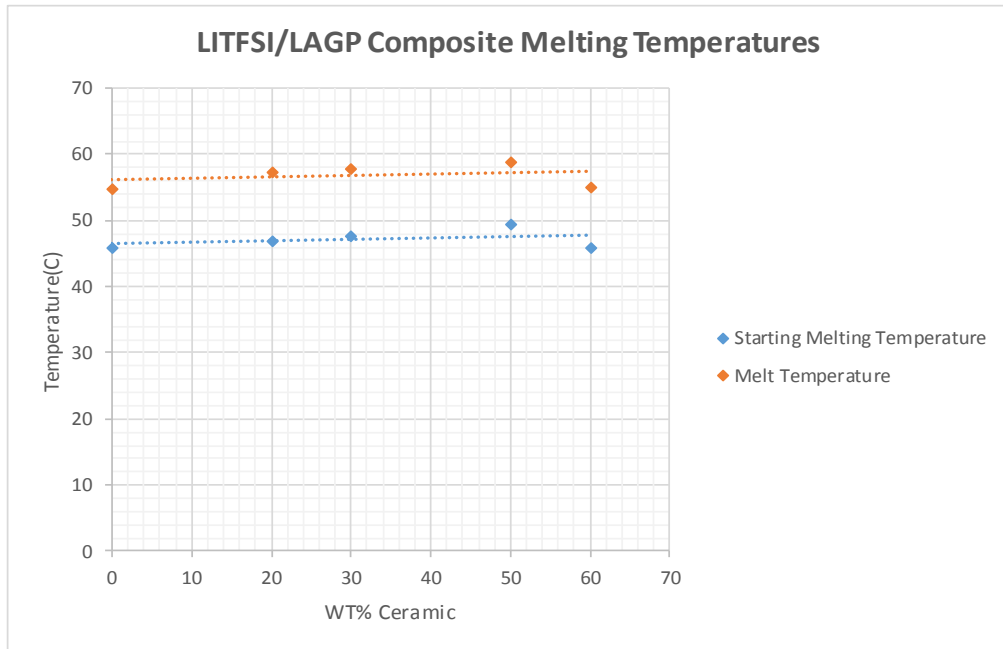
Figure 12: Selection of the onsite melting temperature for analysis (a) in LAGP/PEO/LiBF₄ composite system; (b) in LAGP/PEO/LiTFSI composite system

A summary of the melting temperatures as a function of LAGP content for the LiBF_4 and LiTFSI series can be seen in **Figure 13 (a)** and **(b)**, respectively. For both salt compositions, adding lithium salt into polymer decreases the melting temperature. The melting temperature of lithiated polymers remained relatively unaffected by the addition of LAGP. The average melting temperature range for LiBF_4 films is $53.67^\circ - 60.23^\circ$ Celsius. The average melting temperature range for the LiTFSI films is $45.52^\circ - 56.46^\circ$ Celsius.

The relatively stable melting temperature might be attributed to the particle size used to create the composites. It has been reported that the crystallinity of polymers can only be affected by the ceramic particles of several hundred to tens of nanometers. As seen in the XRD scans carried out on the LiBF_4 composite films, there was no observable broadening of polymer peaks to indicate a crystallinity decrease. Without a change in the crystallinity or the use of a plasticizer, the temperature at which a polymer should undergo a liquid transition should remain relatively unchanged.



(a)



(b)

Figure 13: Melting temperature and onsite melting temperature as a function of LAGP content in (a) LAGP/PEO/LiBF₄ series; (b) in LAGP/PEO/LiTFSI series.

3.6 Surface Morphological Imaging of the Composite Films

To visualize the particle size and distribution in the composite films, scanning electron microscopic analysis was performed. Some imaging was performed on JEOL SEM, and the specimens were coated with a few nm thick gold to dissipate the charges. Majority of the top-view and cross-view imaging was performed on FEI Lyra SEM/FIB dual-beam system. For top view imaging, there is no any coating on specimen. For FIB processing to facilitate cross-view imaging, the films were coated tens of nanometer Ir or Au as conductive layers.

The following images (**Figure 14**) present top view of as-prepared LiBF_4 film series. LAGP particles cover/embedded in PEO matrix can be seen on the surface in the composite films. More LAGP particles can be seen upon increasing LAGP content. It is also noted that most LAGP particles are in sub-micrometer scale with some agglomerates as large as 3 micrometers, although BET calculations suggests particle size of 1-3 micrometer. More SEM images will be presented and discussed in chapter 5 to correlate with the mechanical properties of the films.

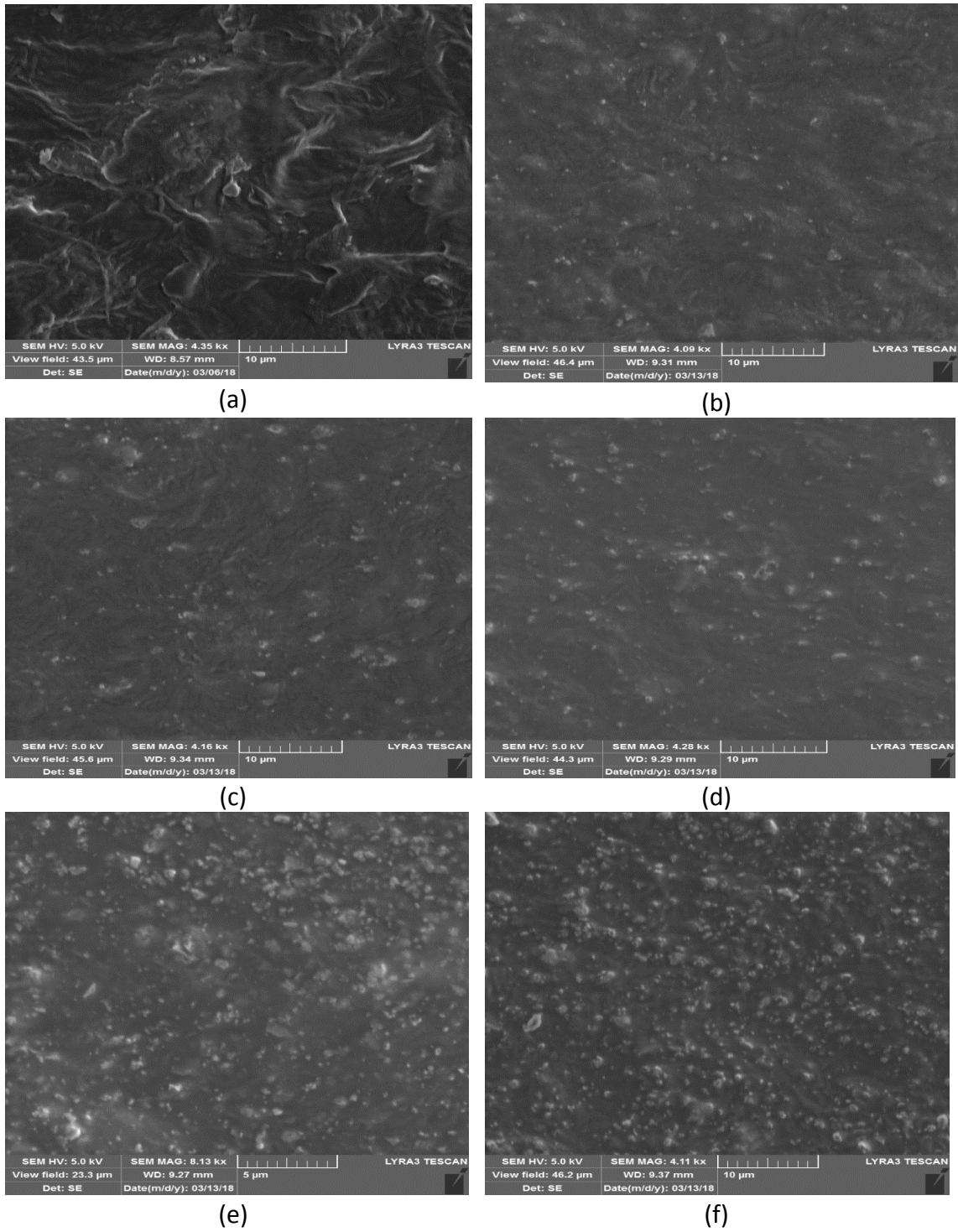


Figure 14: Top-view SEM images showing the surface morphologies and LAGP distribution in the LiBF₄ film series (a) PEO; (b) LAGP20; (c) LAGP30; (d) LAGP40; (e) LAGP50; (f) LAGP60

3.7 Summary

LAGP/PEO/Li-salt composite free-standing films were successfully fabricated using two different salts, i.e. LiTFSI and LiBF₄ with LAGP content in the range of 20-60 wt%, which have not been reported publicly. A 20:1 and 8:1 monomer to salt ratio were used for LiTFSI and LiBF₄ series, respectively.

Based on XRD and DSC results there appears to be no significant change in the crystallinity of the host polymers with increased LAGP addition. The consequence of having no change in the amorphous content of the lithiated polymers is that the conduction through the polymer should be relatively the same.

For both salt compositions, adding lithium salt increased the melting temperature of PEO. In LiBF₄ series, the proportions of LAGP has slightly reduced the melting temperatures of the lithiated polymers; while in LiTFSI series, the proportions of LAGP has slightly increased the melting temperatures of the lithiated polymers. The average melting temperature range for LiBF₄ films is 53.67° – 60.23° Celsius. The average melting temperature range for the LiTFSI films is 45.52° – 56.46° Celsius. LiTFSI has a greater plasticizing effect on PEO than the LiBF₄ salt.

Top-view micrographs of the as-prepared composite films showing LAGP fine particles relatively homogeneously distributed throughout PEO matrix. The size of LAGP particles are in the range of submicron to a few micrometers.

4 Ionic Conduction of the Composite Films

4.1 EIS Results Using Stainless Steel Electrodes

Preliminary studies and literature review were performed prior to deciding what materials would be used as the blocking electrodes for the polymer electrolyte composites to perform electrochemical impedance spectroscopy (EIS). LAGP composites studied by other groups utilized stainless steel as their blocking electrodes by means of compression fixture or coin cell batteries. The benefit of using a material such as stainless steel is that it is an inert material and as a result, can simplify the analysis of the electrolyte. Ideally, the only characteristics that should be detected are ohmic impedance from electrolyte.

Practically, in heterogeneous electrochemical systems, equipment inductance, contact resistance, electrolyte conduction, double layer charging, and charge transfer resistance can be detected by EIS. Without performing other in-situ experiments, information collected by EIS can be complex. For instance, by placing an electrolyte between two current collectors, the system can give rise to a double-layer charging and electrode/interface polarization in addition to electrolyte conduction. When the interface impedance exceeds the bulk electrolyte impedance and the characteristics frequency overlaps, the electrolyte impedance information can be completely overshadowed.

In this study, LAGP20, LAGP30, and LAGP70 - LiBF₄ films were tested against stainless steel electrodes. The EIS spectra obtained from the LAGP20 films at 25° C and 80° C can be seen in **Figure 15 (a)** and **(b)**. The intercept at the high frequencies usually associated with the total resistance from electrolyte. However, as seen in **Figure 15 (a)**, at 25 °C, the high interface impedance up to 100 kohm overshadowed the electrolyte impedance which should be in the kohm range. When the temperature increased above the melting point of the polymer, e.g. 80° C, the high frequency intercept becomes visible and the electrolyte resistance can be readily determined, which is 108 ohm.

Another EIS experiment using the composite membranes of different thicknesses vindicated further the occurrence of the overlapping between electrolyte impedance and interface polarization impedance at low temperatures. In this experiment, two stainless steel coin cells were fabricated using the same LAGP30/PEO/LiBF₄ electrolyte but different number of layers. The thicknesses of the two electrolytes are 415 microns and 127 microns, respectively. Both films were annealed at 80° Celsius for 1 hour prior to cooling down to 25° Celsius for 1 hour. After measurements were taken, both coin cells were de-crimped to confirm that the multilayers of electrolyte were indeed melted to form one continuous layer. As seen in **Figure 16**, despite being more than 3 times thicker than the 127 micron electrolyte, the first non-zero intercepts in Nyquist plot of the 415 micron thick electrolyte only differed by a fraction of the 127 micron electrolyte. The impedance value does not reflect linear relationship with the electrolyte thickness indicated that the values from the semicircle originated both from electrolyte and interface impedances.

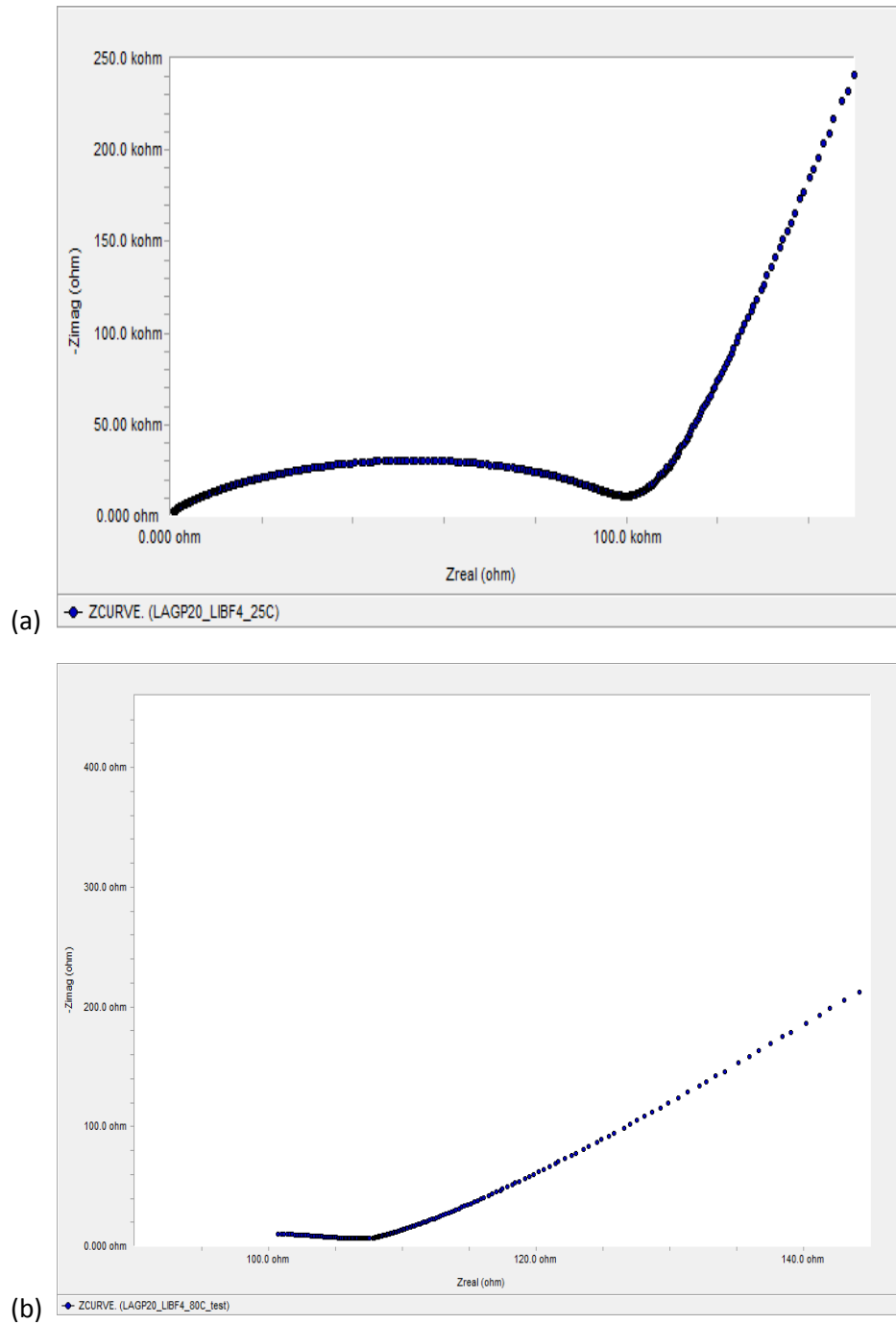


Figure 15: Nyquist impedance plot of LAGP20/LiBF₄ Composite obtained at (a) 25° Celsius (b) 80° Celsius using two stainless steel electrodes

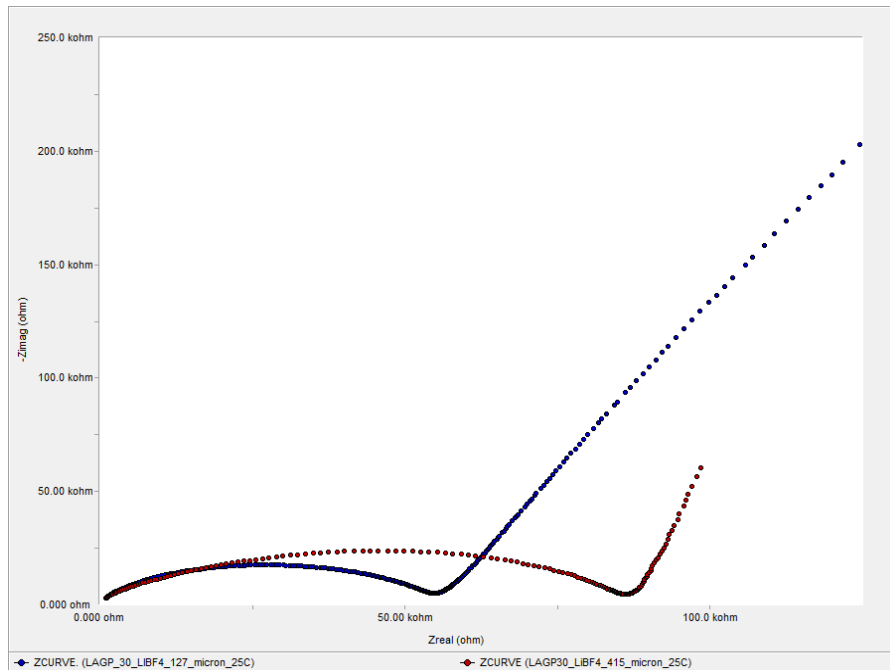


Figure 16: Nyquist Plot of LAGP30/LiBF₄ Composite Electrolytes of two different thickness, 127 microns and 415 microns, using stainless steel electrodes

Although the spectra can be fitted using equivalent circuit, from which the electrolyte resistance and conductivity can be derived, relatively large errors may be resulted. A summary of the conductivities of LAGP/PEO/LiBF₄ films tested using stainless steel electrodes is presented in **Figure 17**. The results carried out from these experiments were not fruitful or accurate when compared against literature[84]. It is submitted that stainless steel is not an ideal choice of electrode to ascertain the impedance of the studied composite electrolyte systems, especially at temperature below the polymer melting point.

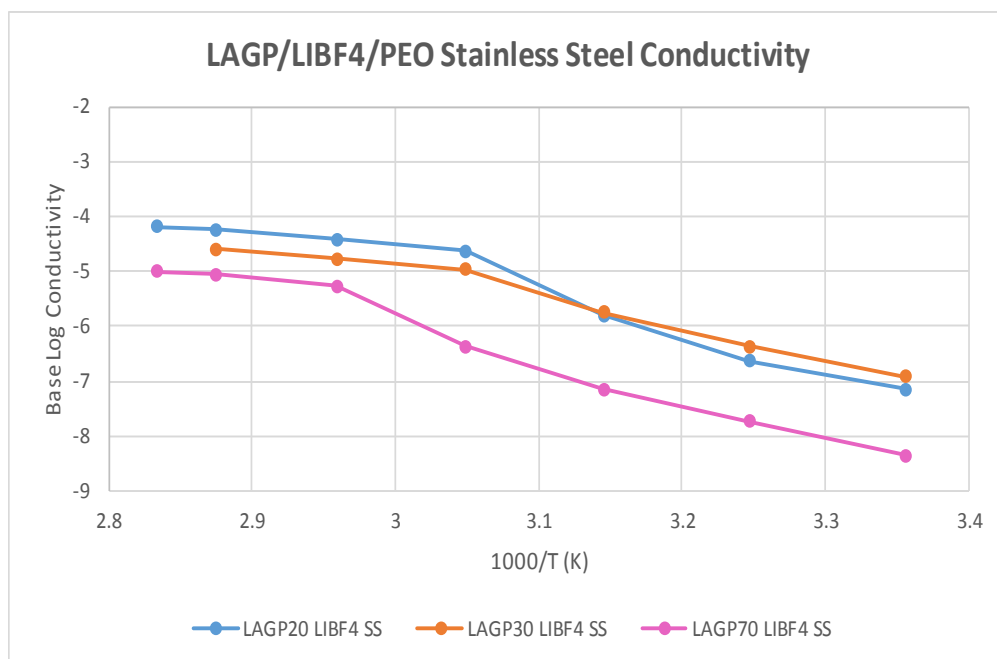


Figure 17: Arrhenius conductivity plot of LAGP/PEO/LiBF4 samples obtained using stainless steel.

4.2 EIS Results Using Lithium Electrodes

In addition to stainless steel, different electrode/substrates such as aluminum, copper, gold, silver, and lithium were assessed to see if the electrolyte impedance could be de-coupled from the interfacial impedance. Silver, gold, and lithium yielded results that were sufficient for decoupling at room temperature, which is due to the better interfacial contact with the electrolyte film. Either gold or silver, to be used as blocking electrodes, needs to be sputtered or pasted onto the electrolyte. When annealing samples above the melting point of the polymer, samples began to irreversibly short-circuit. Therefore, lithium foil was chosen to characterize ionic conduction of the composite films.

Lithium is stable against lithiated PEO from at least 0 to 4.25 Volts and PEO may serve as a buffer layer between the LAGP and lithium foil [44], [85], [108]. In this study,

3/4" electrolyte samples were assembled in an argon filled glove box between two 5/8" lithium foils in a CR2032 coin cell configuration shown in **Figure 18**.

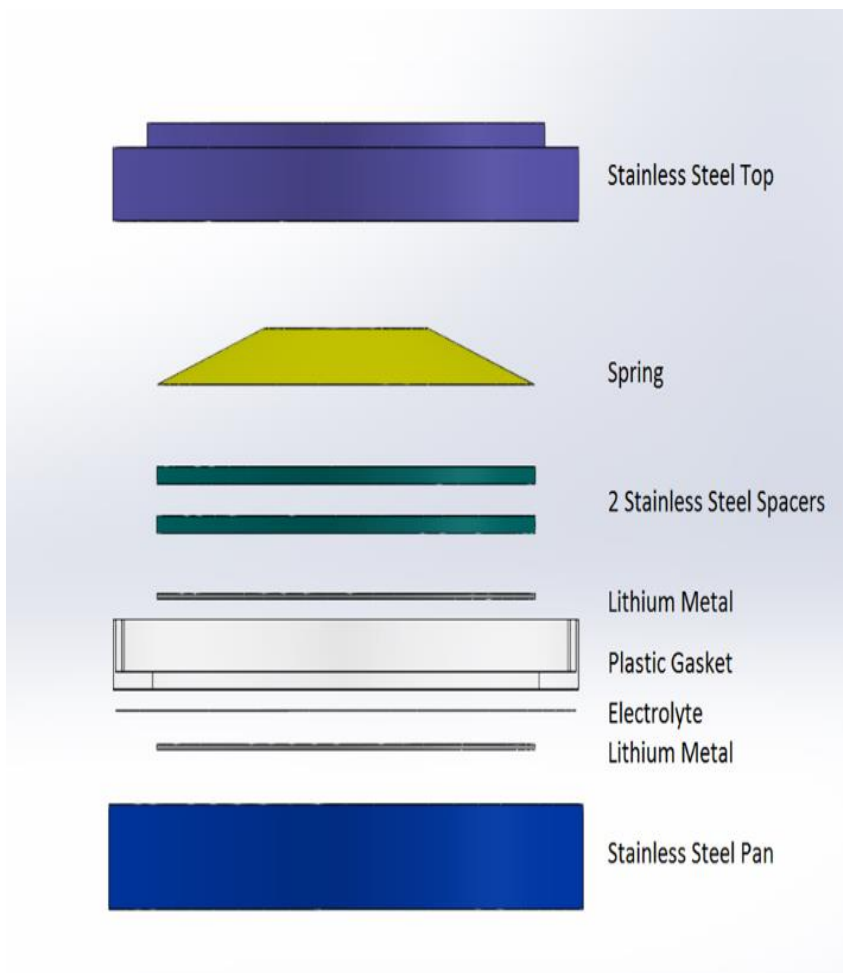


Figure 18: A Schematic of Coin Cell Assembly For Electrochemical Characterization

For the LiBF_4 films, samples were annealed at 80°C for 1 hour prior to cooling them, EIS measurements were taken after each new temperature was reached and held isothermally for at least 1 hour using an AC voltage of 100 mV with or without DC polarization. In some samples, thermal treatment was conducted to investigate the stability of the composite electrolyte against lithium foils.

EIS carried out on the LAGP20/LiBF₄ film at 35°C using an AC voltage of 100 mV and DC voltages ranging from 0 to 750 mV are shown in **Figure 19**. Compare with the spectra obtained using stainless steel electrodes, the EIS spectra using lithium foils become well separated two semicircles corresponding interfacial polarization impedance and ionic conducting impedance in the electrolyte. Moreover, the interface impedance reduces to a few thousand ohms, which is two orders of magnitude lower than using stainless steel electrodes. Further, the influence of the dc polarization of the EIS was studied. As DC voltage increased from 0V to 700mV, it is clear that resistance from the low frequency semicircle reduces, confirming it originates from the electrode kinetic polarization. By contrast, the resistance in the high frequency semicircle does not change with the polarization voltage, confirming its originating from electrolyte.

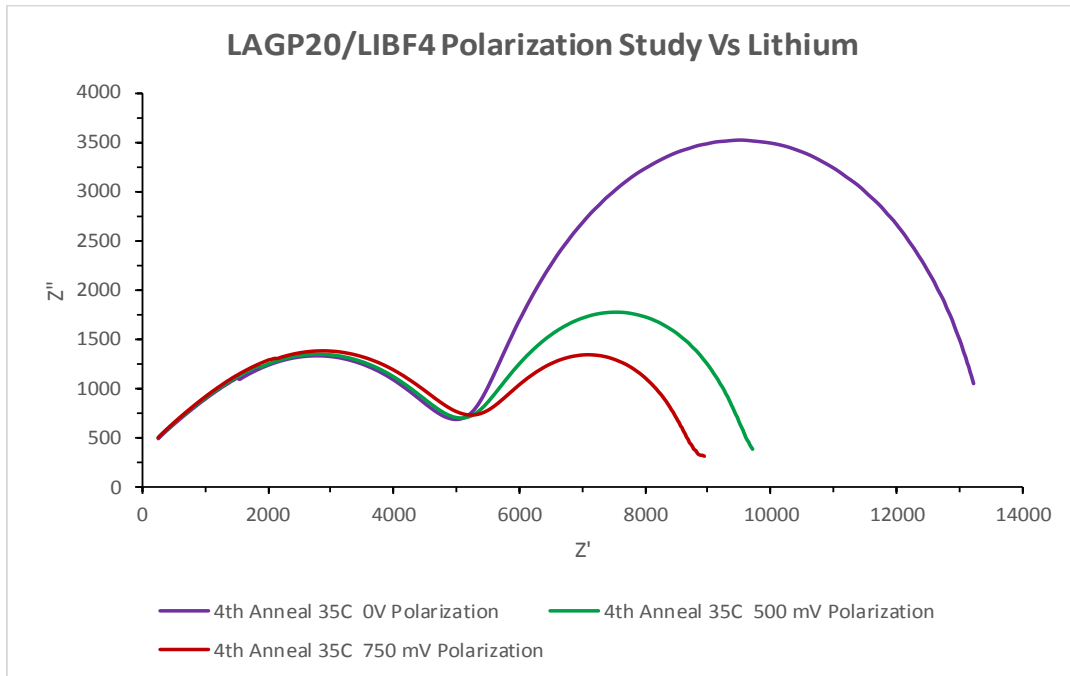


Figure 19: EIS of the LAGP20/LiBF₄ film obtained at 35°C using an AC voltage of 100 mV and DC voltages ranging from 0 to 750 mV.

The impedance spectra observed at temperatures between 55 and 80 °C are presented in **Figure 20**. It is seen that both electrolyte resistance and interface polarization resistance rapidly reduce with increasing the temperatures. The electrolyte impedance semicircle become incomplete with the fast ionic movement and hence high frequencies. The electrolyte resistances were taken from the intercept/minimum points for conductivity calculation.

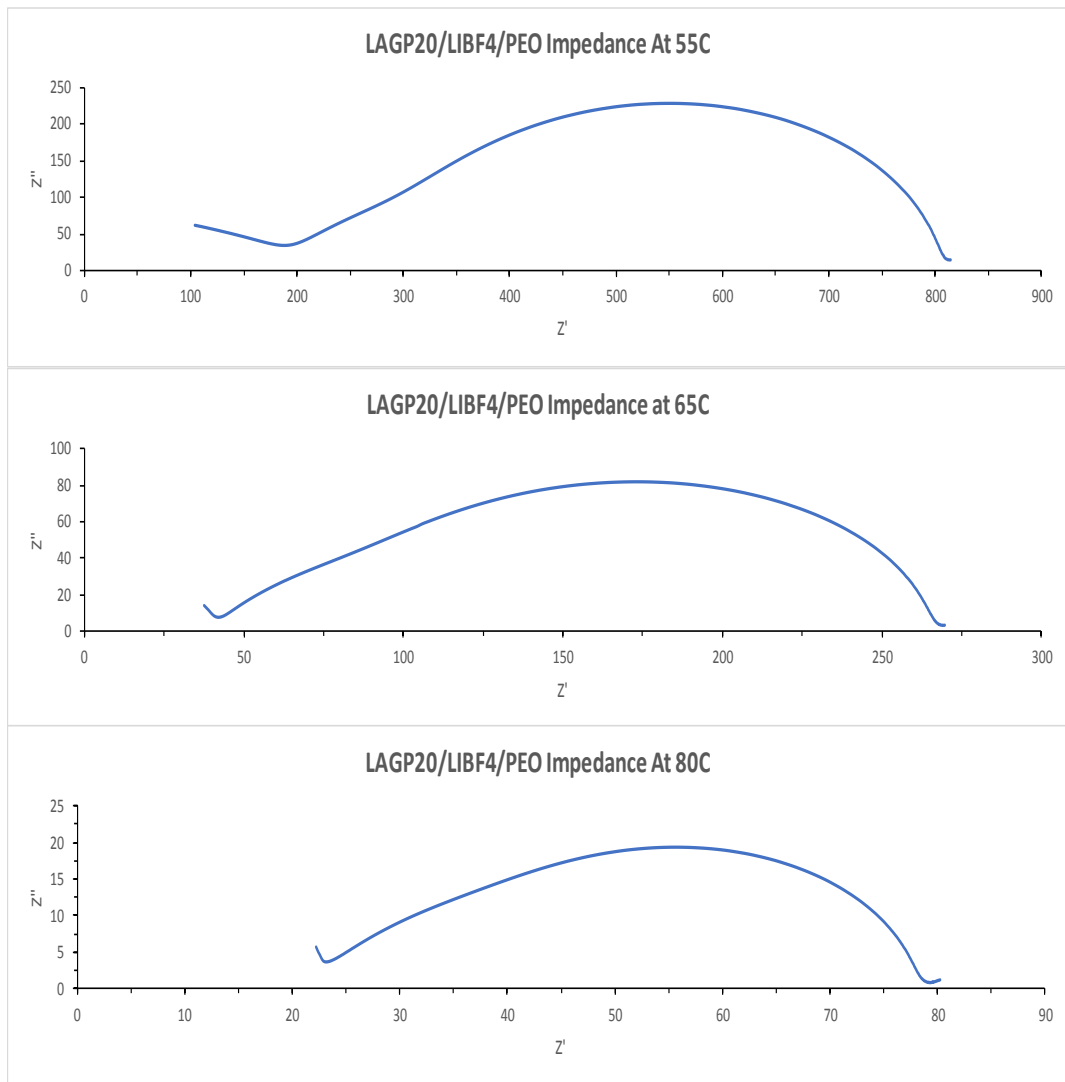


Figure 20: EIS of the LAGP20/LiBF₄ film obtained from 55° to 80° Celsius with no DC polarization

To investigate the stability of the electrolytes towards lithium electrodes and thermal treatment, the sample was cycled between 25 °C and 80 °C. **Figure 21** shows the EIS spectra recorded at 80 °C at the second, third and fourth thermal cycles. The impedance remains relatively unchanged at the high frequency intercept, confirming the stability of electrolyte against thermal cycles. Also the electrolyte passing through the melting temperature, the shape and dimension remain unchanged. The low frequency semicircle increased about 30% confirming occurrence of some reactions between the electrolyte and lithium at the interface, which may result from the instability of LAGP towards lithium.

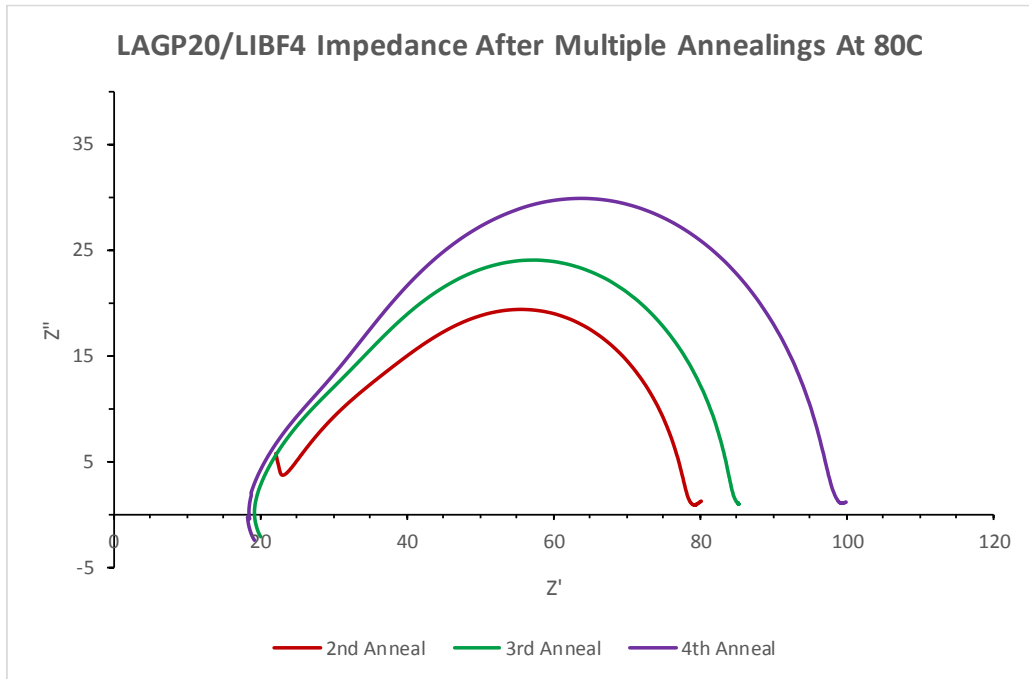


Figure 21: EIS spectra of LAGP20/LiBF₄ film at 80°C at the 2nd, 3rd, and 4th thermal cycles.

It is interesting to observe a unique phenomenon at the temperature of 45°C. At this temperature, the EIS were collected at different time, i.e. 1 hour, 2 hours, and 20

hours. A few select samples were measured at 45° Celsius months after the initial time study. It is seen that the impedance continuously increased over the extended periods of time. This phenomenon was observed in all the LiBF₄ films containing different LAGP compositions. In the later discussion, the values obtained at 45°C 20 hour was used for conductivity calculations for all the different compositions. An LAGP20/LiBF₄ film with a time study of the impedance can be seen in **Figure 22**.

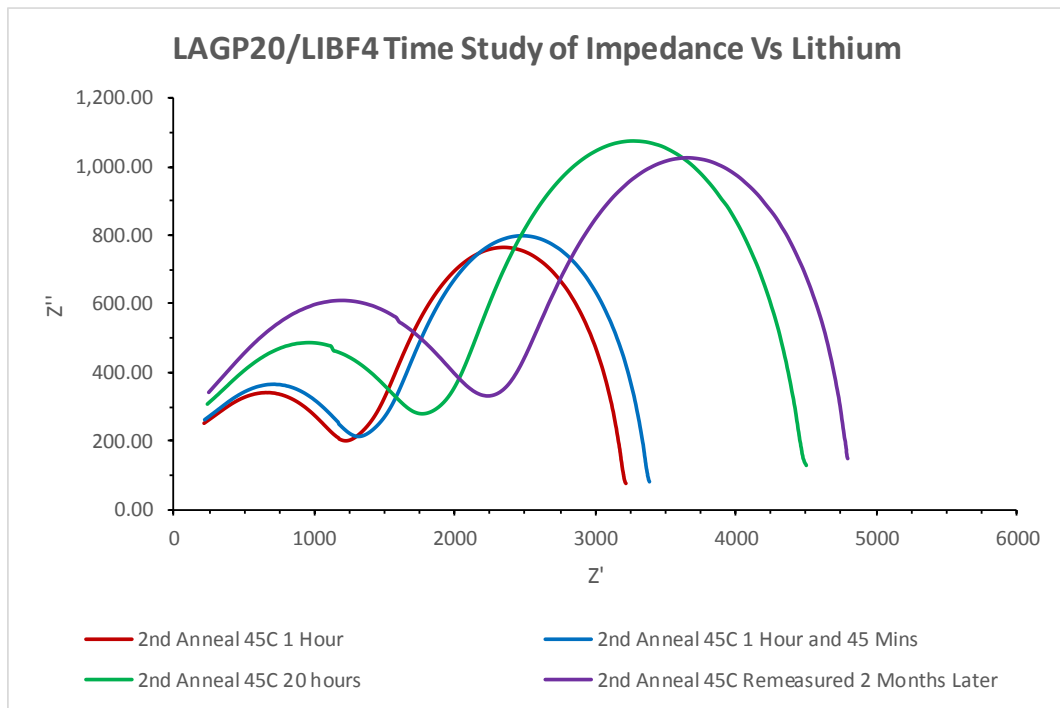


Figure 22: EIS spectra of LAGP20/LiBF₄ film at 80 °C as a function of time

Another set of experiment was performed on the sample but after different thermal cycles between 25 and 80 °C. As seen in **Figure 23**, the resistance decreases from approximately 2400 ohm down to nearly 1500 ohm and stabilizes. This observation could possibly be related with the phase transformation of PEO. At 45 °C, the PEO starts

to melt and PEO are in the transition from semi-amorphous state to viscous phase, which may take time to reach equilibrium.

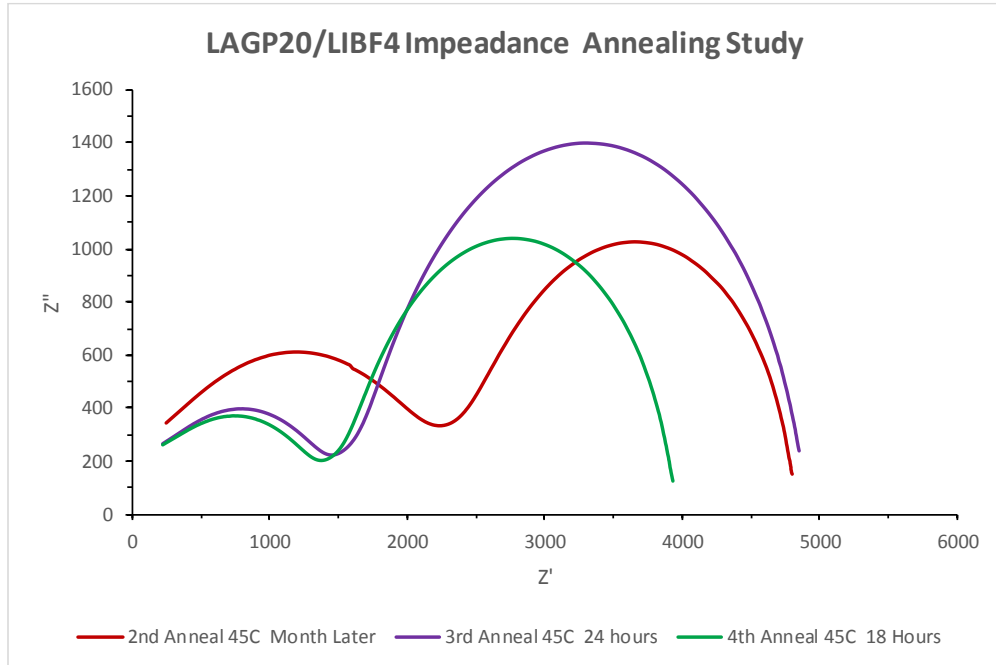
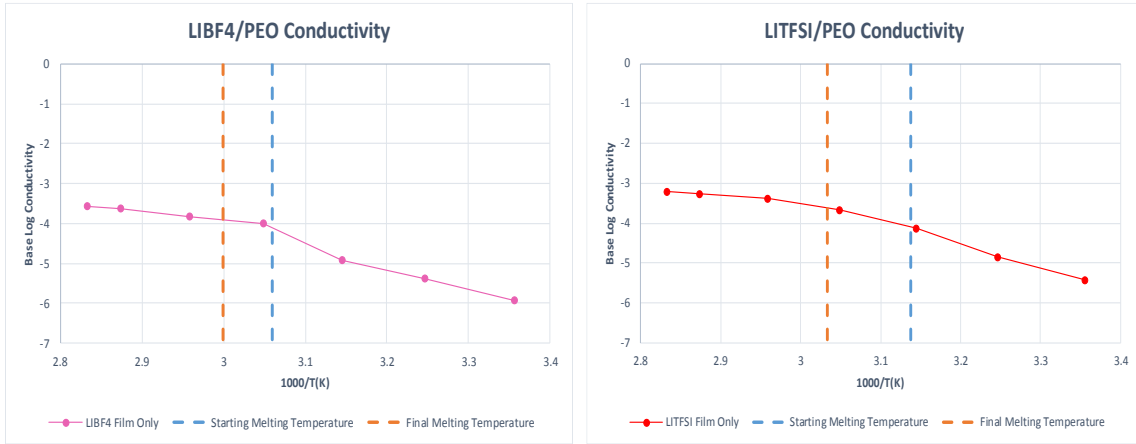


Figure 23: EIS spectra of LAGP20/LiBF₄ film at 45 °C at the 2nd, 3rd, and 4th thermal cycles.

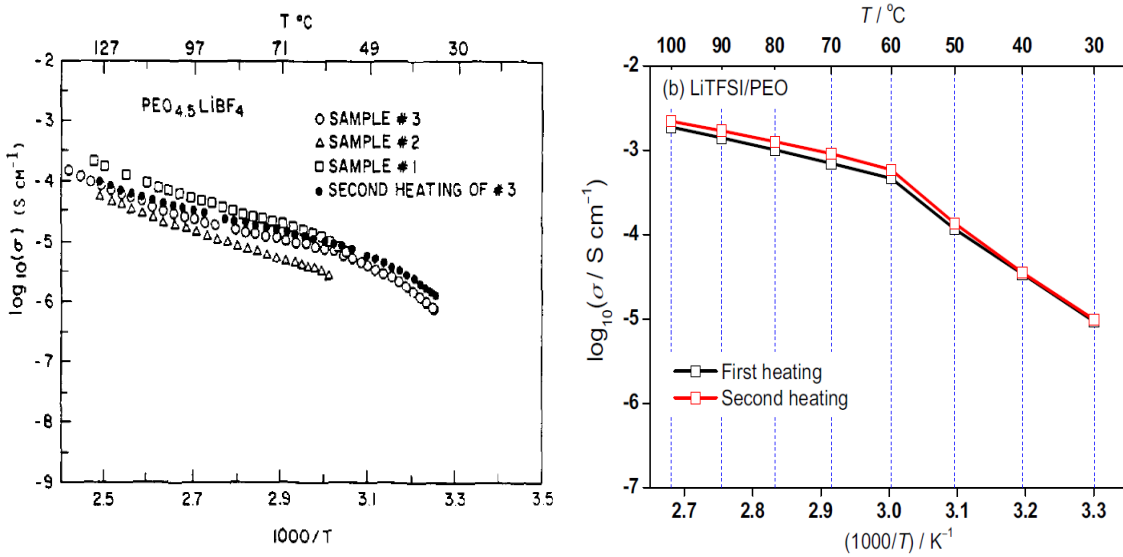
4.3 Ionic Conductivity Characteristics of the Composite Films

4.3.1 Lithiated Polymer Ionic Conductivity



(a)

(b)



(c)

(d)

Figure 24: Arrhenius Conductivity Plots of (a) PEO/LiBF₄ (8:1) film; (b) PEO/LiTFSI (20:1) film; (c) PEO/LiBF₄ (4.5:1) [109]; and (d) PEO/LiTFSI (20:1) film [108]

Figure 24 (a) and (b) present the conductivity as a function of temperature, in Arrhenius plot, obtained from PEO/LiBF₄ and PEO/LiTFSI, respectively. Apparently, the conductivity values at each temperature and the changing trend of conductivity with temperature are slightly different between the two systems. PEO/LiTFSI conductivities are consistently higher than PEO/LiBF₄. For instance, the conductivities at 25°C are 1.2×10^{-6} S/cm and 3.83×10^{-6} S/cm, and values at 80 °C are 2.66×10^{-4} S/cm and 6×10^{-4} S/cm for LiBF₄ film and LiTFSI film, respectively.

Figure 24 (c) and (d) show the public results of the two systems. When comparing with **Figure 24 (d)** in which LiTFSi/PEO also using a 20:1 EO:Li molar ratio, our conductivities is in close agreement with literature [110]. In **Figure 24 (c)**, the LiBF₄/PEO system used a 4.5: 1 molar ratio of EO:Li yielding a ionic conductivity of $1-2 \times 10^{-6}$ S/cm [107], which corroborate well with our conductivity values although the EO: Li is different from ours.

In consideration of lithium ion concentration, large anions can easily dissociate in the PEO matrix and set off free lithium cations. Hence, the bulkier the anion of the lithium salt, the higher is the ionic conductivity. The radii of BF₄⁻ and TFSI⁻ are reported 0.24, and 0.326 nm, respectively. It is reported that LiTFSI's anion has one of the lowest ionic association strengths; in stark contrast with LiBF₄ which has a higher relative ionic association strength, as demonstrated in glyme and acetonitrile [111]–[113]. The melting point of PEO/LiTFSI is lowered than that of PEO/LiBF₄, indicating a high salt dissociation level owing to the presence of a strong electron withdrawing group

(NSO_2CF_3). Higher concentration of effective mobile lithium ion contribute to the higher conductivities in LiTFSI/PEO electrolyte.

In PEO matrix, Li^+ lithium ions are mostly coordinated by the ether oxygen atoms on a segmental PEO chain due to the high donor number of EO. It is well accepted that lithium ions transport via intrachain or interchain hopping with the processes of breaking/forming lithium–oxygen (Li–O) bonds. The long-range displacement of lithium ions is the result of the gradual replacement of the ligands for the solvation of Li as well as the continuous segmental rearrangement. Therefore, in consideration of mobility, effective lithium ion transport mobility in the PEO relies on the local relaxation and segmental motion of the PEO. On the one hand, addition of a Li salt to PEO can reduce the crystallinity of PEO. An anion with a well delocalized negative charge and low basicity is preferred for improving the ion conductivity. The high flexible TFSI group in LiTFSI can act as plasticizer in PEO, which significantly reduce the crystallinity of PEO, resulting in high mobility of lithium ion and hence conductivities compared with LiBF_4 in PEO.

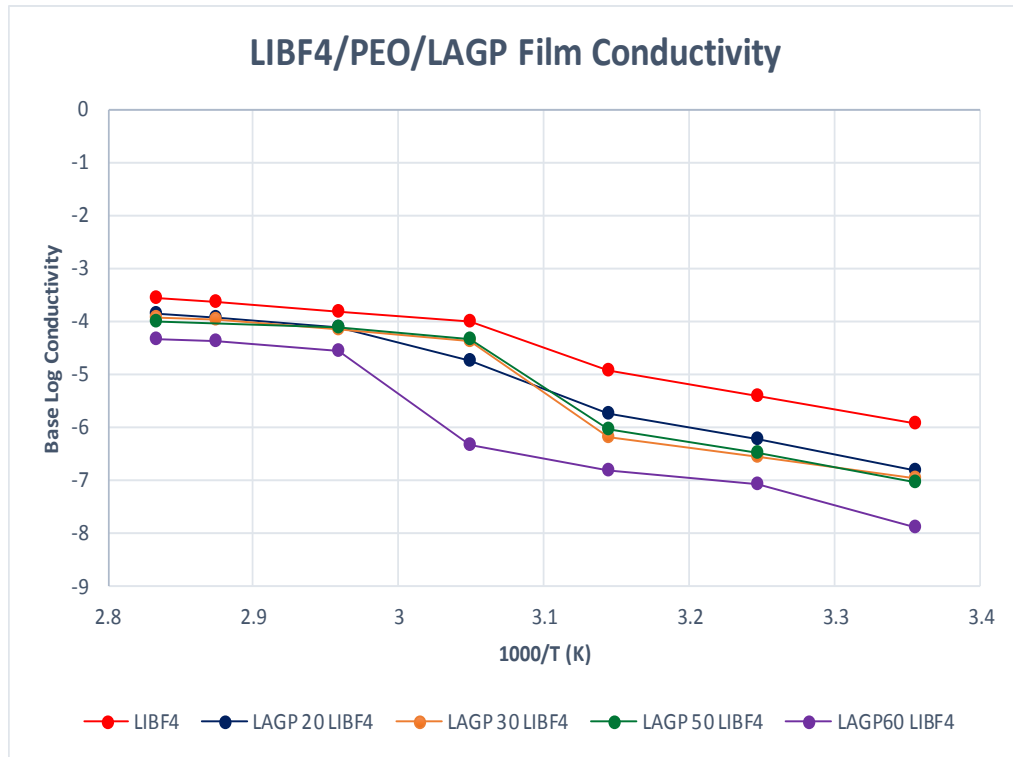
In **Figure 24 (a) and (b)** it is also seen that as the temperature increases, the activation energies are changed occurring in the vicinity of the melting temperature which are marked in the figure. The transition occurs at lower temperature in PEO/LiTFSI films. The LiTFSI films closely follows Vogel-Tamman-Fulcher (VTF) trend but the LiBF_4 film exhibits two Arrhenius behavior with a clear transition temperature. At low temperatures (below the melting point), LiBF_4/PEO has an activation energy of 91.32 kJ/mol and LiTFSI/PEO activation energy is 117.8 kJ/mol. At high temperatures

(above the melting point), the activation energies are reduced to 16.22 kJ/mol and 25.96 kJ/mol for LiBF₄/PEO and LiTFSI/PEO, respectively.

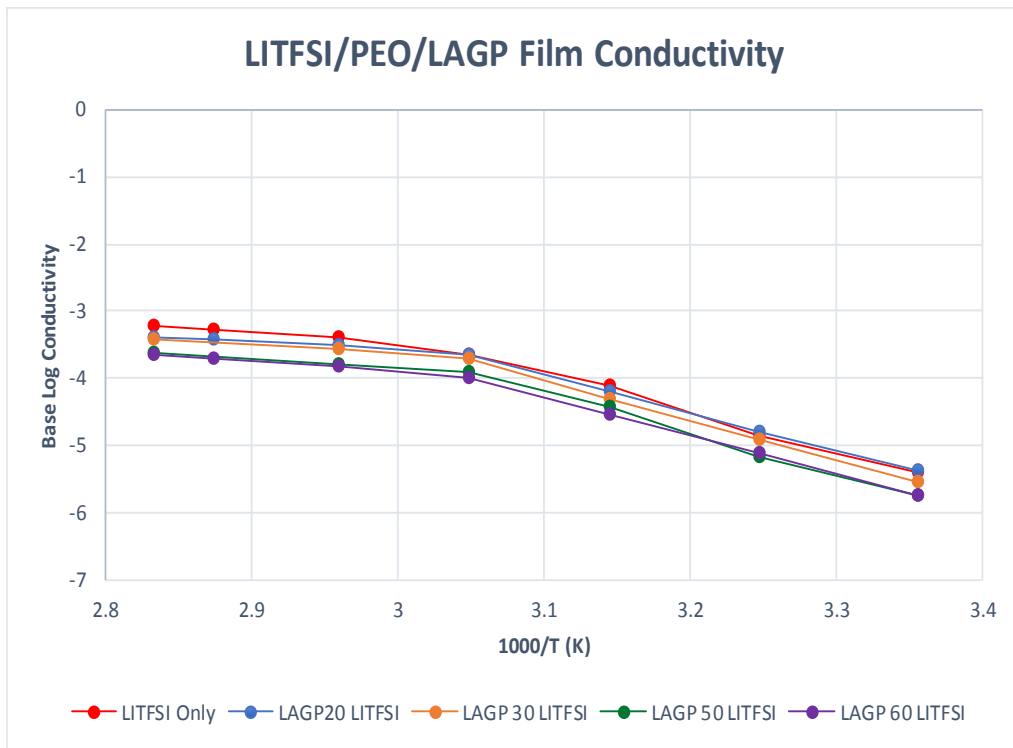
At temperatures lower than melting point, the higher degree of crystallinity of PEO leads to lower ionic conductivities and higher activation energy. The prominent lithium ion transport occurs in the amorphous phase of PEO which is dominant at temperature above melting temperature. The difference in observed behavior in LiBF₄ and LiTFSI films can be attributed to the different crystallinity degree at low temperatures and their different melting temperatures as well as crystalline to amorphous phase transformation kinetics. In LiBF₄ films high crystallinity of PEO at low temperatures corresponds to lower conductivities and higher activation energy. The narrower melting window (between starting to maximum melting point determined by DSC) in LiBF₄ film suggests rapid and close to instantaneous phase transformation. As a consequence, distinguished transition point can be detected from crystalline conduction regime to amorphous conduction regime. LiTFSI/PEO exhibits plasticized system which follows the VTF trend with no clear transition between the two regimes.

4.3.2 With Addition of LAGP

Figure 25 (a) and (b) present Arrhenius plots of LAGP/PEO/LiBF₄ and LAGP/PEO/LiTFSI composite films of different LAGP content. It is seen that with increasing proportion of weight percent ceramic the ionic conductivities of the composite films decrease for both Li-salt systems. The LiTFSI films have a marginal decrease in ionic conductivity throughout the experimental temperature range with the ceramic addition. In comparison, the ionic conductivities of LiBF₄ composite films reduced dramatically with LAGP content increasing from 20wt% to 60 wt%. At low temperature regime the reduction is 1-2 magnitudes but at high temperature regime the reduction is less than one magnitude. The activation energies are estimated in the two different temperature regime. Activation energy is 98-124kJ/mol at low temperatures and 27-35 kJ/mol at high temperatures, which is close to the electrolyte with no LAGP addition.



(a)



(b)

Figure 25: Arrhenius Conductivity Plot Summary of (a) LAGP/LiBF₄; (b) LAGP/LiTFSI PEO-based Composite Films

In general, the ceramic fillers are classified into two categories: active and inert. The active fillers refer to those intrinsic lithium ion conductors which include Li_3N , $\text{Li}_7\text{La}_3\text{Zr}_2\text{O}_{12}$, LAGP, and $\text{Li}_{1.0}\text{GeP}_2\text{S}_{12}$ (LGPS) . The inert fillers refer to those having no lithium ion conduction in bulk like Al_2O_3 , SiO_2 , MgO , TiO_2 etc. In all cases, the particle size, amount, and the characteristics of fillers are the key factors to alter the electrochemical properties of the polymer electrolytes.

It has been constantly reported the addition of a ceramic filler into the PEO-based electrolyte can improve the ionic conductivity. It is generally believed with the addition of ceramic filler, whether active or inert, the amorphous phase of PEO is increased and the recrystallization of PEO is also hindered. In terms of active fillers, there is faster lithium ion transport in the filler than in the PEO, a phenomenon which can contribute to improved conductivity. When utilizing inert fillers, those with nano-sized with appropriate surface groups and limited weight percentage can increase the conductivities. The enhancement is attributed to interactions among the surface groups of the ceramic particles, polymer segments, and the lithium salt anions in terms of percolation behavior when using nano- TiO_2 or Lewis acid –base interaction when using Al_2O_3 or SiO_2 .

Zhao et al incorporated into PEO matrix using four LAGPs with different particle sizes. The results showed that LAGP in the weight percent of 10 wt% to 25 wt% all have higher conductivities compared to PEO-only electrolyte, among which 20wt% $1\mu\text{m}$ -LAGP exhibits the maximum conductivity and 58% increase[85]. The improvement was attributed to two reasons. Firstly, LAGP suppress polymer crystallization evidenced by

the reduction of both glass transition temperature and melting temperature. Secondly, LAGP has a high conductivity ($> 10^{-4}$ S/cm) providing more mobile lithium ions and extra lithium ion transport pathways at the LAGP particle inside and surface.

The particle size of LAGP is in submicron to micrometer range. Adding 20-60 wt% low-conductive relatively large LAGP will have the following negative impacts on lithium ion transport in PEO. As mentioned before, adding ceramic filler into PEO can not only reduce the crystallinity of PEO, but it also reduces the segmental motion of polymer chains unless its passing over the melting temperature [79]. This is the possible reason for the larger conductivity decrease at the low temperatures than high temperatures. Secondly, adding ceramic filler will affect the net volume portion of PEO. In this research, 20 - 60 wt% of LAGP was added into PEO, resulting in up to 50 % of PEO volume reduction. The less conductive LAGP cannot provide any pathway through the LAGP bulk. Thirdly, although the LAGP particle size is milled down a few hundred nanometers, it appears insufficient to provide percolated pathways at the interphase between the fillers and the polymer. Previous studies suggest that the percolation enhancement usually occur with the particle size of the inert filler no more than a few tens of nanometers. LAGP has less effectiveness to enhance than Al_2O_3 and SiO_2 nanoparticles because LAGP used is submicron to micron sized, rendering less interfacial region. The LAGP60/ LiBF_4 film conductivity at low temperature regime suggests that the conductivity is dominant by the loose grain interface. Fourthly, the main polymer chain dynamics governing the ionic transport is not significantly affected when filler particles do not interact directly with polymer chains. Since LiFTSI/PEO is more facile for

lithium transport than LiBF_4/PEO , as discussed in the previous section, addition of filler has less impact in LiTFSI/PEO .

4.4 Summary

Preliminary studies of LAGP films were carried using stainless steel electrodes according to literatures. Despite using similar characterization methods, the EIS results for LAGP composite films could not be replicated. Upon further studying of characterization methods, it was determined that conductivity values calculated can fluctuate widely depending on the interface of the electrolyte and electrodes.

Lithium electrodes were chosen to use as the redox potential of PEO is greater than 4 volts and EIS studies can properly distinguish the conduction impedance of the electrolyte from the electrode interface impedance. With the help of polarization and time interface studies it was determined that the high-frequency semi-circle in the Nyquist plot represents the bulk resistance of the electrolyte.

When comparing the lithiated PEO, i.e. consisting of either LiBF_4 or LiTFSI , the conductivity values are in agreement with literatures. When LAGP is added to the lithiated polymers, the conductivities of LiBF_4 films drastically decrease. For the LiTFSI films that were blended with LAGP powder, the ionic conductivity decreases in a downward trend but substantially less than LiBF_4 composite films.

Ideally, conductivity of PEO electrolyte can be increased with compositing with highly conductive LAGP. Although the amorphous phase is increased, the large portion of the volume is occupied by ceramic filler which could not provide fast transport

pathways due to the large grain size. It is suggested that sintered LAGP and or nano conductive LAGP should be utilized in the future.

5 Mechanical Characterization of the Composite Films

Mechanical testing of electrolyte films is still relatively new territory in the Li-ion battery field. Up to date, there is no extensive report of the mechanical properties of polymer electrolytes and composite electrolyte.

In the sparse reported works, there are a variety of testing conditions and equipment used. Without agreed testing procedures or standards, the confirmation of elastic moduli, yield strength, or ultimate strength can be rather difficult, especially when there is limited data available. Further, testing details such as strain rate, geometry of the samples, as well as the environmental conditions were seldomly reported. For instance, we found that moisture has significant impact on the mechanical properties of the LiTFSI-based films. Ideally, different strain rates will have the same measured elastic moduli, but the ultimate strengths and strain to failure can invariably change [62, pp. 564–567]. Just as important to choose a set of typical strain rates, it is necessary to testing several batches of the same composition to ensure values reported are accurate and reproducible.

In this study, the mechanical properties of the series composite membranes were performed in a well-controlled environment and consistent parameters for comparison. The composite films were stored for at least two weeks in an argon filled

glove-box prior to testing. All samples were punched out and tested in a dry-room that regularly maintained a moisture level below 100ppm by weight or below 0.8% relative humidity. The dry room temperature was maintained at 21° Celsius. All samples were stretched at a rate of 0.1 mm/s or 1.05% strain/s and measured at a rate of 15 Hz.

For this study, ceramic compositions used for LiBF₄/PEO films was 20 – 60 weight percent. Two batches of LAGP30 and LAGP60 were made to ensure results were repeatable. Ceramic compositions used for LiTFSI/PEO films was 20, 30, 50, and 60 weight percent. Two batches of LAGP20 and three batches of LAGP50 were synthesized to see if the compositions were stable.

5.1 Experimental Aspects for Mechanical Testing

Films prepared for mechanical testing were punched with a ASTM D638V die, an engineering drawing can be seen in **Figure 26**. A sample image of a pristinely punched D638V LAGP50/LiTFSI tensile sample is shown in **Figure 27 (a)**. Samples were punched in a way that the gage length was a constant thickness, but due to the orientation of the casting dishes, the samples get sequentially thinner with each new sample. An image of a punched film with thickness indicator bars can be seen in **Figure 27 (b)**.

The thickness of the punched films was measured using a Mitutoyo 293-185 micrometer (see **Figure 28**). The micrometer has a calibrated accuracy of 1 micron and a flatness of 300 nanometers. Samples used in testing had an average thickness of 58-75 microns depending on the area punched and the composition. Any samples with a

deviation of more than 5 microns across the length of the gage length was not used in experiments.

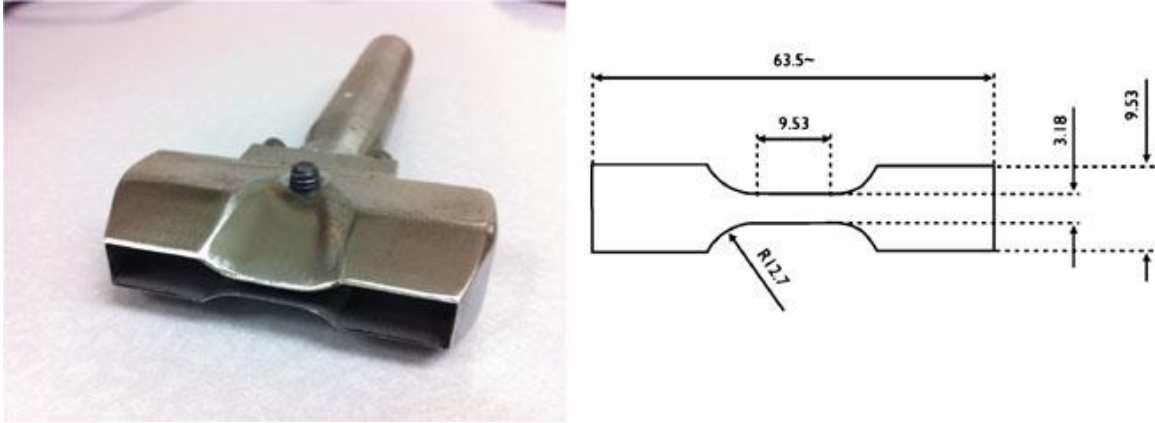


Figure 26: An Engineering Drawing and Specs of ASTM Standard Used

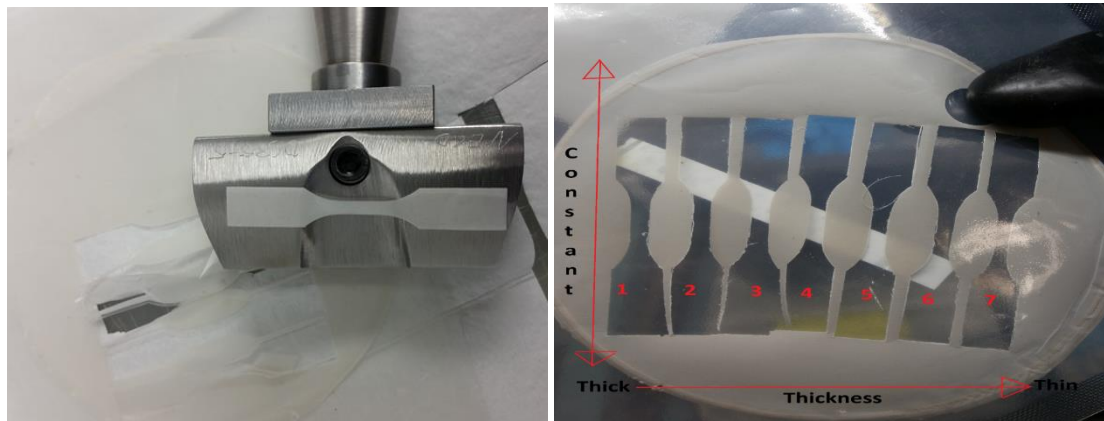


Figure 27: LAGP50/LiTFSI Composite Tensile Sample Punched From a D638V Die

The tensiometer used to stretch the polymer films was a custom translation stage purchased from Bruker. A NIST calibrated 2.5 pound MDB load cell purchased from Transducer Techniques. The equipment and software used to collect data was an NI PXI-1052, NI PXI-8360, NI SC-2345, NI- SCC-SG24, M Series PXI-6251 DAQ card, and LabVIEW. An image of the LabVIEW GUI used and a composite film under stretching in

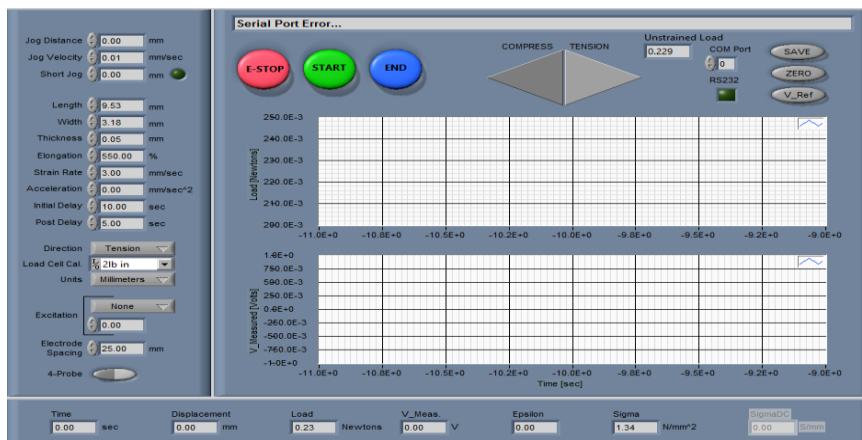
the tensiometer can be seen in **Figures 29 (a)** and **Figure (b)**. It need to mention the system has the maximum strain range of 550%.



Figure 28: Mitutoyo 293-185 micrometer



(a)



(b)

Figure 29: (a) the extensometer used to stretching LAGP/PEO/Li-salt Composite Film; (b) The LabVIEW GUI Used to Control The Tensiometer and Record Data

5.2 Stress-Strain Behavior of Pure PEO films

As a reference data, mechanical tests was carried out on unlithiated PEO films. A stress vs strain plot of the solution cast PEO films can be seen in **Figure 30**. The average elastic moduli was calculated 332.5 MPa from the three samples used. For instance, spin cast and compressed PEO pellet of unknown molecular weight) had elastic moduli values between 290-300 MPa using atomic force microscopy(AFM) [114], [115]. Because the authors did not provide the information of the molecular weight, it is difficult to say if the mechanical properties can be accurately compared to our results. It is well known that mechanical properties of polymers are affected by molecular weight[62, pp. 557–607], [116]–[118]. Lee, using the fluorescent decay of a photo-isomerizing dye [102], determined the elastic moduli of 323 MPa for the spin cast PEO films with 600,000 molecular weight. The moduli values reported by Lee is close to the values that we calculated. The ultimate strength of PEO was determined 13.7 MPa. All PEO has a strain over 550% at the experimental condition.

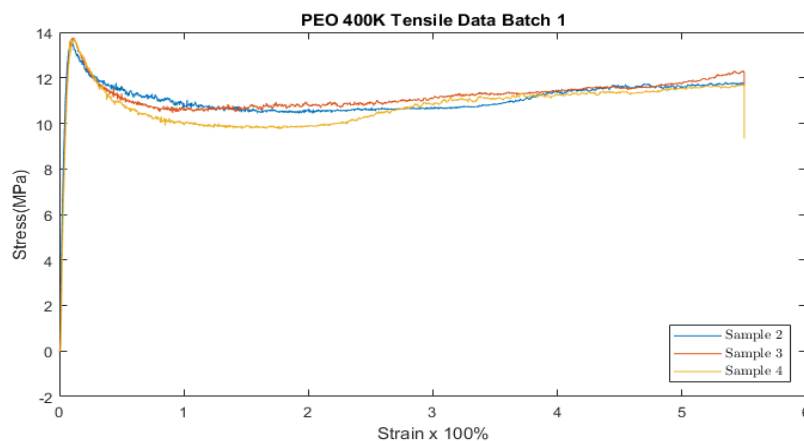
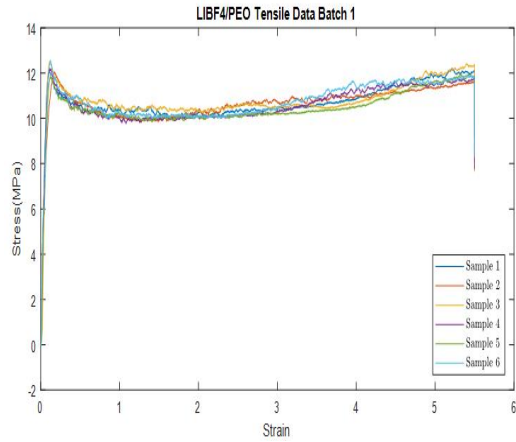


Figure 30: Stress vs Strain Plot of 400,000 Molecular Weight PEO

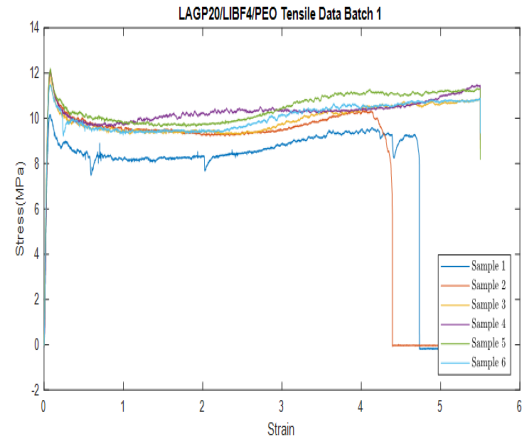
5.3 Mechanical Characteristics of LAGP/PEO/LiBF₄ Composite Films

The stress-strain plots obtained from PEO/LiBF₄ with and without LAGP, i.e. LAGP0, LAGP20, LAGP30, LAGP40, LAGP50, and LAGP60, composite films can be seen in **Figure 31 (a-f)**. Please note at least six specimens from the same batch were tested at each composition.

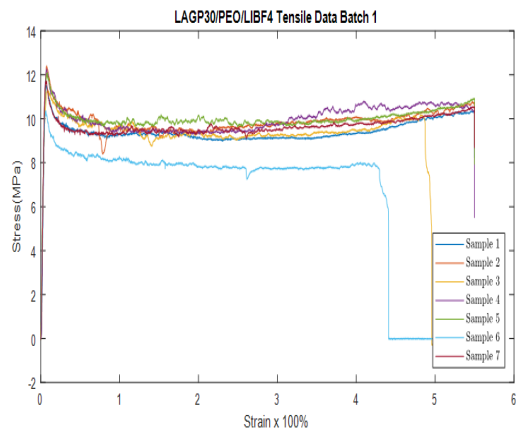
Seen from **Figure 31**, the ultimate strength is reduced from 13.7MPa to 12.2 MPa with the addition of LiBF₄ into PEO. With increasing proportions of LAGP, the ultimate strength of the composite films remains relatively unchanged up to LAGP 50 wt%. For LAGP50 and LAGP60 films, the ultimate strength slightly of many specimens reduced with the minimum value of 10MPa. The strain to failure drastically decreases. For LAGP20 and LAGP30, the failure strain is 450% or higher. For LAGP40, the failure strain is reduced to the range of 241-462%. When the LAGP content is raised to 50wt% and 60wt%, the failure strain decreased dramatically to 26-73% and 14-27%. All values obtained from different samples with same or different batch were analyzed quantitatively in detail, which will be discussed in the following.



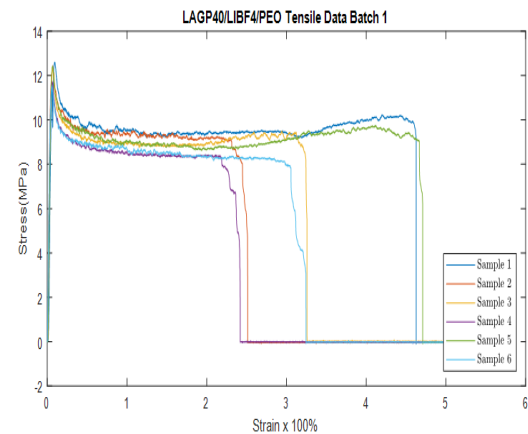
(a)



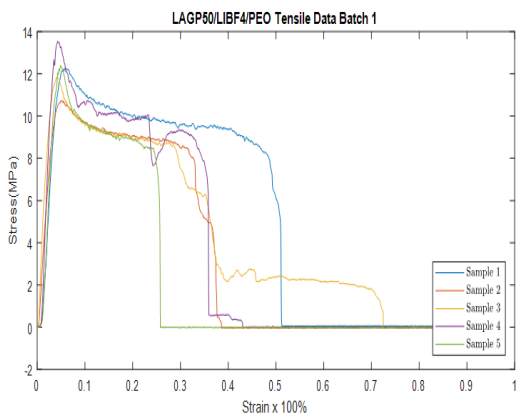
(b)



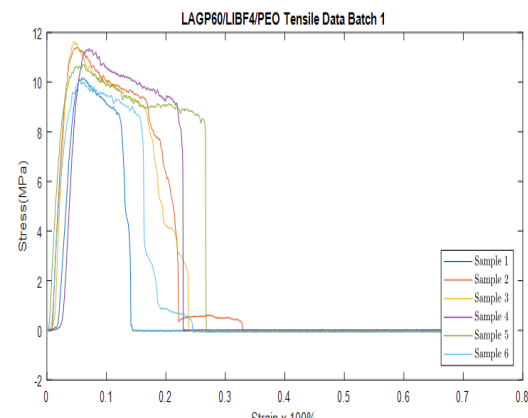
(c)



(d)



(e)



(f)

Figure 31: The stress-strain plots obtained from PEO/LiBF₄ series with LAGP weight percent from 0% to 60%. (a) LAGP0, (b) LAGP20, (c) LAGP30, (d) LAGP40, (e) LAGP50, and (f) LAGP60.

Figure 32(a) presents the change in the average elastic moduli as a function of weight percent content of LAGP. The addition of LiBF_4 salt initially causes a drop in both the elastic moduli and ultimate strength of PEO. The elastic modulus changes from 332.5 MPa to 230.6 MPa. The benefit of adding LAGP filler is seen that the elastic modulus continuously increased with the amount of LAGP weight percent, which is close to a linear relationship. For LAGP60/ LiBF_4 films, the average elastic moduli is 472.7 MPa, which is over 200% of the electrolyte film with no ceramic filler.

Figure 32(b) present the change in the average ultimate strength as a function of weight percent content of LAGP. Apparently, the average ultimate strength of PEO remains relatively unchanged, within the instrumental error, at the value of 12 MPa with LAGP addition up to 50wt%. At LAGP 60wt% the average ultimate strength is reduced to 11.3MPa. Further adding of LAGP beyond 60 wt% should be done with caution, which may lead to continuously/dramatic reduce in terms of the ultimate strength.

With the increased addition of LAGP to LiBF_4 films, the probability for failure under elongation increases and the amount of strain to failure decreases. **Figure 32(c)** present the change in the failure strain as a function of weight percent content of LAGP, in which the reference line at on the y-axis of the plot represents the strain limits of the instrument. Within the instrumental limit of 550% elongation, failure begins to observe with LAGP30 films, but only 3 out of 13 samples fails. However, as the LAGP composition reaches 40 weight percent or higher, all samples break. For LAGP40 samples the average elongation to break was over 300 percent. Samples that were composed of more than

40 percent LAGP had a large decrease in the amount of strain that it could endure before breaking. LAGP50 and LAGP60 samples all broke in less than an average of 70 percent strain. LAGP60 samples broke after only being elongated as little as 30 percent. Experimentally, in this study were unsuccessfully at achieving free standing composite films with LAGP over 70wt% in the PEO/LiBF₄ series.

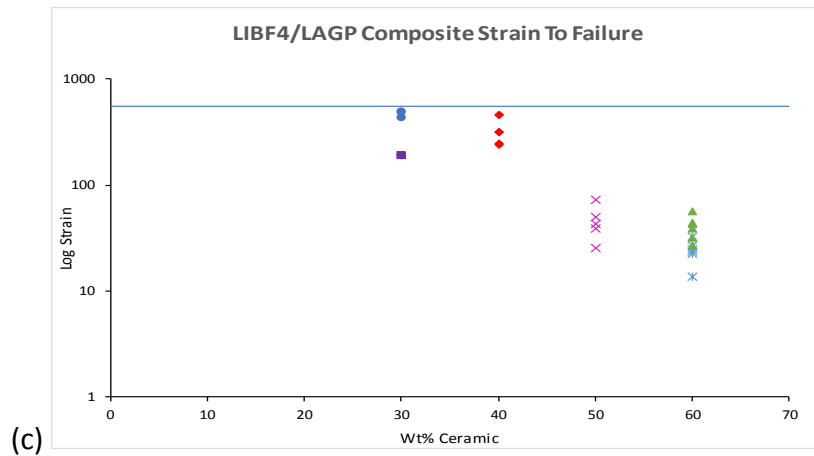
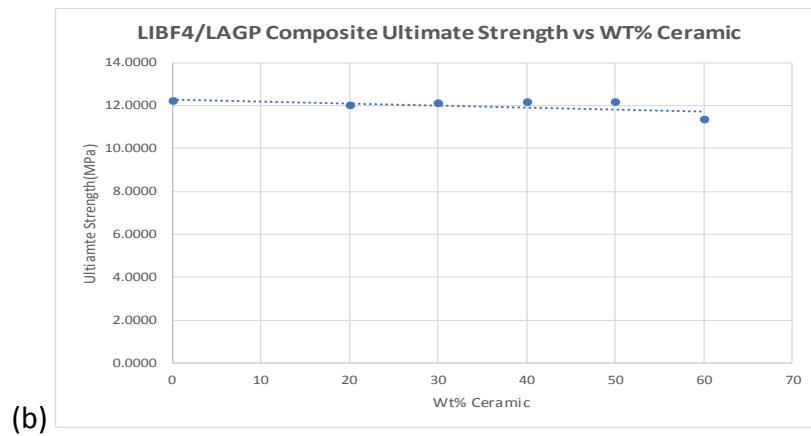
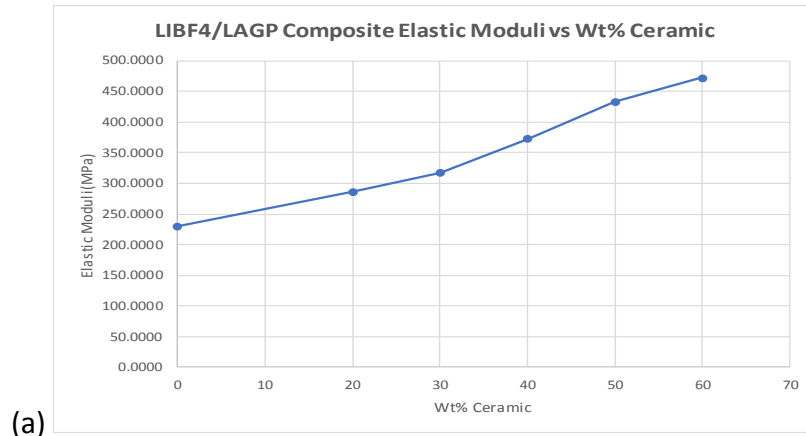


Figure 32: Mechanical properties of the composite films as a function of LAGP weight percent in the LiBF_4 series. (a) average Elastic modulus; (b) average ultimate strength; (c) statistic failure strain (the straight line is the instrumental limit)

5.4 Mechanical Characteristics of LAGP/PEO/LiTFSI Composite Films

For the LiTFSI series, the stress-strain plots of LAGP0, LAGP20, LAGP50, and LAGP60 composite films can be seen in **Figure 33 (a-d)**. Addition of LiTFSI into PEO has reduced the ultimate strength from 13.7MPa to less than 2MPa and the elastic moduli decreased from 332.5 MPa to 23.2 MPa, consistently confirming the plasticizer effect of LiTFSI.

Again, with any addition of LAGP, the elastic moduli increases. The average elastic moduli for LAGP0, LAGP20, LAGP50 and LAGP60 films are 23.2MPa, 71.4MPa, 101.6MPa, and 103.4MPa, respectively. The elastic modulus increases rapidly with the addition of filler, over 400% improvement when the LAGP is 50-60wt%.

All the composite films with LAGP also have lower ultimate strength than pure PEO but close or slightly higher than PEO/LiTFSI film. It is also noticed that ultimate strength values of the composite films fluctuate in the range of 1.5 - 4.5MPa. The average ultimate strengths for LAGP0, LAGP20, LAGP50 and LAGP60 films are 1.98MPa, 3.43MPa, 3.07MPa, and 2.30MPa. It appears than more LAGP will reduce the ultimate strength.

The failure strain gradually decreases upon the addition of LAGP. The strain to failure drastically decreases, similar to LiBF₄ series. For LAGP20 and LAGP30, the failure strain is 350% or higher. When the LAGP content is raised to 50wt% and 60wt%, the failure strain decreased to 50-120% and 14-25%, respectively.

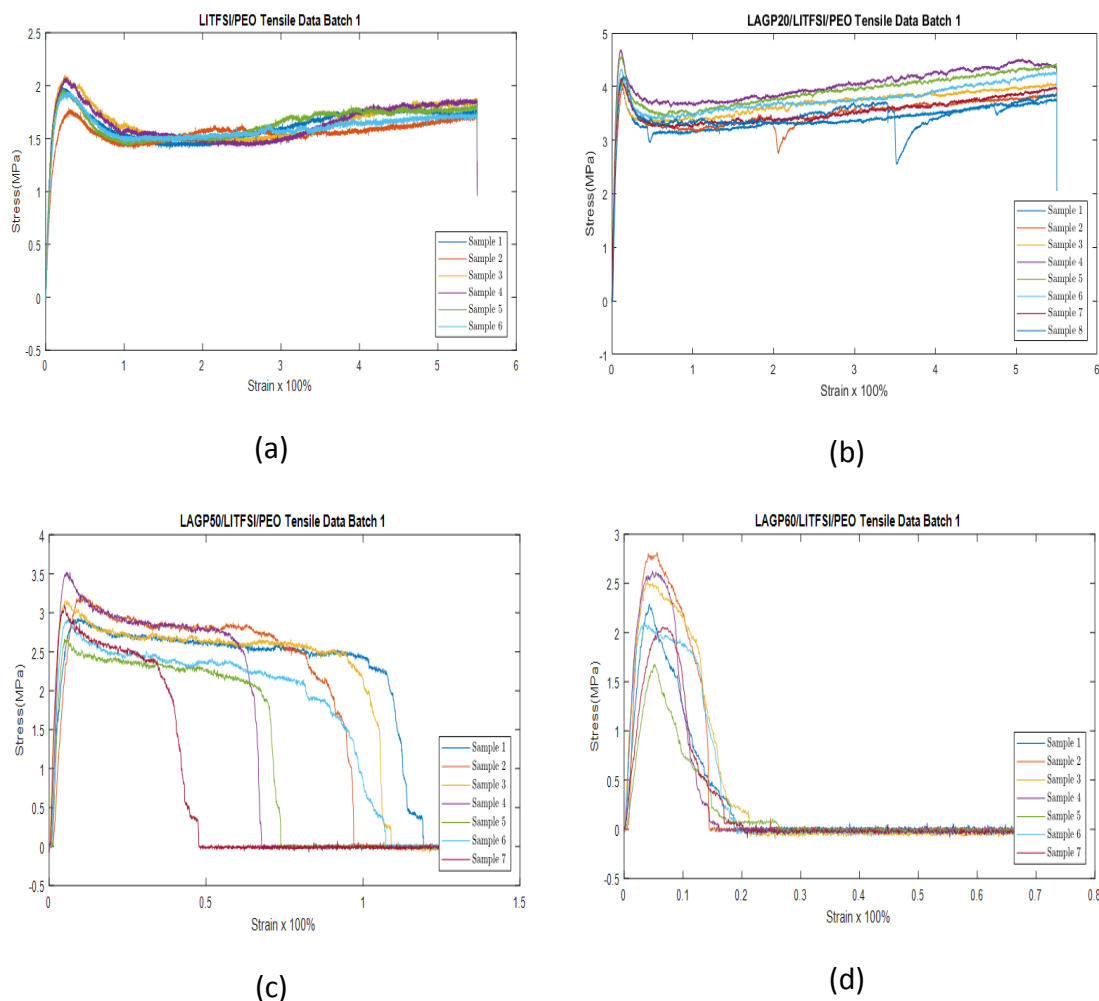


Figure 33: The stress-strain plots obtained from PEO/LITFSI series with LAGP weight percent from 0% to 60%. (a) LAGP0, (b) LAGP20, (c) LAGP50, and (d) LAGP60.

5.5 Morphological Evolution of the Composite Films Upon Stretching

Figure 34 present a series images showing the morphological evolution from top view. For the LAGP less than 40wt%, the composite films exhibit deformation similar to the polymer matrix. Stretching of polymer along the tensile direction can be visualized. Further increasing the elongation, micropores form both on the surface and inside of the films. The pore size and density gradually increased forming crazing structure, i.e.

interconnected array of micropores bridged by the polymer fibers. The bridges will further elongate under the stress until break resulting large cracks until the fracture.

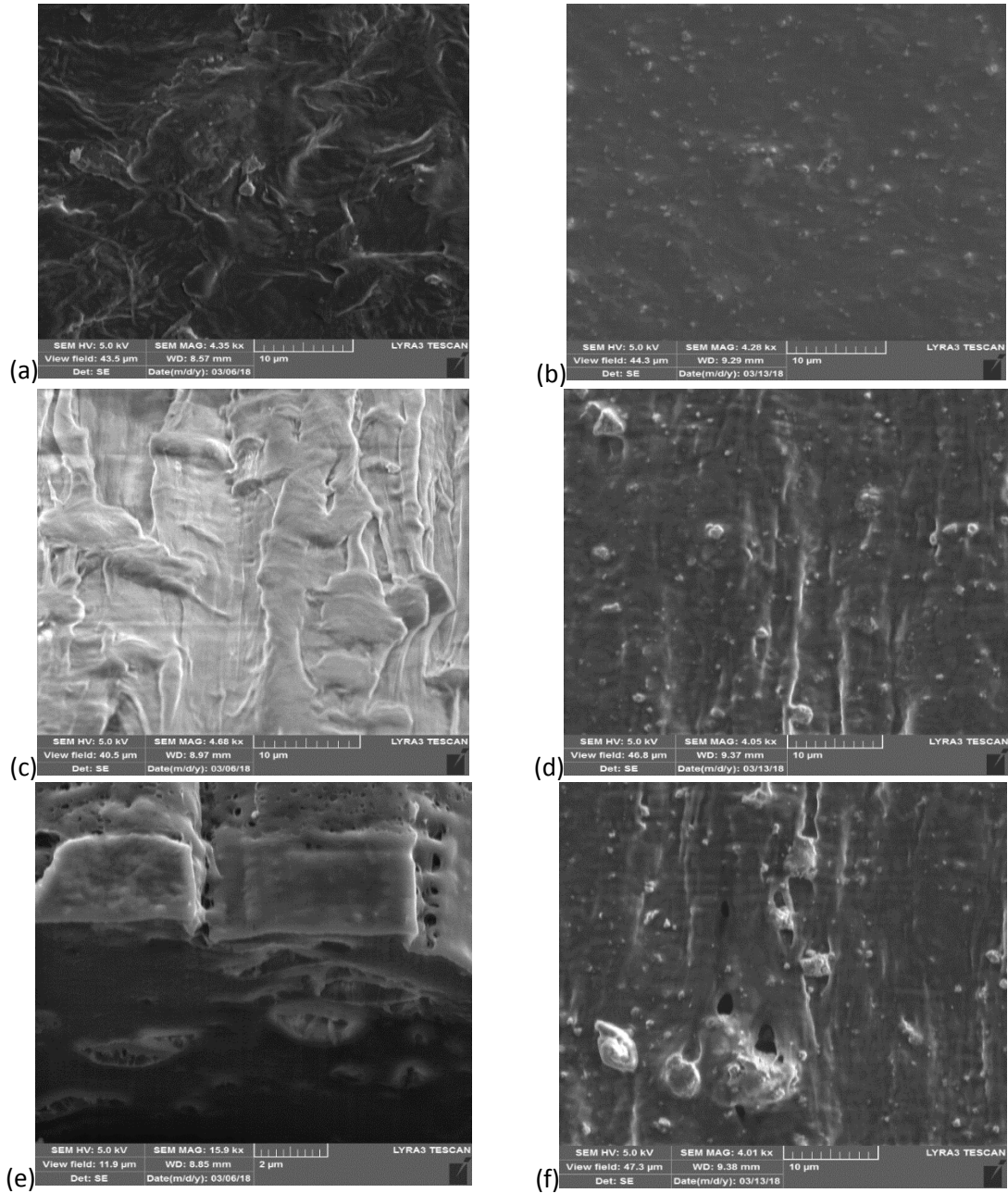


Figure 34: SEM images of PEO (left) and LAGP30/PEO/LiBF4. (a) PEO unstretched; (b) LAGP30 unstretched; (c) PEO stretched, top view; (d) LAGP30 stretched, top view; (e) PEO stretched, side view after FIB cutting; (f) LAGO 30 stretched, top view with micropore

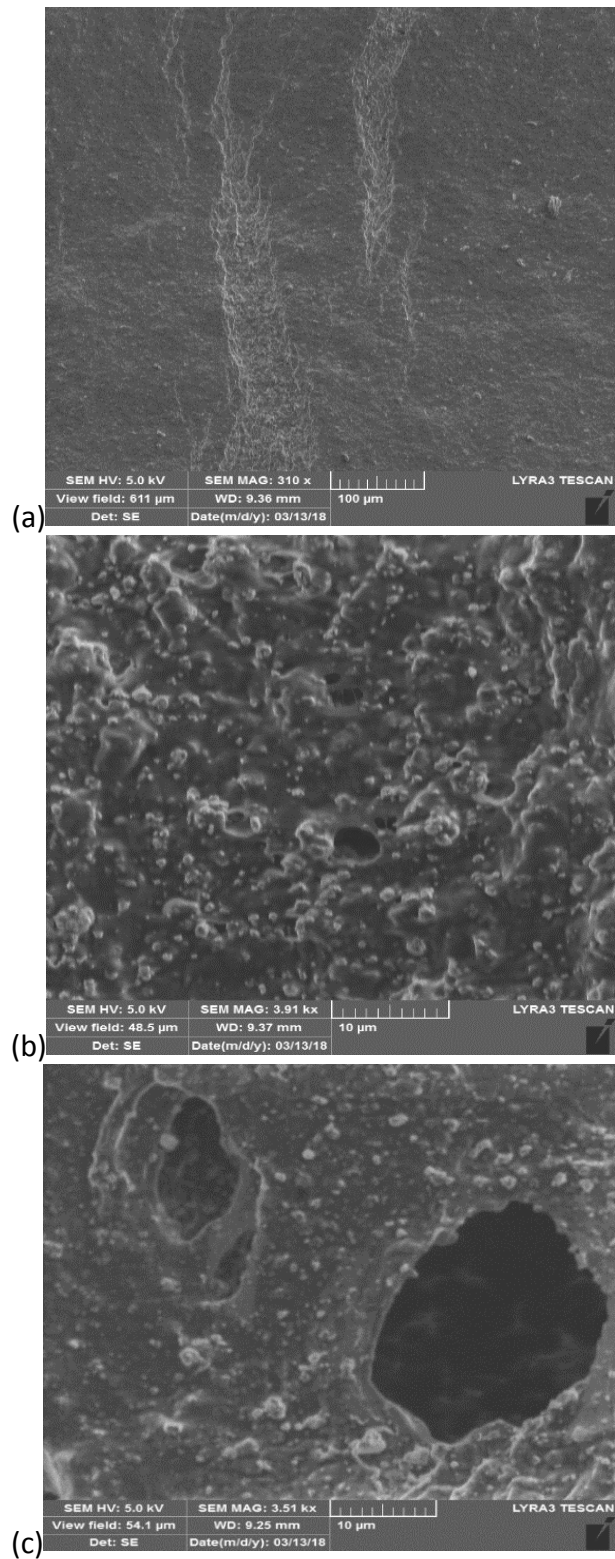
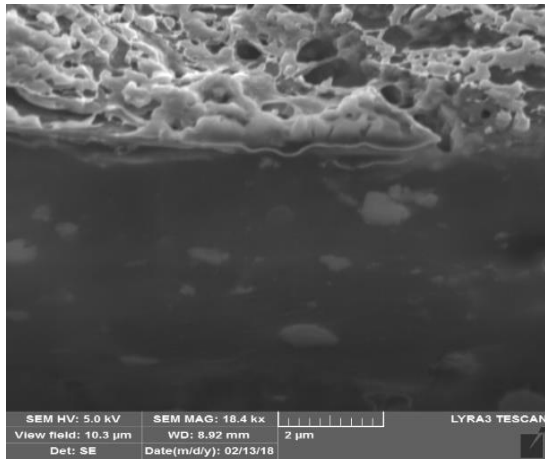


Figure 35: Top-view SEM images of stretched LAGPO/PEO/LiBF4. (a) silver streak at the necking area; (b) micropore at the necking area; (c) increased micropore in the center area.

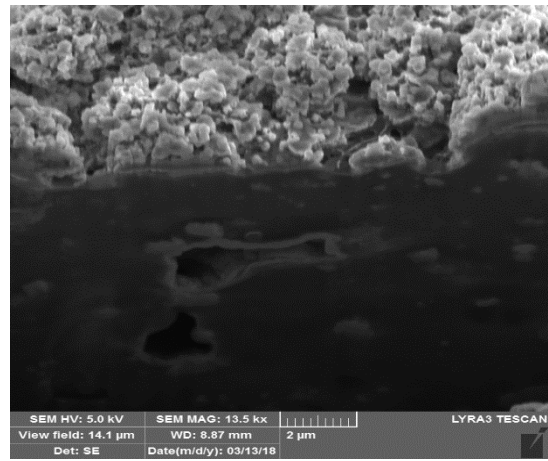
When the LAGP composition increased to 50wt%, no clear polymer stretching and crazing features were observed. Instead, the “silver streaks’ initially appear (see **Figure 35 (a)**), within which many micropores (see **Figure 35 (b)**) form instantly. Increasing the elongation results in rapid pore growth, crack propagation (**Figure 35 (c)**) and eventual fracture, exhibiting more brittle behavior.

It is also noticed that in the similar necking region after stretching test, the amount of microvoids and the size were very different. In LAGP 20 -40, there are smaller and less amounts of microvoids. Cracks may occur along the interface between ceramic and polymer matrix as well as at the polymer phase. In LAGP 50-60 almost all cracks occurs at the interface, and debonding of ceramic phase from polymer matrix were obvious.

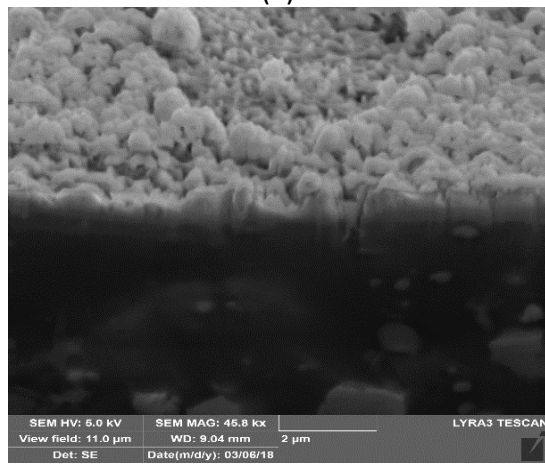
Using the feature of the FIB, cross-section morphology within selected composite films were investigated. **Figure 36 (a-f)** show the SEM images of uncoated LiBF₄ composite films before and after tensile test. For the stretched samples, most cutting and imaging was taken in the vicinity of gage center area. It can be seen from the progression of images, that as the LAGP addition increases, the volume of the polymer matrix decrease. For LAGP60, there exist intrinsic internal micropores and large agglomerations. After stretching, the portion (number and size) of micropores increased significantly with increasing LAGP content. Most pores are formed in the vicinity of ceramic/polymer interface.



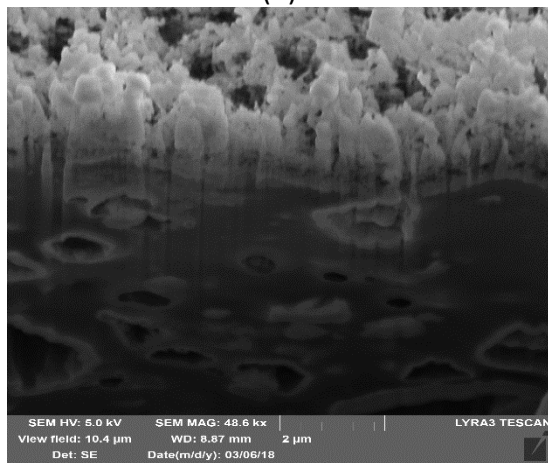
(a)



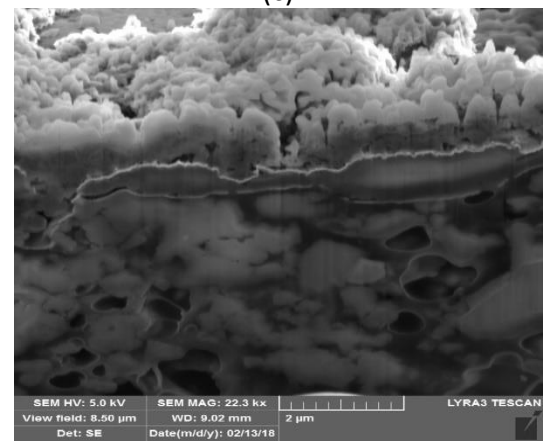
(b)



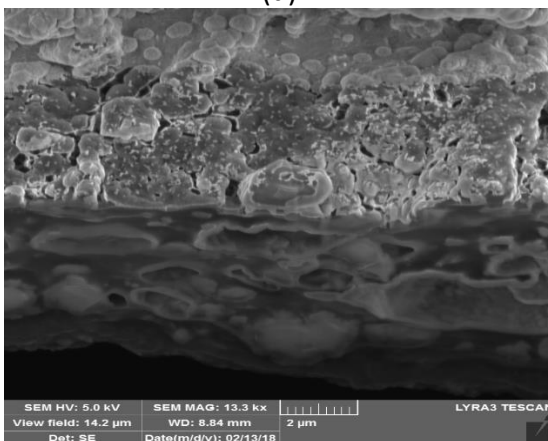
(c)



(d)



(e)



(f)

Figure 36: Cross-section SEM images of LiBF₄ series before (left) and after (right) tensile test (a, b) LAGP20; (c, d) LAGP 30; (e, f) LAGP 60 tensile test

5.6 Accuracy of Equipment Used in Mechanical Testing

The load cell used was a full bridge strain gauge calibrated for tension. To increase the sensitivity of the signal generated, the SCC-SG24 was used to amplify the signal 100 times its normal output, changing the max output voltage of the load cell from 20 mV to 2 volts; the nominal gain error is 1% of the measured output. The DAQ card utilizes a 16 bit ADC and a 1.92 mV reference was utilized when actively collecting data on a -10/10 volt scale. Depending on how much load is applied to the load cell the accuracy of the output will vary. In principle at 2.5 lbs. the measured signal should generate an output voltage of 2 volts where if the load applied is only 1.25 lbs. the measured signal will generate 1 volt. Using a 16 bit DAQ with a full range 10 volt scale reduces the number of bits to 15 or 32768 data points of resolution; what this translates to is 3.05 mV of resolution or that data can only be resolved in these intervals. Between the two different lithium salt film series the lowest average strength of each sample was 0.4 Newtons and 2.7 Newtons. Approximately 0.8 Volts of excitation are produced for every 4.445 Newtons of applied load. The detected voltage for samples with a load of 0.4 Newtons produces 0.072 Volts and the sample with 2.7 Newtons of load produces 0.486 Volts of excitation. Resolving the average resolution error of each film series yields:

$$\text{Resolution Error of LITFSI} = \frac{0.00305}{0.072} \times 100 = 4.236\% \text{ RO}$$

$$\text{Resolution Error of LIBF4} = \frac{0.00305}{0.486} \times 100 = 0.6275\% \text{ RO}$$

It should be noted that the accuracy of the voltage readings is much higher than the resolution of the instruments, therefore it can be resolved that the uncertainty of the measurements will only come from the resolution, gain error of the amplifiers, and the uncertainties corresponding to the load cell. Uncertainties that would rise from the load cell are non-linearity, hysteresis, non-repeatability, and the effects of temperature drift, all of which would arise from operating in values that did not match calibration conditions. The uncertainty of non-linearity, hysteresis, and non-repeatability of the load cell is 0.05% of the readout(RO). Drift in measurement due to temperature is 5ppm of the RO per ° Fahrenheit; a offset error of 7.2° Fahrenheit was used. The overall uncertainty can be determined using the following equation where the units are non-dimensionalized into percentages [119]:

$$U_c = \sqrt{U_{Measurement}^2 + U_{Gain}^2 + (U_{Nonlinearity}^2 + U_{Hysteresis}^2 + U_{Nonrepeatability}^2 + U_{Temp}(T(^{\circ}F)))^2}$$

$$U_c = \sqrt{U_{Measurement}^2 + 1^2 + 3(.05^2) + (.005 * T(^{\circ}F))^2}$$

Using the aforementioned formula, it can be approximated that the uncertainty of the LiTFSI composite films and LiBF₄ composite films is 4.35% and 1.18% respectively. In conclusion, it can be said that while that the accuracy of the measurements maybe significantly higher, it can only be said with confidence that the samples are 95.65% and 98.82% accurate respectively. If a measurement setup with a higher degree of certainty is used, the results may differ significantly when reproducing the experiment.

5.7 Processing Factors Affecting the Mechanical Properties

As discussed in the previous section, the uncertainty of the LiTFSI composite films and LiBF₄ composite films is 4.35% and 1.18%. It is, therefore, believed that any variation great than 5% results from the difference in specimens originated from the film morphological defects and the distribution of the ceramic filler. In order to identify these factors, a series SEM images are analyzed from both top view and side-view.

5.7.1 Surface Morphology

In this study, all the films were casted in a Teflon dish machined in-house. The roughness of the Teflon dish base will unavoidable transfer the bottom face, (side that it was cast on) of any casted films. As seen in **Figure 37**, a representative SEM image showing the grove pattern of the Teflon dish base introduced anisotropic surface morphology on the composite electrolyte film. At the moment without additional experiments, it is difficult to quantitatively predict how much influence these grove ring morphology has on the mechanical properties of the films.

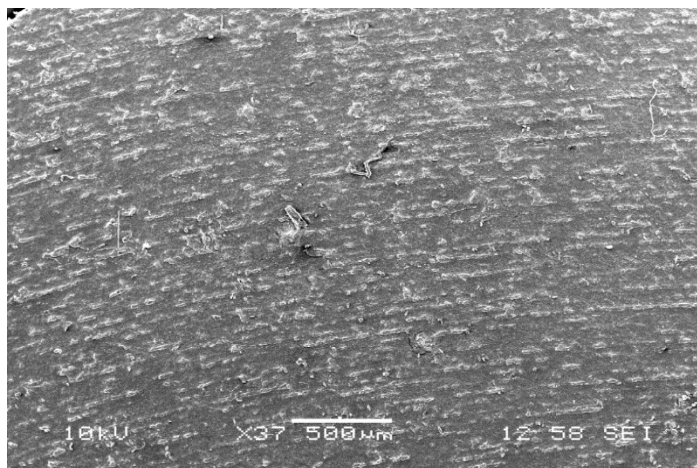


Figure 37: SEM image of the back side of a LAGP20/PEOLiBF₄ Film

As the films were processed in the quiescent environment, spherulite structure will form. **Figure 38 (a-c)** present the SEM images showing the existence of spherulite in the LiBF_4 film with and without LAGP. The average spherulite size is approximately 10-20 microns. It is generally accepted that spherulite size can play an important role on the mechanical strength of the films. The smaller the spherulites, the larger the elastic moduli and yield strength is [120]. Under further observation, it can be seen that the cracks begin at where these spherulites connect upon elongation.

5.7.2 Differences Between Front and Back of Films

In this study, the films were casted in Teflon dish. Hence solvent can only escape from the top surface. This processing can result the different morphology between the top and the bottom. On the other hand, it is occasionally observed that there are less ceramic particles on the top surface than those on the bottom side, especially there are many LAGP large agglomerate in the composite films. The large ceramic agglomerates usually descended faster than the solvent evaporation rate according to the established Stoke's Equation. The phenomenon is more prominent at the early stage of solvent evaporation when the solution is less viscous. When the precipitation occurs, the top surface would be much different from the bottom surface, in correlation with the distribution of the ceramic agglomerates. More agglomerates would concentrated on the bottom side with non-uniform distribution. **Figure 39 (a-f)** present some representative imaging showing the difference. Top side is relatively smooth while the bottom side constantly contains some micropores formed either during the film formation or the peeling process, independent of the presence of LAGP.

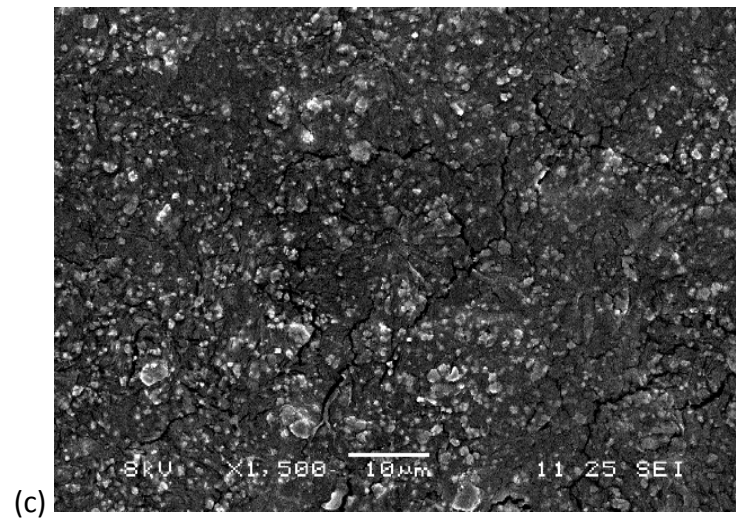
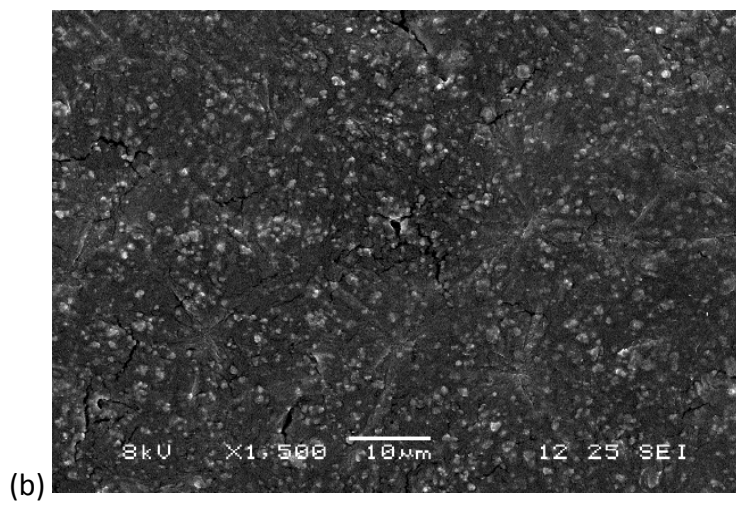
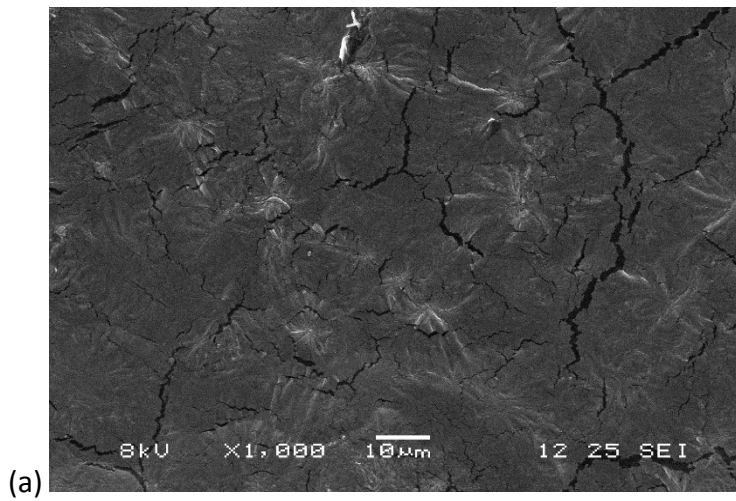
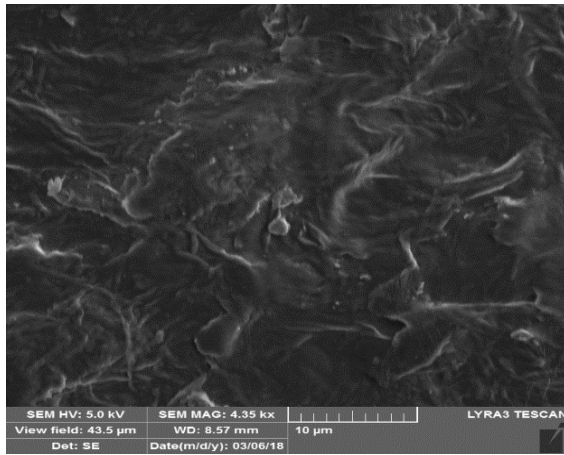
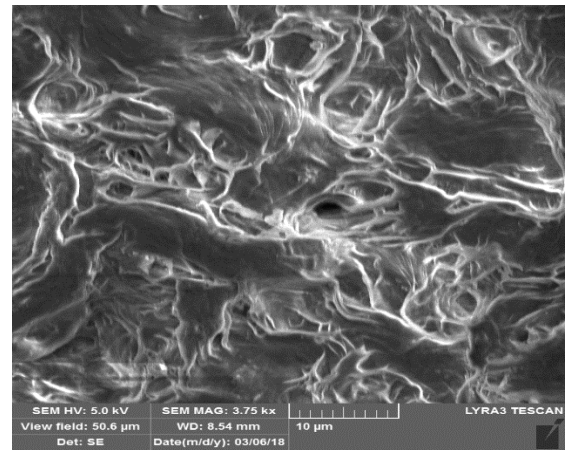


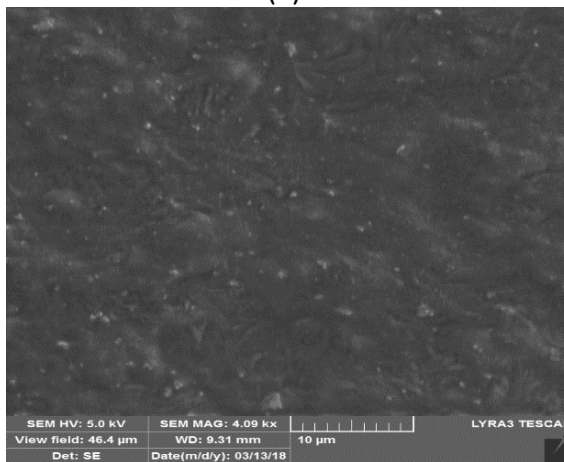
Figure 38: To-view SEM images of there exist spherulite structure in some specimens (a) LiBF₄/PEO film; (b) LAGP40/PEO/LiBF₄ film; (c) LAGP60/PEO/LiBF₄ Film



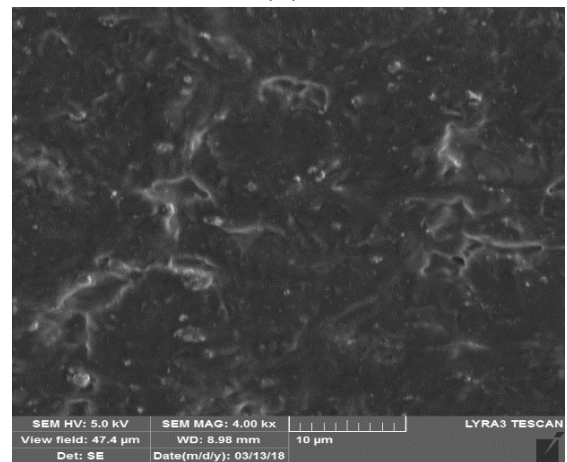
(a)



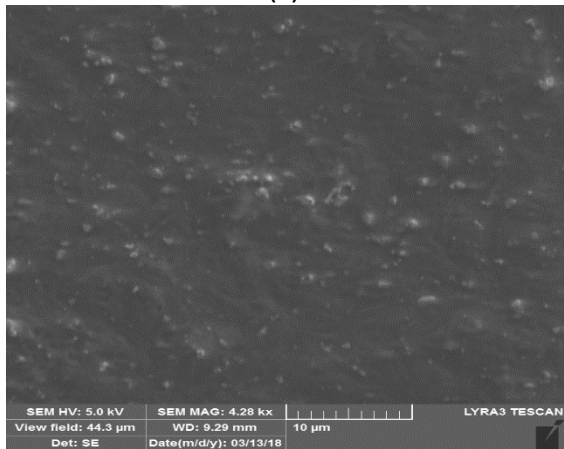
(b)



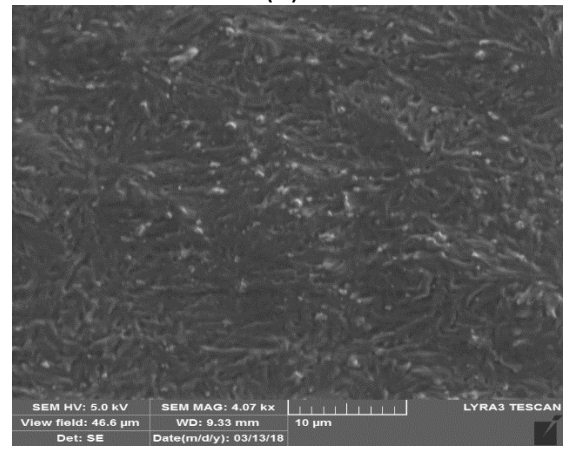
(c)



(d)



(e)



(f)

Figure 39: Top-view SEM images showing the morphological difference between the top side (left) and bottom side (right) of the LiBF₄ series composite films ; (a, b) PEO; (c, d) LAGP20; (e, f) LAGP40

5.7.3 Uncommon large ceramic particles

In some composite films, it was observed large agglomerated LAGP particles.

Figure 40 shows an uncommon large LAGP agglomerate up to 30 micrometer occupying in the composite film. The size is almost the same is film thickness which was subjected to mechanical tests. It is no doubt the large particle size of LAGP can create a weak point leading to earlier fracture and failure, contributing the low ultimate strength and failure strain values.

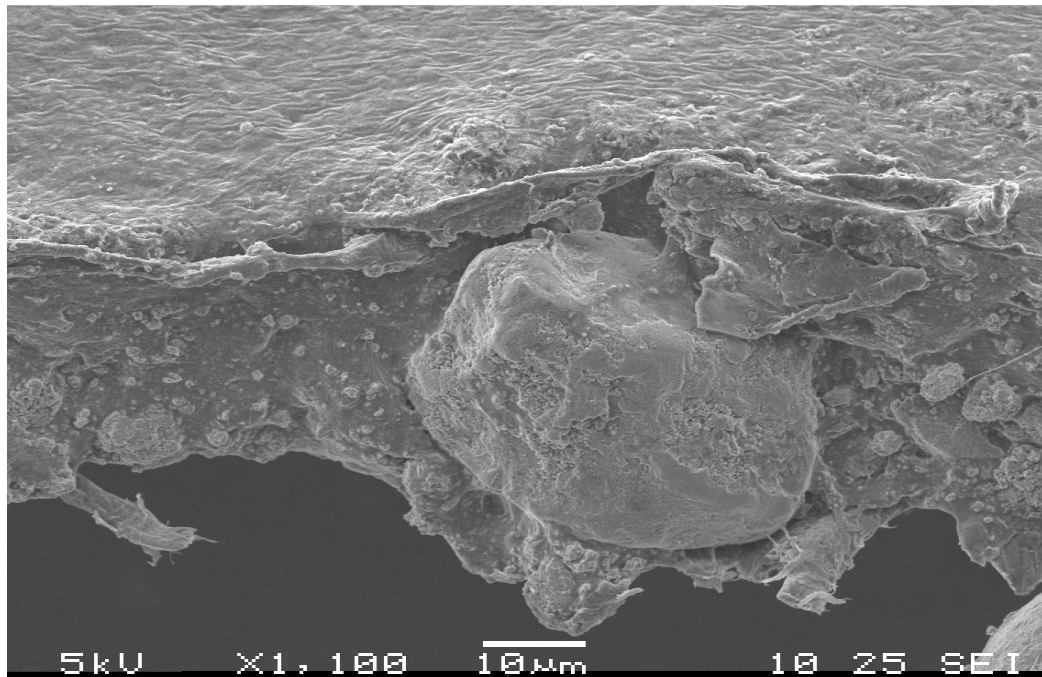


Figure 40: A side-view SEM image showing an uncommon LAGP agglomerate in an area in the LAGP60/PEO/LiBF₄ Film

5.7.4 Internal Ceramic Particle Size and Distribution

As seen the **Figure 31** and **Figure 33**, there is a distribution of elastic moduli, ultimate strength and failure strain for composite films of each LAGP composition. The

variation is much larger in terms of ultimate strength and failure strain. Further, the variation is much larger in LITFSI film series.

For instance, in LAGP50/PEO/LiTFSI films, three different batch (followed same fabrication processing) of samples were tested (see **Figure 41**). In batch 1, the ultimate strength is in the range of 2.5-3.5 MPa and the failure strain is 50-120%. In batch 3, the ultimate strength is 1.7 to 1.9MPa and the failure strain is from 200 to the 550%. In batch 2, the ultimate strength 1.2 to 4.2 MPa and the failure strain is 50 -120%, but some specimens did not fail at the strain of 550%. Mechanical performances from samples in batch 2 lie between batch 1 and 3, suggesting some areas are like those in batch 1 where other areas are close to those in batch 3.

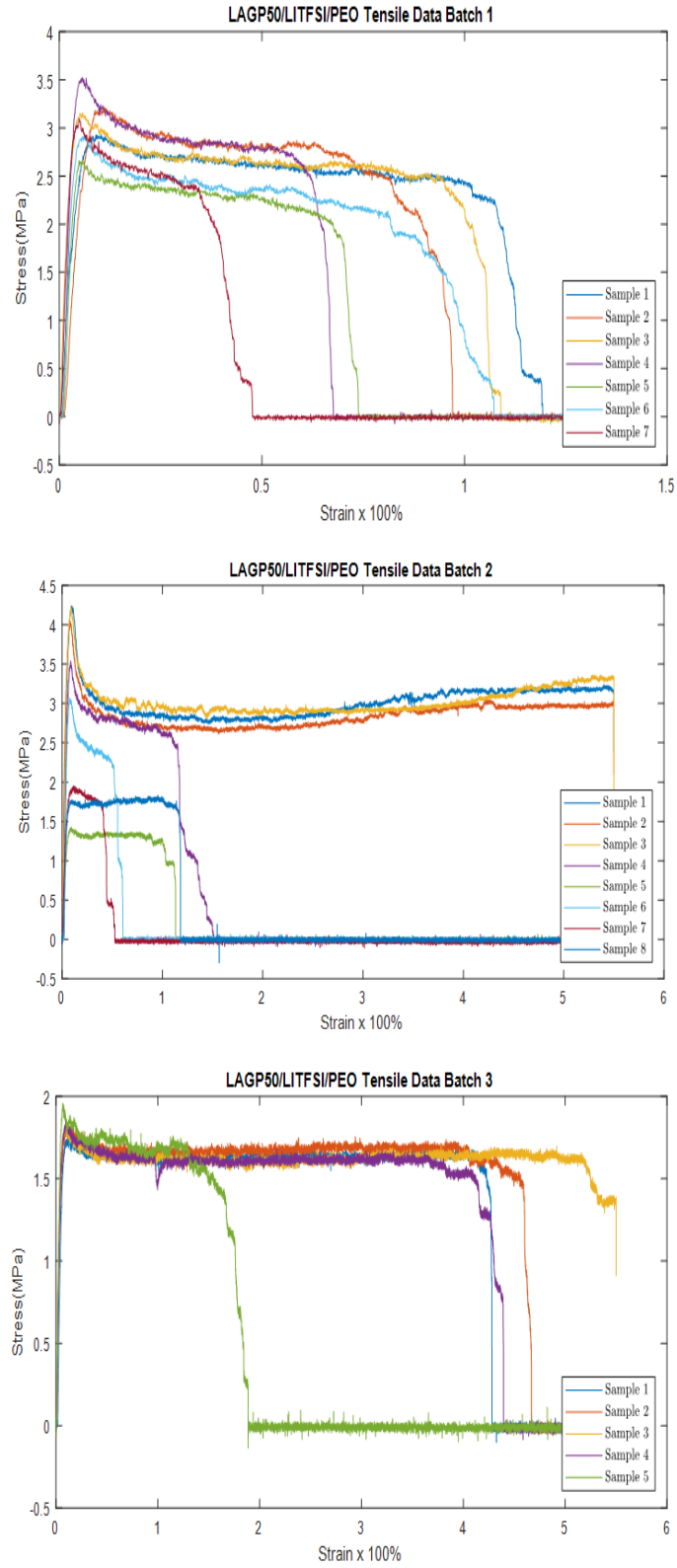


Figure 41: Stress-strain plots of LAGP50/PEO/LITFSI films obtained from three different batch (followed same fabrication processing)

It is hypothesized that the dramatic variation in the LAGP50/PEO/LiTFSI films originated from the different LAGP sizes and distribution. Therefore, the LAGPF films obtained from batch1 and batch 3 were subsequently analyzed with the help of FIB and SEM. **Figure 42 (a-d)** show the SEM images before and after tensile test.

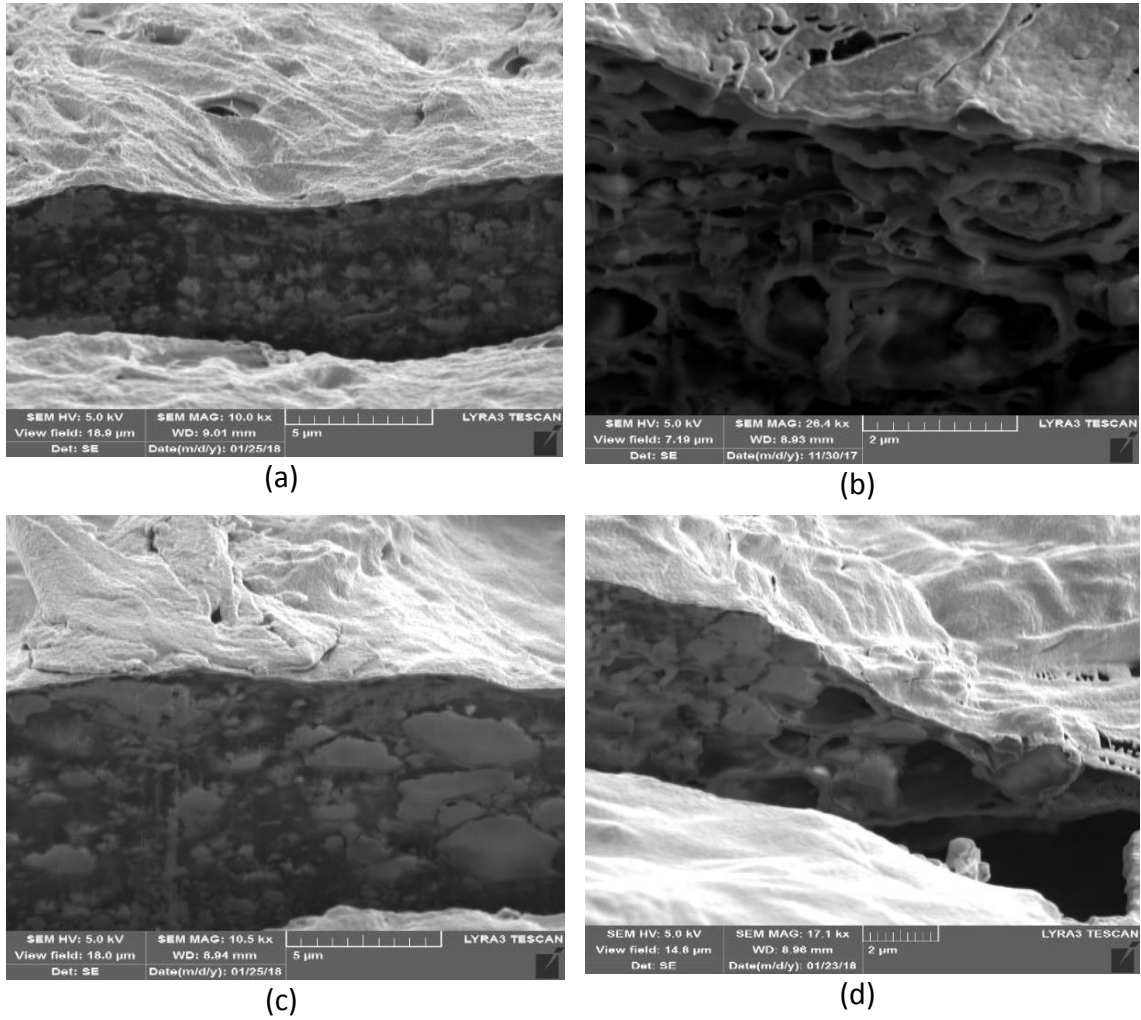


Figure 42: Side—view SEM images of LAGP50/PEO/LiTFSI films before (left) and after (right) tensile stretching cut with the help of FIB. (a, b) batch1; (c, d) batch 3

Seen in **Figure 42**, samples in batch 1 has fine ceramic fillers homogeneously distributed throughout the films. Upon tensile stretching, micropores are also uniformly formed throughout the films and no de-bonded ceramic fillers are observed (see **Figure 42 (b)**). The fine ceramic grains and homogeneity of the composite films are attributed to the higher ultimate strength and elastic moduli but lower strain due to the compositing effect.

In contrast, samples in batch 3 has large variety of ceramic size and inhomogeneous distribution. **Seen in Figure 42(c)**, on the left side there are more fine particles uniformly distributed. However, on the right side in the image, there are many up to 5 micrometer sized ceramic agglomerates and in the vicinity there are some areas with less or no ceramic fillers. After stretching, the large micropores are concentrated in ceramic-poor areas next to the agglomerate-rich areas, and the ceramic-poor areas becomes much thinner indicating where the stress is concentrated. Further, it can be seen a few debonded large ceramic fillers next to the micropores (see **Figure 42(d)**). Consequently, those polymer matrix areas with no or much less ceramic filler contribute to the mechanical behavior similar to bare polymer matrix which is weaker but more ductile than composite. Mechanical performances from samples in batch 2 lie between batch 1 and 3, suggesting some areas are homogeneous like those in batch 1 where other areas are less homogeneous and accumulate with many large ceramic agglomerates close to those in batch 3.

5.8 General Discussion

There are many factors contributing to the mechanical testing results of polymer and ceramic/polymer composite electrolytes. Excluding any processing faults like the container roughness for casting and rapid evaporation of solvent upon drying, the intrinsic parameters related with size and shape of ceramic nanoparticles, ceramic/polymer phase composition, dispersion of nanoparticles, are key important.

A better bonding between the polymer matrix and the reinforcing phase resulted in a higher elastic modulus and a higher strength. A large number of interface between polymer and ceramic filler will be beneficial. Hence, well-dispersed nanoceramics in polymer composite will provide increased the elastic modulus and ultimate strength. The inhomogeneity induced by conventional (or micron) particle/agglomerates filled composites need to be minimized or eliminated.

5.9 Summary

Pure PEO with molecular weight of 400,000 has an elastic module 332MPa and ultimate strength of 13.7MPa. Addition of lithium salts significantly reduces elastic modulus and ultimate strength. For the PEO/LiBF₄ films in which EO to Li ratio is 8:1, elastic modulus is reduced to 230.6 MPa and ultimate strength to 12.2MPa. In the PEO/LiTFSI films with EO to Li ratio of 20:1, elastic modulus is significantly decreased to 23.2 MPa and ultimate strength to 2 MPa, confirming the plasticizer effect of TFSI anions.

When LAGP is added to PEO/Li-salt films, whether LiBF₄ or LiTFSI, there is an upward increase in the elastic moduli. When adding as much as 60 weight percent of LAGP to LiBF₄/PEO films the elastic moduli increases as much as 200 percent. If LAGP is homogenously distributed into LiTFSI/PEO films, it can increase the elastic moduli by as much as 450 percent. For the LiBF₄ composite series, the ultimate strength of the composite films remains relatively unchanged up to LAGP 50 wt%. For LAGP60 films, the ultimate strength slightly reduced. For LiTFSI composite series, the ultimate strength increased to nearly 200 percent. With the increased addition of LAGP, the probability for failure under elongation increases and the amount of strain to failure decreases. With LAGP 60wt%, the failure strain is reduced to 15-50wt% depending on the lithium-salt system and particle distribution uniformity.

Consistent improvement in elastic modulus and ultimate strength is achieved in the composite films when the fine LAGP particles are homogenously distributed in the polymer matrix. In this study, it is constantly observe LAGP agglomerates in the composite films with LAGP composition great than 50wt%. The phenomenon becomes more evident in the LiTFSI series, resulting in non-uniform distribution and hence reduced mechanical properties. Care must be taken in the present casting procedure without further modification.

6 Conclusion

This research is to systematically investigate a series of ceramic/polymer lithium-ion conducting composite electrolytes for potential application to all solid state lithium-ion batteries. The materials selected for study is the $\text{Li}_{1.4}\text{Al}_{0.4}\text{Ge}_{1.6}(\text{PO}_4)_3$ /lithiated polyethylene oxide (LAGP/PEO) with two different lithium salts, LiBF_4 and LiTFSI.

A comprehensive review of literature of traditional and novel electrolytes was conducted and summarized. Based on the past work done, LAGP was synthesized using a solid solution reaction. The crystallinity of the as-synthesized LAGP purity was verified with XRD measurements. The ionic conductivity of sintered LAGP pellets was 1.72×10^{-4} S/cm and the conduction activation energy was 29 kJ/mol which is in line with most of the reported values.

Free-standing composite PEO/LAGP/Li-salt electrolytes were fabricated using the casting approach. The processing was optimized in consideration of solvation, casting, and evaporation. The selected component include 400,000 molecular weight PEO and two different lithium salts, i.e. LiBF_4 and LiTFSI. For LiBF_4 composite films with EO:Li (in LiBF_4) ratio of 8:1 and 0 – 60 weight percent compositions of LAGP were fabricated. For LiTFSI composite films with EO:Li (in LiTFSI) ratio of 20:1 and 0, 20, 30, 50, and 60 weight percent compositions of LAGP were fabricated.

For electrochemical characterization, it was determined that stainless steel and was inappropriate due to the large interface impedance overlapping/overshadowing the electrolyte conduction information. With the help of symmetric cells using lithium foils, reliable conductivities of the composite electrolyte films were determined in the temperature range of 25°C to 80°C. When LAGP is added to the PEO/LiBF₄ films, conductivity drastically decreases. For the LAGP/PEO/LiTFSI electrolyte films, the ionic conductivity decreases in a downward trend, but substantially less than LiBF₄ composite films. It is suggested that nano conductive LAGP should be utilized in the future.

Lastly, mechanical testing was carried out on the compositions using a novel testing system low humidity conditions at a constant strain rate of 1.05%. The elastic moduli, ultimate strength, and failure strain of the composite electrolyte films were systematically investigated. The LAGP/PEO/LiBF₄ composite films increased elastic moduli as much as 200 percent without any decrease in ultimate strength. For LiTFSI films, when the LAGP was homogeneously distributed LiTFSI/PEO films, it can increase the elastic moduli by as much as 450 percent and the ultimate strength nearly 200 percent. With the increased addition of LAGP, the probability for failure under elongation increases and the amount of strain to failure decreases. With LAGP 60wt%, the failure strain is reduced to 15-50wt% depending on the lithium-salt system and particle distribution uniformity.

When LAGP is not homogeneously distributed, the mechanical properties can fluctuate widely and ultimate strength is lowered. It is more challenging to maintain a homogenous distribution in the PEO/LiTFSI based films. Care much be taken in the

present casting procedure without further modification such as the use of another additive or surfactant.

Based on results found in our experiments, we may have discovered the nature of LAGP in regard to its influence on ionic conductivity. In appropriate composite composition, LAGP fillers can enhance the elastic modulus and ultimate strength of electrolyte membrane without sacrificing the strain-to failure, suitable to free-standing fabrication and flexible batteries. The electrochemical performance and thermal properties of the composite membranes are affected but not significantly when appropriate component is selected for the composite membranes. The aforementioned findings suggest that of the LAGP/lithiated composite electrolytes have potential applications to flexible all solid-state lithium-ion batteries.

References

- [1] N. Nitta, F. Wu, J. T. Lee, and G. Yushin, "Li-ion battery materials: Present and future," *Mater. Today*, vol. 18, no. 5, pp. 252–264, 2015.
- [2] P. W. Gruber, P. A. Medina, G. A. Keoleian, S. E. Kesler, M. P. Everson, and T. J. Wallington, "Global lithium availability: A constraint for electric vehicles?," *J. Ind. Ecol.*, vol. 15, no. 5, pp. 760–775, 2011.
- [3] C. Grosjean, P. Herrera Miranda, M. Perrin, and P. Poggi, "Assessment of world lithium resources and consequences of their geographic distribution on the expected development of the electric vehicle industry," *Renew. Sustain. Energy Rev.*, vol. 16, no. 3, pp. 1735–1744, 2012.
- [4] G.-A. Nazri and G. Pistoia, *Lithium Batteries: Science and Technology*. 2003.
- [5] A. J. Bard and L. R. Faulkner, *Electrochemical Methods: Fundamentals and Applications*, 2nd ed. Wiley, 2000.
- [6] K. Mizushima, P. C. Jones, P. J. Wiseman, and J. B. Goodenough, "Li_xCoO₂ (0 < x ≤ 1): A new cathode material for batteries of high energy density," *Solid State Ionics*, vol. 3–4, no. C, pp. 171–174, 1981.
- [7] J. R. Dahn and J. N. Reimers, "Electrochemical and In Situ X-Ray Diffraction Studies of Lithium Intercalation in Li_xCoO₂," vol. 139, no. 8, pp. 2–8, 1992.
- [8] P. A. Nelson, K. G. Gallagher, I. Bloom, and D. W. Dees, "Modeling the Performance and

Cost of Lithium-Ion Batteries for Electric-Drive Vehicles,” pp. 1–102, 2011.

- [9] H. Arai, “Thermal behavior of $\text{Li}_{1-y}\text{NiO}_2$ and the decomposition mechanism,” *Solid State Ionics*, vol. 109, no. 3–4, pp. 295–302, 1998.
- [10] A. Rougier, P. Gravereau, and C. Delmas, “Optimization of the Composition of the $\text{Li}_{1-x}\text{Ni}_x\text{O}_2$ Electrode Materials: Structural, Magnetic, and Electrochemical Studies,” *Electrochem. Soc. Proc. Ser. Pennington, NJ*, vol. 143, no. 4, pp. 1168–1175, 1993.
- [11] A. Yamada, S. C. Chung, and K. Hinokuma, “Optimized LiFePO_4 for Lithium Battery Cathodes,” *J. Electrochem. Soc.*, vol. 148, no. 3, p. A224, 2001.
- [12] M. J. Lee, S. Lee, P. Oh, Y. Kim, and J. Cho, “High performance LiMn_2O_4 cathode materials grown with epitaxial layered nanostructure for Li-Ion batteries,” *Nano Lett.*, vol. 14, no. 2, pp. 993–999, 2014.
- [13] D. Doughty and E. P. Roth, “A General Discussion of Li Ion Battery Safety,” *Electrochem. Soc. Interface*, pp. 37–44, 2012.
- [14] a. J. Smith, J. C. Burns, and J. R. Dahn, “A High Precision Study of the Coulombic Efficiency of Li-Ion Batteries,” *Electrochem. Solid-State Lett.*, vol. 13, no. 12, p. A177, 2010.
- [15] M. M. Thackeray, “Spinel Electrodes for Lithium Batteries,” *J. Am. Ceram. Soc.*, vol. 82, pp. 3347–3354, 1999.
- [16] Y. Qi, H. Guo, L. G. Hector, and A. Timmons, “Threefold Increase in the Young’s Modulus

- of Graphite Negative Electrode during Lithium Intercalation," *J. Electrochem. Soc.*, vol. 157, no. 5, p. A558, 2010.
- [17] E. Markervich, G. Salitra, M. D. Levi, and D. Aurbach, "Capacity fading of lithiated graphite electrodes studied by a combination of electroanalytical methods, Raman spectroscopy and SEM," *J. Power Sources*, vol. 146, no. 1–2, pp. 146–150, 2005.
- [18] M. Hahn *et al.*, "A Dilatometric Study of Lithium Intercalation into Powder-Type Graphite Electrodes," *Electrochem. Solid-State Lett.*, vol. 11, no. 9, p. A151, 2008.
- [19] M. Wagemaker *et al.*, "A kinetic two-phase and equilibrium solid solution in spinel $\text{Li}_{4+x}\text{Ti}_5\text{O}_{12}$," *Adv. Mater.*, vol. 18, no. 23, pp. 3169–3173, 2006.
- [20] S. Franger, C. Bourbon, and F. Le Cras, "Optimized Lithium Iron Phosphate for High-Rate Electrochemical Applications," *J. Electrochem. Soc.*, vol. 151, no. 7, p. A1024, 2004.
- [21] a. . Jansen *et al.*, "Development of a high-power lithium-ion battery," *J. Power Sources*, vol. 81–82, pp. 902–905, 1999.
- [22] K. Zaghib *et al.*, "Safe and fast-charging Li-ion battery with long shelf life for power applications," *J. Power Sources*, vol. 196, no. 8, pp. 3949–3954, 2011.
- [23] M. Ue, Y. Sasaki, Y. Tanaka, and M. Morita, *Electrolytes for Lithium and Lithium-Ion Batteries*, vol. 58. 2014.
- [24] B. Laforge, L. Levan-Jodin, R. Salot, and A. Billard, "Study of Germanium as Electrode in Thin-Film Battery," *J. Electrochem. Soc.*, vol. 155, no. 2, p. A181, 2008.

- [25] R. Chandrasekaran, A. Magasinski, G. Yushin, and T. F. Fuller, "Analysis of Lithium Insertion/Deinsertion in a Silicon Electrode Particle at Room Temperature," *J. Electrochem. Soc.*, vol. 157, no. 10, p. A1139, 2010.
- [26] J. L. Tirado, "Inorganic materials for the negative electrode of lithium-ion batteries: State-of-the-art and future prospects," *Mater. Sci. Eng. R Reports*, vol. 40, no. 3, pp. 103–136, 2003.
- [27] I. A. Courtney, J. S. Tse, O. Mao, J. Hafner, and J. R. Dahn, "Ab initio calculation of the lithium-tin voltage profile," *Phys. Rev. B - Condens. Matter Mater. Phys.*, vol. 58, no. 23, pp. 15583–15588, 1998.
- [28] W. J. Zhang, "Lithium insertion/extraction mechanism in alloy anodes for lithium-ion batteries," *J. Power Sources*, vol. 196, no. 3, pp. 877–885, 2011.
- [29] F. La Mantia, R. A. Huggins, and Y. Cui, "Oxidation processes on conducting carbon additives for lithium-ion batteries," *J. Appl. Electrochem.*, vol. 43, no. 1, pp. 1–7, 2013.
- [30] D. a Scherson and J. D. Protasiewicz, *Electrolytes for Lithium Ion Batteries*. 2009.
- [31] D. Linden and T. B. Reddy, *HANDBOOK OF BATTERIES*. .
- [32] I. Albinsson, B. E. Mellander, and J. R. Stevens, "Ion association effects and ionic conductivity in polymer electrolytes," *Solid State Ionics*, vol. 60, pp. 63–66, 1993.
- [33] Y. Ein-Eli, B. Markovsky, D. Aurbach, Y. Carmeli, H. Yamin, and S. Luski, "The dependence of the performance of Li-C intercalation anodes for Li-ion secondary batteries on the

- electrolyte solution composition," *Electrochim. Acta*, vol. 39, no. 17, pp. 2559–2569, 1994.
- [34] Y. Yamada, K. Usui, C. H. Chiang, K. Kikuchi, K. Furukawa, and A. Yamada, "General observation of lithium intercalation into graphite in ethylene-carbonate-free superconcentrated electrolytes," *ACS Appl. Mater. Interfaces*, vol. 6, no. 14, pp. 10892–10899, 2014.
- [35] J. S. Gnanaraj, R. W. Thompson, J. F. DiCarlo, and K. M. Abraham, "The Role of Carbonate Solvents on Lithium Intercalation into Graphite," *J. Electrochem. Soc.*, vol. 154, no. 3, p. A185, 2007.
- [36] E. Markevich *et al.*, "Reasons for capacity fading of LiCoPO₄ cathodes in LiPF₆ containing electrolyte solutions," *Electrochem. commun.*, vol. 15, no. 1, pp. 22–25, 2012.
- [37] H. Lee, J.-J. Cho, J. Kim, and H.-J. Kim, "Comparison of Voltammetric Responses over the Cathodic Region in LiPF₆ and LiBETI with and without HF," *J. Electrochem. Soc.*, vol. 152, no. 6, p. A1193, 2005.
- [38] R. Sharabi *et al.*, "Raman study of structural stability of LiCoPO₄ cathodes in LiPF₆ containing electrolytes," *J. Power Sources*, vol. 203, pp. 109–114, 2012.
- [39] B. M. Newman, G.H., Francis, R. W., Gaines, L. H., Rao, "Hazard Investigations of LiClO₄ / Dioxolane Electrolyte," *J. Electrochem. Soc.*, vol. 127, no. 9, p. 2025, 1980.
- [40] J. S. Gnanaraj *et al.*, "The use of accelerating rate calorimetry (ARC) for the study of the

- thermal reactions of Li-ion battery electrolyte solutions," *J. Power Sources*, vol. 119–121, pp. 794–798, 2003.
- [41] C. Iwakura *et al.*, "Electrochemical characterization of various metal foils as a current collector of positive electrode for rechargeable lithium batteries," *J. Power Sources*, vol. 68, no. 2, pp. 301–303, 1997.
- [42] L. J. Vimmerstedt, S. Ring, C. J. Hammel, and B. --, "Current Status of Environmental, Health, and Safety Issues of Lithium Ion Electric Vehicle Batteries," no. September 1995, 1995.
- [43] L. J. Krause *et al.*, "Corrosion of aluminum at high voltages in non-aqueous electrolytes containing perfluoroalkylsulfonyl imides; new lithium salts for lithium-ion cells," *J. Power Sources*, vol. 68, no. 2, pp. 320–325, 1997.
- [44] Q. Ma *et al.*, "Novel Li[(CF₃SO₂)(n-C₄F₉SO₂)N]-Based Polymer Electrolytes for Solid-State Lithium Batteries with Superior Electrochemical Performance," *ACS Appl. Mater. Interfaces*, vol. 8, no. 43, pp. 29705–29712, 2016.
- [45] M. S. Ding and T. Richard Jow, "How Conductivities and Viscosities of PC-DEC and PC-EC Solutions of LiBF₄, LiPF₆, LiBOB, Et₄NBF₄, and Et₄NPF₆ Differ and Why," *J. Electrochem. Soc.*, vol. 151, no. 12, p. A2007, 2004.
- [46] Y. Sasaki, M. Handa, K. Kurashima, T. Tonuma, and K. Usami, "Application of Lithium Organoborate with Salicylic Ligand to Lithium Battery Electrolyte," *J. Electrochem. Soc.*, vol. 148, no. 9, pp. A999–A1003, 2001.

- [47] L. C. F. S. O., T. Mixtures, and A. Webber, "Conductivity and Viscosity of Solutions of LiCF_3SO_3 in Organic Solvents," vol. 138, no. 9, pp. 2586–2590, 1991.
- [48] S. S. Zhang, K. Xu, and T. R. Jow, "Study of LiBF_4 as an Electrolyte Salt for a Li-Ion Battery," *J. Electrochem. Soc.*, vol. 149, no. 5, p. A586, 2002.
- [49] P. Ping, Q. Wang, J. Sun, H. Xiang, and C. Chen, "Thermal Stabilities of Some Lithium Salts and Their Electrolyte Solutions With and Without Contact to a LiFePO_4 Electrode," *J. Electrochem. Soc.*, vol. 157, p. A1170, 2010.
- [50] S. Steudte *et al.*, "Hydrolysis study of fluoroorganic and cyano-based ionic liquid anions – consequences for operational safety and environmental stability," *Green Chem.*, vol. 14, no. 9, p. 2474, 2012.
- [51] S. S. Zhang and T. R. Jow, "Aluminum corrosion in electrolyte of Li-ion battery," *J. Power Sources*, vol. 109, no. 2, pp. 458–464, 2002.
- [52] K. Kanamura, "Anodic oxidation of nonaqueous electrolytes on cathode materials and current collectors for rechargeable lithium batteries," *J. Power Sources*, vol. 81–82, pp. 123–129, 1999.
- [53] D. W. McOwen, D. M. Seo, O. Borodin, J. Vatamanu, P. D. Boyle, and W. A. Henderson, "Concentrated electrolytes: decrypting electrolyte properties and reassessing Al corrosion mechanisms," *Energy Environ. Sci.*, vol. 7, no. 1, pp. 416–426, 2014.
- [54] N. Williard, W. He, C. Hendricks, and M. Pecht, "Lessons learned from the 787 dreamliner

- issue on Lithium-Ion Battery reliability,” *Energies*, vol. 6, no. 9, pp. 4682–4695, 2013.
- [55] E. Peled and S. Menkin, “Review—SEI: Past, Present and Future,” *J. Electrochem. Soc.*, vol. 164, no. 7, pp. A1703–A1719, 2017.
- [56] L. Long, S. Wang, M. Xiao, and Y. Meng, “Polymer electrolytes for lithium polymer batteries,” *J. Mater. Chem. A*, vol. 4, no. 26, pp. 10038–10069, 2016.
- [57] I. Nicotera, L. Coppola, C. Oliviero, A. Russo, and G. A. Ranieri, “Some physicochemical properties of PAN-based electrolytes: Solution and gel microstructures,” *Solid State Ionics*, vol. 167, no. 3–4, pp. 213–220, 2004.
- [58] C. M. Mathew, B. Karthika, M. Ulaganathan, and S. Rajendran, “Electrochemical analysis on poly (ethyl methacrylate) -based electrolyte membranes,” *Bull. Mater. Sci.*, vol. 38, no. 1, pp. 1–6, 2015.
- [59] M. Marcinek *et al.*, “Electrolytes for Li-ion transport - Review,” *Solid State Ionics*, vol. 276, pp. 107–126, 2015.
- [60] S. Abbrent and S. Greenbaum, “Recent progress in NMR spectroscopy of polymer electrolytes for lithium batteries,” *Curr. Opin. Colloid Interface Sci.*, vol. 18, no. 3, pp. 228–244, 2013.
- [61] P. Judeinstein, D. Reichert, E. R. DeAzevedo, and T. J. Bonagamba, “NMR multi-scale description of ionic conductivity mechanisms inside polymer electrolytes,” *Acta Chim. Slov.*, vol. 55, no. 1, pp. 349–360, 2008.

- [62] L. H. Sperling, *Introduction to Physical Polymer Science*, vol. 78. 2006.
- [63] H. S. Choe, J. Giaccai, M. Alamgir, and K. M. Abraham, "Preparation and characterization of poly(vinyl sulfone)- and poly(vinylidene fluoride)-based electrolytes," *Electrochim. Acta*, vol. 40, no. 13–14, pp. 2289–2293, 1995.
- [64] A. Manuscript and S. Magnitude, "Polymer chain organization in tensile-stretched poly(ethylene oxide)-based polymer electrolytes," vol. 31, no. 9, pp. 1713–1723, 2013.
- [65] S. Choudhary and R. J. Sengwa, "Dielectric relaxation and lithium ion transport study of ultrasonic and microwave irradiated polymer nanocomposite electrolytes," vol. 21, no. February, pp. 7–15, 2014.
- [66] Y. Kong and J. N. Hay, "The enthalpy of fusion and degree of crystallinity of polymers as measured by DSC," *Eur. Polym. J.*, vol. 39, no. 8, pp. 1721–1727, 2003.
- [67] K. Xu, "Nonaqueous liquid electrolytes for lithium-based rechargeable batteries," *Chem. Rev.*, vol. 104, no. 10, pp. 4303–4417, 2004.
- [68] J. Evans, C. A. Vincent, and P. G. Bruce, "Electrochemical measurement of transference numbers in polymer electrolytes," *Polymer (Guildf.)*, vol. 28, no. 13, pp. 2324–2328, 1987.
- [69] H. Zhang *et al.*, "Single lithium-ion conducting solid polymer electrolytes: advances and perspectives," *Chem. Soc. Rev.*, vol. 46, no. 3, pp. 797–815, 2017.
- [70] C. A. Angell, K. Xu, S. S. Zhang, and M. Videa, "Variations on the salt-polymer electrolyte

theme for flexible solid electrolytes," *Solid State Ionics*, vol. 86–88, no. PART 1, pp. 17–28, 1996.

- [71] Z. Florjańczyk *et al.*, "Polymer-in-salt electrolytes based on acrylonitrile/butyl acrylate copolymers and lithium salts," *J. Phys. Chem. B*, vol. 108, no. 39, pp. 14907–14914, 2004.
- [72] A. Ferry, L. Edman, M. Forsyth, D. R. MacFarlane, and J. Sun, "Connectivity, ionic interactions, and migration in a fast-ion-conducting polymer-in-salt electrolyte based on poly(acrylonitrile) and LiCF₃SO₃," *J. Appl. Phys.*, vol. 86, no. 4, pp. 2346–2348, 1999.
- [73] J. W. Fergus, "Ceramic and polymeric solid electrolytes for lithium-ion batteries," *J. Power Sources*, vol. 195, no. 15, pp. 4554–4569, 2010.
- [74] X. G. Sun and J. B. Kerr, "Synthesis and characterization of network single ion conductors based on comb-branched polyepoxide ethers and lithium bis(allylmalonato)borate," *Macromolecules*, vol. 39, no. 1, pp. 362–372, 2006.
- [75] K. Kerman, A. Luntz, V. Viswanathan, Y.-M. Chiang, and Z. Chen, "Review—Practical Challenges Hindering the Development of Solid State Li Ion Batteries," *J. Electrochem. Soc.*, vol. 164, no. 7, pp. A1731–A1744, 2017.
- [76] F. P. McGrogan *et al.*, "Compliant Yet Brittle Mechanical Behavior of Li₂S–P₂S₅ Lithium-Ion-Conducting Solid Electrolyte," *Adv. Energy Mater.*, vol. 7, no. 12, pp. 1–5, 2017.
- [77] J. Wolfenstine *et al.*, "A preliminary investigation of fracture toughness of Li₇La₃Zr₂O₁₂ and its comparison to other solid Li-ion conductors," *Mater. Lett.*, vol. 96,

pp. 117–120, 2013.

- [78] S. Smith, T. Thompson, J. Sakamoto, J. L. Allen, D. R. Baker, and J. Wolfenstine, “Electrical, mechanical and chemical behavior of $\text{Li}_{1.2}\text{Zr}_{1.9}\text{Sr}_{0.1}(\text{PO}_4)_3$,” *Solid State Ionics*, vol. 300, pp. 38–45, 2017.
- [79] D. R. Paul and L. M. Robeson, “Polymer nanotechnology: Nanocomposites,” *Polymer (Guildf)*, vol. 49, no. 15, pp. 3187–3204, 2008.
- [80] L. Lee, S. Park, and S. Kim, “Effect of nano-sized barium titanate addition on PEO / PVDF blend-based composite polymer electrolytes,” *Solid State Ionics*, vol. 234, pp. 19–24, 2013.
- [81] J. Jeon, M. Kim, and S. Kwak, “Effects of addition of TiO_2 nanoparticles on mechanical properties and ionic conductivity of solvent-free polymer electrolytes based on porous P (VdF-HFP) / P (EO-EC) membranes,” vol. 162, pp. 1304–1311, 2006.
- [82] C. Capiglia, P. Mustarelli, E. Quartarone, C. Tomasi, and A. Magistris, “Effects of nanoscale SiO_2 on the thermal and transport properties of solvent-free, poly(ethylene oxide) (PEO)-based polymer electrolytes,” *Solid State Ionics*, vol. 118, pp. 73–79, 1999.
- [83] S. Klongkan and J. Pumchusak, “Effects of nano alumina and plasticizers on morphology, ionic conductivity, thermal and mechanical properties of PEO-LiCF₃SO₃ Solid Polymer Electrolyte,” *Electrochim. Acta*, vol. 161, pp. 171–176, 2015.
- [84] Y.-C. Jung, S.-M. Lee, J.-H. Choi, S. S. Jang, and D.-W. Kim, “All Solid-State Lithium

- Batteries Assembled with Hybrid Solid Electrolytes," *J. Electrochem. Soc.*, vol. 162, no. 4, pp. A704–A710, 2015.
- [85] Y. Zhao *et al.*, "A promising PEO/LAGP hybrid electrolyte prepared by a simple method for all-solid-state lithium batteries," *Solid State Ionics*, vol. 295, pp. 65–71, 2016.
- [86] Y. Zhao *et al.*, "A new solid polymer electrolyte incorporating Li₁₀GeP₂S₁₂ into a polyethylene oxide matrix for all-solid-state lithium batteries," *J. Power Sources*, vol. 301, pp. 47–53, 2016.
- [87] W. Wang, E. Yi, A. J. Fici, R. M. Laine, and J. Kieffer, "Lithium Ion Conducting Poly(ethylene oxide)-Based Solid Electrolytes Containing Active or Passive Ceramic Nanoparticles," *J. Phys. Chem. C*, vol. 121, no. 5, pp. 2563–2573, 2017.
- [88] J. H. Choi, C. H. Lee, J. H. Yu, C. H. Doh, and S. M. Lee, "Enhancement of ionic conductivity of composite membranes for all-solid-state lithium rechargeable batteries incorporating tetragonal Li₇La₃Zr₂O₁₂ into a polyethylene oxide matrix," *J. Power Sources*, vol. 274, pp. 458–463, 2015.
- [89] L. Chen, Y. Li, S. P. Li, L. Z. Fan, C. W. Nan, and J. B. Goodenough, "PEO/garnet composite electrolytes for solid-state lithium batteries: From 'ceramic-in-polymer' to 'polymer-in-ceramic,'" *Nano Energy*, vol. 46, no. August 2017, pp. 176–184, 2018.
- [90] C. J. Leo, B. V. R. Chowdari, G. V. S. Rao, and J. L. Souquet, "Lithium conducting glass ceramic with Nasicon structure," *Mater. Res. Bull.*, vol. 37, no. 8, pp. 1419–1430, 2002.

- [91] H. Chung and B. Kang, "Increase in grain boundary ionic conductivity of $\text{Li}_{1.5}\text{Al}_{0.5}\text{Ge}_{1.5}(\text{PO}_4)_3$ by adding excess lithium," *Solid State Ionics*, vol. 263, pp. 125–130, 2014.
- [92] J. K. Feng, L. Lu, and M. O. Lai, "Lithium storage capability of lithium ion conductor $\text{Li}_{1.5}\text{Al}_{0.5}\text{Ge}_{1.5}(\text{PO}_4)_3$," *J. Alloys Compd.*, vol. 501, no. 2, pp. 255–258, 2010.
- [93] L. Ai, G. Po, M. Kotobuki, and M. Koishi, "Sol–gel synthesis of $\text{Li}_{1.5}\text{Al}_{0.5}\text{Ge}_{1.5}(\text{PO}_4)_3$ solid electrolyte," *Ceram. Int.*, vol. 41, no. 7, pp. 8562–8567, 2015.
- [94] R. E. Hummel, *Electronic properties of materials / Rolf E. Hummel*, vol. 53. 2012.
- [95] P. D. Kichambare, T. Howell, and S. Rodrigues, "Sol – Gel-Derived Lithium Superionic Conductor," vol. 5, pp. 391–396, 2014.
- [96] K. Arbi, W. Bucheli, R. Jiménez, and J. Sanz, "High lithium ion conducting solid electrolytes based on NASICON $\text{Li}_{1+x}\text{Al}_x\text{M}_{2-x}(\text{PO}_4)_3$ materials ($\text{M} = \text{Ti}, \text{Ge}$ and $0 \leq x \leq 0.5$)," *J. Eur. Ceram. Soc.*, vol. 35, no. 5, pp. 1477–1484, 2015.
- [97] M. Zhang, Z. Huang, J. Cheng, O. Yamamoto, N. Imanishi, and B. Chi, "prepared by tape casting," *J. Alloys Compd.*, vol. 590, pp. 147–152, 2014.
- [98] C. J. Leo, G. V. Subba Rao, and B. V. R. Chowdari, "Effect of MgO addition on the ionic conductivity of $\text{LiGe}_2(\text{PO}_4)_3$ ceramics," *Solid State Ionics*, vol. 159, no. 3–4, pp. 357–367, 2003.
- [99] J. K. Feng, B. G. Yan, J. C. Liu, M. O. Lai, and L. Li, "All solid state lithium ion rechargeable

- batteries using NASICON structured electrolyte,” vol. 28, no. 5, pp. 3–6, 2013.
- [100] Y. Liu, J. Chen, and J. Gao, “Preparation and chemical compatibility of lithium aluminum germanium phosphate solid electrolyte,” *Solid State Ionics*, no. July, pp. 0–1, 2017.
- [101] P. Hartmann *et al.*, “Degradation of NASICON-type materials in contact with lithium metal: Formation of mixed conducting interphases (MCI) on solid electrolytes,” *J. Phys. Chem. C*, vol. 117, no. 41, pp. 21064–21074, 2013.
- [102] X. Xu, Z. Wen, X. Wu, X. Yang, and Z. Gu, “Xiaoxiong Xu, Zhaoyin Wen,” vol. 2806, no. 22226, pp. 2802–2806, 2007.
- [103] J. S. Thokchom and B. Kumar, “The effects of crystallization parameters on the ionic conductivity of a lithium aluminum germanium phosphate glass – ceramic,” vol. 195, pp. 2870–2876, 2009.
- [104] M. Zhang, K. Takahashi, N. Imanishi, and Y. Takeda, “Preparation and Electrochemical Properties of $\text{Li}_{1+x}\text{Al}_x\text{Ge}_{2-x}(\text{PO}_4)_3$ Synthesized by a Sol-Gel Method,” vol. 159, no. 7, pp. 1114–1119, 2012.
- [105] S. S. Zhang, K. Xu, and T. R. Jow, “A new approach toward improved low temperature performance of Li-ion battery,” vol. 4, pp. 928–932, 2002.
- [106] A. K. Sircar, P. T. Weissman, and B. Kumar, “Evaluation of Doped Polyethylene Oxide As Solid Electrolyte For Polymer Batteries,” 1992.
- [107] S. J. Wen, T. J. Richardson, D. I. Ghanous, K. a Striebel, P. N. Ross, and E. J. Cairns, “FTIR

- characterization of PEO+LiN(CF₃SO₂)(₂) electrolytes," *J. Electroanal. Chem.*, vol. 408, pp. 113–118, 1996.
- [108] X. W. Zhang, C. Wang, A. J. Appleby, and F. E. Little, "Characteristics of lithium-ion-conducting composite polymer-glass secondary cell electrolytes," *J. Power Sources*, vol. 112, no. 1, pp. 209–215, 2002.
- [109] E. A. Rietman, M. L. Kaplan, and R. J. Cava, "Lithium ion-poly (ethylene oxide) complexes. I. Effect of anion on conductivity," *Solid State Ionics*, vol. 17, no. 1, pp. 67–73, 1985.
- [110] H. Zhang *et al.*, "Lithium bis(fluorosulfonyl)imide/poly(ethylene oxide) polymer electrolyte," *Electrochim. Acta*, vol. 133, pp. 529–538, 2014.
- [111] W. A. Henderson, "Glyme-lithium salt phase behavior," *J. Phys. Chem. B*, vol. 110, no. 26, pp. 13177–13183, 2006.
- [112] D. M. Seo, O. Borodin, S.-D. Han, Q. Ly, P. D. Boyle, and W. A. Henderson, "Electrolyte Solvation and Ionic Association I," *J. Electrochem. Soc.*, vol. 159, no. 5, p. A553, 2012.
- [113] H. R. Allcock, D. T. Welna, and A. E. Maher, "Single ion conductors-polyphosphazenes with sulfonimide functional groups," *Solid State Ionics*, vol. 177, no. 7–8, pp. 741–747, 2006.
- [114] F. R. Barnet, "Elastic Constants Of Bulk Polymers," 1972.
- [115] H.-Y. Nie, M. Motomatsu, W. Mizutani, and H. Tokumoto, "Local elasticity measurement on polymers using atomic force microscopy," *Thin Solid Films*, vol. 273, no. 1–2, pp. 143–

148, 1996.

- [116] A. E. O. Connor and N. Willenbacher, "The effect of molecular weight and temperature on tack properties of model polyisobutylenes," vol. 24, pp. 335–346, 2004.
- [117] M. Singh *et al.*, "Effect of Molecular Weight on the Mechanical and Electrical Properties of Block Copolymer Electrolytes," pp. 4578–4585, 2007.
- [118] D. Devaux, R. Bouchet, D. Glé, and R. Denoyel, "Mechanism of ion transport in PEO/LiTFSI complexes: Effect of temperature, molecular weight and end groups," *Solid State Ionics*, vol. 227, pp. 119–127, 2012.
- [119] R. S. Figliola and D. E. Beasley, *Theory and Design for Mechanical Measurements*. 2011.
- [120] P. J. Bates and C. Y. Wang, "The effect of sample preparation on the mechanical properties of nylon 66," *Polym. Eng. Sci.*, vol. 43, no. 4, pp. 759–773, 2003.